Master of Science Thesis

Physics of dielectric-barrier discharge in gas

A numerical study

F.G.A. van de Beek

May 24, 2017

ÉCOLE POLYTECHNIQUE
FÉDÉRALE DE LAUSANNE

Aerodynamics

TU Delft

Faculty of Aerospace Engineering

Delft University of Technology

Physics of dielectric-barrier discharge in gas

A numerical study

Master of Science Thesis

For obtaining the degree of Master of Science in Aerospace Engineering
at Delft University of Technology

F.G.A. van de Beek

May 24, 2017

Faculty of Aerospace Engineering · Delft University of Technology

Delft University of Technology

DELFT UNIVERSITY OF TECHNOLOGY
DEPARTMENT OF AERODYNAMICS

The undersigned hereby certify that they have read and recommend to the Faculty of Aerospace Engineering for acceptance the thesis entitled **"Physics of dielectric-barrier discharge in gas"** by **F.G.A. van de Beek** in fulfillment of the requirements for the degree of **Master of Science**.

Dated: May 24, 2017

Head of department: ______________________
Prof. Dr. S. Hickel

Primary supervisor (EPFL): ______________________
Dr. P. Leyland

Primary supervisor (DUT): ______________________
Dr. M. Kotsonis

Secondary supervisor (DUT): ______________________
Dr. S.J. Hulshoff

External member: ______________________
Dr. V. Gentile

Preface

This document contains the full report of my thesis project on the development of numerical methods for plasma actuated flow control. The thesis was conducted under the Aerodynamics department of the aerospace engineering faculty of Delft University of Technology (DUT), under supervision of Dr. M. Kotsonis, in close collaboration with and partially under the Interdisciplinary Aerodynamics Group (IAG) at the École Polytechnique Fédérale de Lausanne (EPFL), under supervision of Dr. P. Leyland. I hope that I have been able to help advance both groups in the field of plasma actuated flow control, in spite of my work being a humble master thesis project.

I would like to show my gratitude to Pénélope Leyland for facilitating my stay at EPFL, where I've had a very wonderful and utmost fruitful time. Furthermore, I thank my supervisor Marios Kotsonis for the pragmatic and effective support he was able to provide me, both in technical and non-technical sense, and for giving me the guidance I needed to bring this thesis to a satisfying end. Also, I would like to thank Steven Hulshoff for the interesting discussions on numerical methods, and Prof. Dr. S. Hickel and Dr. V. Gentile for taking the time to assess my thesis.

Finally, I would like to thank both the ZKS Schindler Foundation and the Justus and Louise van Effen Fund for awarding me their master scholarships, thereby financially facilitating my stay in Switzerland, which would not have been possible without.

Den Haag, the Netherlands
May 24, 2017

Floris G.A. van de Beek

Summary

Efficiency increase of aerodynamic bodies should always be striven for. Plasma actuated flow control is a promising technique, but not yet ready for implementation. Better understanding of the fundamental physics can be achieved using numerical methods. This study aims at development of a robust and flexible framework for modelling of dielectric-barrier discharge in gaseous media by implementation of a plasma model into OpenFoam® .

By creating a strong electric field between two electrodes, plasma can be generated, existing of a mixture of charged (ionized) particles and the neutral parent gas. Different discharges can be generated, where corona and streamer discharges are the most notable ones. Dielectric-barrier discharge (DBD) is most popular in active flow control, which includes a layer of insulating but polarizing material shielding at least one of the electrodes. By using an alternating current (AC) or nanosecond (ns) pulsed actuation signal, termination of the generated discharge by charge accumulation on the dielectric surface can be prevented. The neutral flow experiences different interaction with the plasma under different input signals, in short being a body force for the continuous signal and energy deposition for the pulsed signal.

Most types of discharges can be described using the same plasma model, governed by the drift-diffusion equations and Gauss' law for electrostatics. These equations describe charged particle transport, creation and destruction through chemical reactions, driven by the electric field. The drift-diffusion equations are continuity equations for the different particle species, and are heavily coupled to the equation for electrostatics. The model problem was described as a 1D volumetric or 2D surface DBD set-up, involving a gaseous region and electrode and dielectric solid regions. The 1D set-up involves two parallel opposing plates separated by the dielectric layers and the gas, whereas in the 2D set-up the two electrodes are situated parallel, with one plate buried in a dielectric layer with the other electrode in contact with the gas. Particles are assumed to recombine instantly when colliding on the geometric surfaces, where their charge is stored which is known as surface charging.

Up to three species are considered, comprising of electrons, positive and negative species. The governing equations are solved in a semi-implicit and sequential manner. The strong coupling existing between the equations were overcome by predictor-corrector algorithm, which uses a first order approximation of charge densities in a semi-implicit formulation of Gauss' law to predict the electric field at the new time step. The corrector algorithm then corrects the solutions by iteratively solving for the species densities and the electric field, which heavily depend on one another. The inter-dependency of the continuity equations were overcome by a Strang splitting method. A MUSCL scheme and a forward Euler scheme were used for spatial and temporal discretization, respectively.

During code verification, first order accuracy was observed for the Laplacian scheme of the electrostatic equation as well as for the convective scheme of the continuity equations. A Gauss-Seidel method was used to solve the electric field sequentially in the different regions, accelerated through over-relaxation. Discretization of the coupling condition was found to be first order, yielding first order accuracy for the Laplacian scheme as well. Although higher accuracy could not be obtained, the computational routine is at least convergent. The model was successfully validated qualitatively against a volumetric glow discharge case from literature, proving the physics are treated correctly. Quantitative validation on the other hand could not be achieved and requires experimental data. Robustness of the computational routine was observed, but at the cost of computational efficiency.

Table of Contents

List of Figures

List of Tables

Terminology / Notation

Acronyms / Abbreviations

- **ACDBD** Alternating Current DBD
- **DBD** Dielectric-Barrier Discharge
- **EHD** ElectroHydroDynamic(s)
- **LFA** Local Field Approximation
- **nsDBD** nanosecond DBD

List of symbols

Table 1: Universal constants

Symbol	Name	Value	Units
ε_0	Absolute permittivity of vacuum	8.854×10^{-12}	$\mathrm{F} \cdot \mathrm{m}^{-1}$
e	Elementary charge	1.602×10^{-19}	C
k_B	Boltzmann constant	1.381×10^{-23}	$\mathrm{J} \cdot \mathrm{K}^{-1}$
m_e	Electron particle mass	9.109×10^{-31}	kg
m_N	Nitrogen (N_2) particle mass	4.652×10^{-26}	kg
m_O	Oxygen (O_2) particle mass	5.314×10^{-26}	kg
m_{He}	Helium (He_2) particle mass	6	644×10^{-27}
m_{Ar}	Argon (Ar_2) particle mass	6	633×10^{-26}

Table 2: Physical quantities

Symbol	Name	Units
α	Ionization coefficient	m^{-1}
β_{ei}	Electron-ion recombination coefficient	$\mathrm{m}^3 \cdot \mathrm{s}^{-1}$
β_{ii}	Ion-ion recombination coefficient	$\mathrm{m}^3 \cdot \mathrm{s}^{-1}$
η	Attachment coefficient	m^{-1}
η_E	Electronic excitation power fraction coefficient	$-$
η_{el-R}	Elastic-rotational power fraction coefficient	$-$
η_{VT}	Vibrational-translational relaxation power fraction coefficient	$-$
γ	Secondary electron emission factor coefficient	$-$
μ_k	Specie mobility coefficient	$\mathrm{m}^2 \cdot \mathrm{V}^{-1}\mathrm{s}^{-1}$
ϕ	Electrostratic potential scalar	V
ρ_c	Charge volume density scalar	$\mathrm{C} \cdot \mathrm{m}^{-3}$
σ	Charge surface density scalar	$\mathrm{C} \cdot \mathrm{m}^{-2}$
σ_e	Conductivity of gas scalar	$\mathrm{S} \cdot \mathrm{m}^{-1}$
ε_d	Relative permittivity of dielectric coefficient	$\mathrm{F} \cdot \mathrm{m}^{-1}$
$\vec{\Gamma}_k$	Specie flux vector	$\mathrm{m}^{-2}\mathrm{s}^{-1}$
$\vec{E}$	Electric field vector	$\mathrm{V} \cdot \mathrm{m}^{-1}$
$\vec{F}_{EHD}$	Electrohydrodynamic force density vector	$\mathrm{N} \cdot \mathrm{m}^{-3}$
$\vec{J}_k$	Specie current density vector	$\mathrm{A} \cdot \mathrm{m}^{-2}$
$\vec{M}_{EHD}$	Electrohydrodynamic momentum density vector	$\mathrm{Ns} \cdot \mathrm{m}^{-3}$
$\vec{U}_k$	Specie velocity vector	$\mathrm{m} \cdot \mathrm{s}^{-1}$
D_k	Specie diffusion coefficient	$\mathrm{m}^2 \cdot \mathrm{V}^{-1}\mathrm{s}^{-1}$
E/N	Reduced electric field scalar	Td
E_{EHD}	Electrohydrodynamic energy density scalar	$\mathrm{E} \cdot \mathrm{m}^{-3}$
k	Specie subscript index for **e**lectron/**p**ositive ion/**n**egative ion	e/p/n
N_k	Specie number density scalar	m^{-3}
P_{EHD}	Electrohydrodynamic power density scalar	$\mathrm{W} \cdot \mathrm{m}^{-3}$
P_g	Gas bulk pressure	Torr
P_k	Specie partial pressure	Torr
T_g	Gas bulk temperature	K
T_k	Specie temperature	eV
V_{br}	Breakdown voltage	V
d	Electrode gap spacing	m

Chapter 1

Introduction

Plasma is finding its way into many engineering applications, from surface treatment to production of ozone. In aerodynamics, initiating a small plasma region in the flow over the surface of an immersed body has been found to alter the flow in such ways that it can be utilized for flow control; the active guidance of the flow over an aerodynamic body. This is achieved by triggering small continuous or repetitively pulsed electric discharge currents through the flow over the surface of an object. The gas is brought in motion by electrostatic force mechanisms, without the need for mechanically moving parts. This was found already in 1750 by B. Wilson, who managed to make a pin wheel rotate just by applying a voltage to it, as reported by Collier and Gourdine (1968). The strong electric fields generated at the sharp edged geometry ionizes the air by generating a corona discharge, and the positive ions forced away from the tip transfer their momentum to the neutral particles, causing a so called ionic wind. As Newton already prescribed, the net body force applied to the air requires an equal but opposite component, applied to the pin wheel and making it spin. This sparked interest in development of devices relying on this so called electrohydrodynamic principle for engineering purposes.

1.1 Practical relevance of the subject

Most research performed today on plasma actuated flow control finds its application in the aircraft industry, such as separation and transition control (Post and Corke (2004); Huang et al. (2006); Little et al. (2010); Glezer et al. (2005); Little et al. (2012)), shockwave control (Nishihara et al. (2011)) or even flight control (Lee et al. (1997)). Albeit, optimization of aerodynamic performance of an object is relevant to all applications involving aerodynamics. For other applications, one may think of efficiency increase of wind turbines, drag reduction of trucks or performance enhancement of combustion engines (Starikovskaia (2014)). Concluding, this technique knows many applications, all of which have one common denominator: increase of efficiency, required for a reduction in energy usage. This is an important drive, as the world will only grow more hungry for energy, and technological development must make sure that the transportation sector [1], or the energy consumption market in general, is allowed to grow to meet demand, without compromising our living environment. Until a revolution takes place in the way mankind transports itself, research must keep improving the current conventional methods, and strive for an ever increase in efficiency of these methods. For example, by taking old but high potential concepts and making them the current state of the art.

This thesis aims at contributing to this goal for the technique of plasma actuated flow control: the active guidance of a flow over an aerodynamic body by plasma forcing. This technique is very promising: the lack of mechanically moving parts can be a great advantage over other means of active flow control, requiring only a simple and light-weight design for the actuator. The required input voltages may be high, but at the right discharge types, the discharge current is moderate and often of a very short duration, keeping the total power consumption of an actuator at acceptable levels and making the whole actuator very efficient (Moreau (2007)). But most importantly, the actuators have been found very effective in their interaction with macroscopic aerodynamic structures and phenomena, at least in laboratory environments.

On the other hand, development of plasma actuators still has to take a number of important steps. Power supplies for certain types of actuators are far from implementation ready. Also, the electromagnetic interference induced by the electric systems is not well controlled either. But most importantly, the flow interaction processes are simply not fully understood yet. This is essential for optimal design and control of actuators, but is also crucial in light of safety during operation.

In modern times, an unmissable step in reaching this level of understanding is by research and development of numerical methods. Such methods enforce deep understanding of the fundamental physics by the need of a physical model, while giving access to a reality where a wide range of circumstances can be mimicked cheaply and quickly.

Delft University of Technology (DUT) and École Polytechnique Fédérale de Lausanne (EPFL) have both been working on the topic of plasma actuators for a number of years now and have already reached a broad understanding of its working principles. At DUT, research has been done under the supervision of Dr M. Kotsonis on actuator design and control necessary to make this device applicable, while at EPFL under supervision of Dr P. Leyland, experimental work has been done on the plasma physics which make this type of flow control possible. To reach a technology readiness level required for application in industry, a deeper and more fundamental understanding of the parameters and variables which influence the actuation process and quality should be obtained. A strong basis has been laid through experimental work (Kotsonis et al. (2014), Peschke (2014)). Some numerical work has preceded this project, but have mostly been focussed on the induced flow dynamics (Kotsonis et al. (2011)) and less on the plasma physics behind it. The work of Goekce (2014) was a first step in modelling of the plasma physics by simulating a streamer discharge in air, although there were many difficulties validating the model. Also, the program was written in a language which does not

---

[1] https://www.eia.gov/outlooks/ieo/world.cfm, under transportation sector

provide a reliable platform for further development.

1.2 Thesis outline

This project is set-up to meet the demand for a robust platform for development of a first-principle electrohydrodynamic model. The **aim** is then to **take a first step and lay a solid foundation for a fully coupled model for simulation of non-equilibrium cold plasma discharge processes and flow interaction based on the current global state of the art in a platform which provides robustness and flexibility in both development and application**. The following main research question is formulated to reach this goal:

How can a robust and flexible computational framework be established for modelling of dielectric-barrier discharge in gaseous media?

At the end of this study, this main research question should have been answered. To do so, a number of sub-questions have been formulated to support the process:

- What discharge processes and flow interaction phenomena characterize DBD in gas?
- What are the numerical challenges in plasma modelling and what is the state of the art in literature on handling these challenges?
- What is the physical behaviour of the plasma in a 1D volume discharge and how is this influenced by physical and numerical parameters?
- What are the capabilities of the developed model and what can be expected for future work?

1.3 Methodology

The methodology on which this project is based is as following. First a literature study is conducted to get a good overview of the available knowledge, challenges and solutions in all areas related to this topic.

Next, the model is development. This is done in OpenFoam® , a C++ based open source CFD package supported by an open and active community of users and developers. The software includes many different solvers already, ranging from potential flow to combustion models. The fact that the software is open source allows for implementation of an own plasma-neutral fluid model and gives the desired flexibility in the development of the tool. The availability of a wide variety of neutral fluid dynamic solvers allows for convenient coupling between a plasma model and these neutral flow models, which provides the desired flexibility from an application perspective. Finally, many numerical schemes and solution methods implemented in OpenFoam® and used in e.g. modelling of compressible flows can also be used for modelling of electrohydrodynamic problems.

The first step is to develop the electrostatic model. This unit calculates the forcing mechanisms which drives the plasma dynamics. After that, the transport model is constructed which describes the transport through electrostatic forces undergone by the plasma species. Finally, a chemical model is developed which describes the creation and destruction of species through varies chemical reactions.

The development of the numerical model is succeeded by a verification and validation step. The units are tested individually in a 1D symmetric volume discharge set-up. For the electrostatic and transport model, exact solutions are known and errors can be quantified. Reference data is available in literature for validation of the model.

1.4 Report structure

The outcome of the literature study is presented in chapter 2, where the relevant background theory is given. This chapter should provide the reader with the sufficient knowledge on plasma, electric breakdown and discharge physics, as well as different ways of actuating the discharge and their respective fluid interaction mechanisms. The chapter is concluded with some examples of application of plasma actuators to aerodynamic problems.

Then, the physical model is presented in chapter 3, which describes the problem to be simulated by the numerical model. The working force mechanisms and discharge dynamics presented in chapter 2 are summarized and the solution domain, governing equations and analytical boundary conditions are discussed by which the problem model is described.

In chapter 4, the implementation of the numerical model is presented. The finite volume method on which OpenFoam® is based, is elaborated on and some insight is given in the solution methods utilized by the software. Then, the implementation of the governing equations is treated. Available spatial and temporal discretization schemes are discussed as well as additional schemes presented in literature. Calculation of the mobility and reaction rates of the plasma is elaborated on as well as the implementation of the boundary and initial conditions. Then, the numerical procedure of the model is laid out and the computational steps taken is explained one by one.

The verification and validation of the model is treated in chapter 5. A 1D volume discharge set-up in helium is used as a case study. The convergence behaviour of the different solver units is studied. Furthermore, the physical effects of the dielectric permittivity and non-linear effects of the surface and volume charges is evaluated. Finally, the model is validated by qualitative comparison of the solution to a reference case from literature, driven by a sinusoidal input wave form.

Finally, in chapter 6, the conclusion of this work is formulated and the main and sub-research questions will be answered. The chapter is ended with an outlook for future work; what is recommended and what can be expected.

Chapter 2

Non-equilibrium cold plasma discharge processes and flow interaction

In chapter 1, the practical relevance of DBD actuators has been reviewed. Its capability of altering the flow over its surface without any mechanically moving parts has endless applications. In this chapter, the physics behind the working of this actuator will be revealed, according to the available knowledge in literature. First, a short introduction to plasma is given in section 2.1. Second, in section 2.2 electric breakdown and discharge in gas is discussed. Then, two specific discharges will be discussed, namely the Townsend and streamer discharge, in section 2.3 and section 2.4 respectively. A specific actuator configuration is considered in section 2.5 in which the dielectric-barrier discharge (DBD) actuator is explained. This actuator has two popular actuation voltage waveforms in particular: alternating current (AC) and nanosecond (ns) pulsed, which have different effects on the neutral flow. The continuous (AC) operation yields a body force, as explained in section 2.6, while the pulsed operation results in rapid energy deposition, as explained in section 2.7. The chapter is concluded by evaluation of reported studies on macroscopic flow interaction using the formerly presented actuators in section 2.8.

2.1 Introduction to plasma

Plasma is the fourth state of matter, besides the solid, liquid and gaseous form, and is well represented in many natural phenomena such as lightning, flames, solar wind and the Northern light (Aurora Borealis). This fourth state is reached by feeding energy into a gas until molecular bonds are overcome and ionization occurs. The gas becomes ionized, meaning the medium consists of positively and negatively charged ions, free floating electrons and the remaining neutral particles. For this reason, plasmas conducts electricity as charged particles can be transported through the medium. A plasma is called neutral if the net charge is zero, i.e. the concentrations of positive and negative species balance each other out. According to

Pavón (2008), the concentration of free floating electrons determines the degree of ionization, indicated by α_p:

$$\alpha_p = \frac{n_e}{n_e + n_g}, \tag{2.1}$$

where n_e and n_g are the electron and neutral gas species densities, respectively. A plasma is said to be highly ionized when $\alpha_p > 0.1\%$ and weakly ionized when $\alpha_p < 0.1\%$. Plasma can be generated by adding thermal energy (heating of a gas) or by adding electric potential energy (applying a strong electric field). A gas can be ionized directly as well through photo-ionization, where a photon interacting with a particle can energize its electrons, e.g. by the use of a laser, up to a point where the particle is excited and the outer electron is released.

When ionization is achieved by adding thermal energy, the plasma is classified as a hot plasma, referring to the relative high temperatures ($> 5000K$ for air Peschke (2014)) required for ionization. In the case of application of an electric field or photo-ionization, the plasma is termed cold plasma, referring to the relative low temperatures required for ionization. This type of plasma can be subdivided into thermal equilibrium and non-equilibrium plasma, referring to the temperature differences between the electrons and the ions and neutrals. According to Pavón (2008), for a thermal equilibrium plasma, $T_e \simeq T_i \simeq T_n$, while for non-equilibrium, $T_e > T_i \simeq T_n$.

An import parameter in plasma physics is the Debye electron shielding length. This length indicates the distance over which the potential of a single charge drops with a factor e, which is the elementary charge, by induced transport of other charged particles. As an illustration, the electric potential induced by a free charge carrier would drop much quicker with increasing distance from the carrier in a plasma than in a vacuum. This is due to the collective behaviour of charges in a plasma: a charge carrier tends to repel carriers with the same charge and attract carriers of opposite charge, thereby effectively cancelling its own charge Nicholson (1983). The Debye length is given by the relation:

$$\lambda_{e,i} = \sqrt{\frac{T_{e,i}}{4\pi n_0 q_c^2}}. \tag{2.2}$$

In aerodynamics, hot plasma is relevant mainly in hypersonic aerodynamics, where shocks can cause extreme temperature rises generating chemically reacting, thermally imperfect gas flow. Cold plasma, on the other hand, can be generated in a more controlled manner and used for active flow control in any flow regime. This plasma is usually generated through gas discharge, where a voltage potential difference between two electrodes initiates a breakdown, which in its turn leads to a current. Generally, two types of current are distinguished: conduction and displacement current Jackson and Fox (1999). The first is simply due to transport of charge carriers:

$$\nabla \cdot \vec{J}_{cond} + \frac{\partial \rho_c}{\partial t} = 0, \tag{2.3}$$

in which J_{cond} is the conduction current and rho_c the charge volume density. The charge volume density is made up from free charge carriers, of which their number densities are determined by convection, diffusion and chemical reactions, creating or destroying species according to their corresponding reaction rates. The displacement current is due to change in the electric field, for example in a fluctuating electric field:

$$\vec{J}_{disp} = \frac{\partial \varepsilon \vec{E}}{\partial t}. \tag{2.4}$$

In this relation, J_{disp} is the displacement current, for a dielectric material with relative permittivity ε_d, $\varepsilon = \varepsilon_d \varepsilon_0$ is the dielectric permittivity and $\vec{E}$ is the electric field vector. Both current types can be used to quantify the plasma, and more specifically the strength of the discharge.

In the next section, more insight will be given in the generation of gas discharge in general, and different classifications and their properties used in aerodynamics specifically.

2.2 Electric discharge in a gas

In the former chapter, the plasma state of matter has been introduced and some examples of generating plasma have been given. In this chapter, specifically gas discharge as a way of generating plasma will be discussed as it currently is the most popular way of intentionally generating ionized flow.

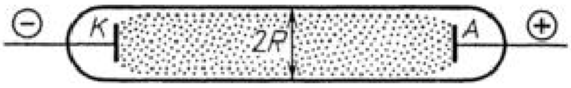

Figure 2.1: Gas discharge tube Raizer and Allen (1997).

The discharge referred to here is the current resulting from two electrodes or capacitors with a voltage potential between them. An electric current is the transportation of charged particles, in this case through a gas. To explain the processes concerned with this discharge, a volume discharge will be considered, which includes two opposing, parallel electrodes separated by a gas spacing d. We consider the volume to be filled with gas at both high and low pressures.

Vacuum is not considered here. The applied voltage potential is constant. The set-up is presented in Figure 2.1.

Most gases are well known to be good insulators, but under certain circumstances such media can become conductors, allowing a discharge between the two electrodes. Multiple discharge regimes exist, depending on the applied voltage and the resulting current density through the gas, as depicted in Figure 2.2. Besides its dependency on the voltage, the current density can be controlled by altering the gas type and pressure, the spacing between the electrodes and their respective configuration.

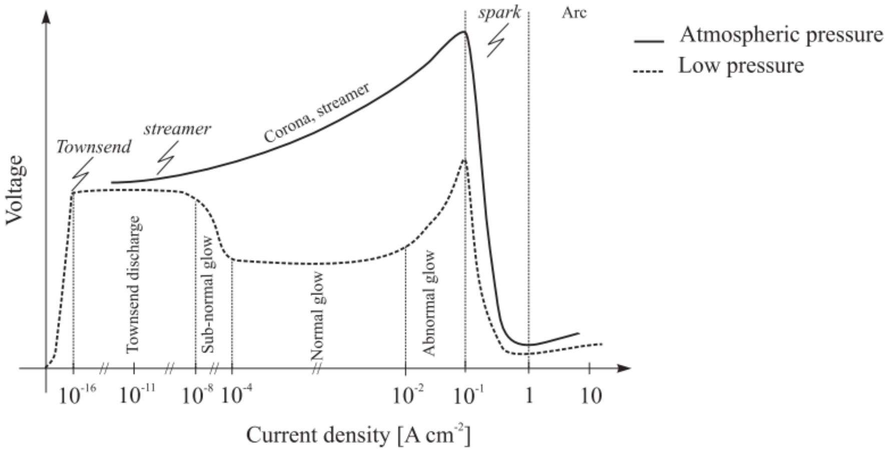

Figure 2.2: Gas discharge regimes Meek and Craggs (1953).

The discharge types considered here are stable or quasi-stable processes and are preceded by a transient process called a breakdown. When considering the set-up displayed in Figure 2.1 with a steadily increasing voltage potential starting from zero, the first identified discharge to occur is the **Townsend** discharge, preceded by the Townsend breakdown, or electron avalanche. The discharge is characterized by a low voltage, low current and is not self-sustaining. At low pressures, this Townsend breakdown can develop through secondary electron emission into a sustained discharge with higher currents at lower input voltages. These discharges are characterized by radiating photons in the visible spectrum, producing a glow for which they are termed **glow** discharge. For higher pressures (around atmospheric values), a much higher breakdown voltage V_{br} is required due to the isolating properties of the denser air. Similarly to the glow discharge, when secondary electron emission occurs, the Townsend breakdown transits into a sustained discharge called a **corona** discharge. The corona discharge differs from its low-pressure counterpart by the occurrence of a complementary electron seeding process, called photo-ionization, where additional ionization occurs by the radiation of photons from excited radicals in the plasma. Alternatively, the Townsend breakdown initiates a **streamer** breakdown, which evolves if a sufficiently high over-voltage is applied. When for all pressures the initialized discharge is able to undergo a **spark** breakdown, the discharge evolves into an **arc** discharge. This type of discharge is typical for its high current density and can be sustained at relative low voltages. Arc discharges occur when the ionized region reaches from the anode to the cathode and a closed circuit is formed. This can be prevented by setting up a **dielectric barrier** discharge, as explained in section 2.5.

First, the types of discharge most relevant for flow control are discussed below. More insight is given in the process of the electron avalanche and its transition into a sustained (corona) discharge in section 2.3. Thereafter, the streamer breakdown and discharge is elaborated on in section 2.4. Please note that all processes explained in the next sessions are generated in the geometric set-up as presented in Figure 2.1.

2.3 Townsend breakdown

The fundamental discharge type is the Townsend discharge. This discharge is characterized by its very low current densities and is also known as the Townsend avalanche. External sources such as cosmic radiation provide free charge carriers, such as electrons, which are accelerated by the electric field. This causes an initial low current. If the strength of the electric field between the electrodes is sufficient, which occurs at the breakdown voltage V_{br}, the electrons can pick up velocities which allow for inelastic collisions with neutral particles, thereby releasing another electron and leaving a positively charged ion. This newly freed electron can do the same with another neutral particle, through which the number of electrons increases exponentially in space as visualized in Figure 2.3. This phenomenon is called an electron avalanche and is the primary breakdown process.

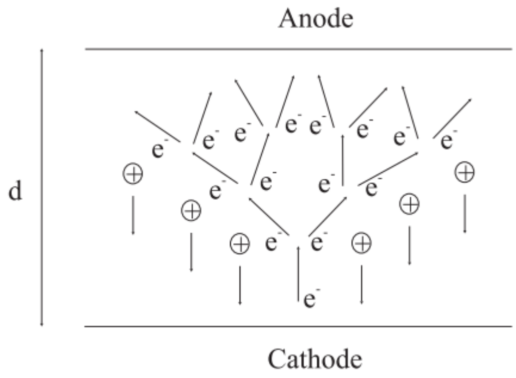

Figure 2.3: Free electron exponential growth in electrode gap Pavón (2008).

The remaining ions are charged, meaning they respond to the electric field as well. The resulting current of this process is termed a Townsend discharge, and terminates directly if the electric field strength is sufficiently low. On the other hand, if the electric field strength is sufficiently high, heavy species collide upon the cathode with sufficient velocity to release new electrons. This is called secondary electron emission and according to Pavón (2008), can be enhanced by photo-ionization or photon bombardment. When this secondary electron emission takes place, the current is self-sustaining and the discharge transforms into a corona discharge. The condition determining whether a current is self-sustained can be derived as follows. The Townsend ionization factor α is defined as:

$$\alpha = \frac{1}{n_e}\frac{dn_e}{dx}.$$

Which states that the ionization factor is given by the relative increase of the electron particle density per increase in distance. Integrating over x yields:

$$n_e(x) = n_{e0}e^{\alpha x},$$

meaning that at the cathode $e^{\alpha d}$ electrons are freed for every single seed electron, neglecting recombination or binding to electronegative molecules. As explained, in a sufficient strong electric field, resulting positive ions collide with the negative electrode, potentially releasing $\gamma(e^{\alpha d} - 1)$ electrons, where γ is the probability that the ion-electrode collision releases an electron. This probability factor depends on the gas type, cathode material, surface conditions, reduced electric field E/N and the measure of photo-ionization photon bombardment of the cathode. If a single electron is released, the current is said to be self-sustaining, so the breakdown condition therefore is:

$$\gamma(e^{\alpha d} - 1) \geq 1,$$

and takes place at a voltage higher than the breakdown voltage V_{br}. Empirical relations exist for this breakdown voltage as a function of the product of the gas pressure P_g and the electrode spacing d, called the gap-pressure-product. One of such relations is given by (Paschen (1889); Pavón (2008)):

$$V_{br} = \frac{BP_{gas}d}{ln(AP_{gas}d) - ln[ln(\frac{1}{\gamma}) + 1]},$$

where constants A and B depend on the gas type and stem from curve-fits for the Townsend ionization of the form:

$$\alpha = A\exp(B/(E/p)^r$$

The factor r has the value of 0.5 and 1 for atomic and moceluar gases, respectively. The meaning of the reduced electric field E/p will be explained later. This relation as well as values for A, B and r for different gases can be found in the work of Ward (1962). To continue, for air, the curve is presented in Figure 2.4:

Simply, the voltage region above the curve results in a breakdown process, while the region below the curve will not. For higher values of the product, a higher voltage is required for breakdown. This can be physically explained as follows: for increasing values of d, the generated characteristic electric field strength decreases ($\bar{E} \propto V/d$), lowering the characteristic electron velocity ($\bar{U} \propto \bar{E}$), and electrons will not have the kinetic energy to initiate an electron avalanche. Similarly, when the gas pressure is increased, the mean free particle path reduces ($\lambda \propto 1/P_g$). If an electron is not able to accelerate sufficiently before colliding with another particle, it also won't be able to gain the required kinetic energy to initiate breakdown. Increment of either of the parameters result in an increase in the product, and a higher V_{br} is required.

A small note is added regarding the mean free path, also the characteristic plasma length scale which is equal to the mean free path λ and scales with $\propto 1/N_g$ ($P_g \propto N_g$). When considering DBD modelling used for flow interaction, it must be taken into account that for most fluid models, the medium is considered a continuum, i.e. $Kn = \lambda/L \ll 1$. This implies that $\lambda \ll L$. Since N_g is proportional to $\propto P_g$, only medium to high pressure gases can be considered.

Instead of this pressure-gap-product, it is more common to use another similarity parameter called the reduced electric field, E/N:

$$E/N = \frac{|\vec{E}|}{N_g} \times 10^{21} [\text{Td}] \tag{2.5}$$

This parameter normalizes the local electric field strength over the initial gas number density, which makes it a local function of the ratio $V/(P_g \cdot d)$. The unit is given in Townsend (Td) and equals $10^{-21} V \cdot m^2$. Whenever two plasmas have equal reduced electric field distributions, the plasmas are said to be similar.

Concluding this section, the Townsend discharge requires free seed electrons (generally pro-

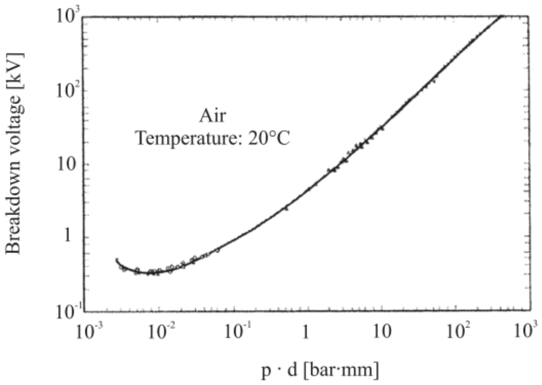

Figure 2.4: Breakdown voltage dependency on the socalled pressure-gap-product Pavón (2008).

vided by external sources, such as cosmic radiation) and the breakdown is initiated by gradually increasing the voltage to the breakdown voltage V_{br}, until an electron avalanche occurs. The breakdown then leads to a discharge, which is sustained whenever the breakdown condition is met and secondary electron emissions are released. In the next section, the streamer breakdown process will be explained.

2.4 Streamer breakdown and discharge

In case of a sufficiently high reduced electric field E/N, the electron avalanche initiates a different type of breakdown, called a streamer breakdown. A Townsend breakdown can develop into a glow or corona discharge when secondary electron emission occurs. For high values of E/N, the electron avalanche develops too quickly (in the order of nanoseconds) for this to happen. Another fundamental difference with a Townsend breakdown is the fact that the resulting electron avalanche is so strong, it causes an exceeding of the critical number of free electrons in the electrode gap. The critical number refers to the upper limit of free electrons, beyond which a space charge is induced that distorts the local electric field Meek and Craggs (1953). What then happens is the following:

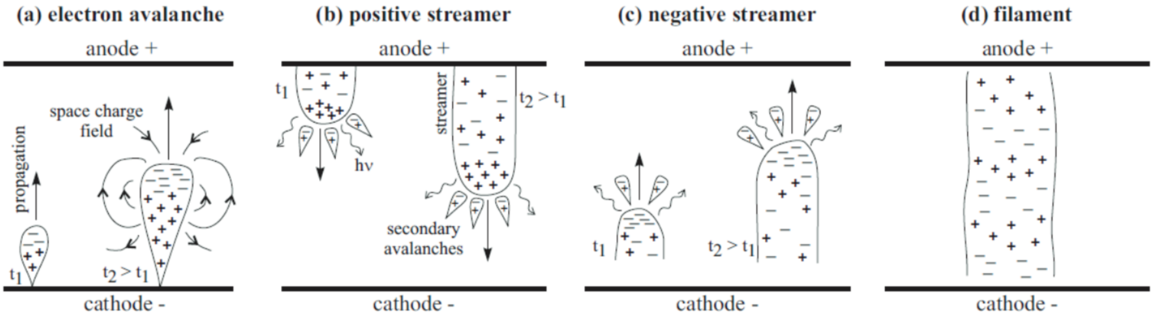
(a) electron avalanche **(b) positive streamer** **(c) negative streamer** **(d) filament**

Figure 2.5: Formation of a streamer (Raizer and Allen (1997)).

a Similarly to the Townsend breakdown, an electron avalanche is formed initiated by free electrons, as illustrated in Figure 2.5. The electrons released by impact ionization accumulate at the front of the avalanche, polarizing the avalanche. The critical number of free electrons is exceeded and a local electric field, stronger than the applied electric field, is induced due to the accumulated space charge. This is an important aspect, as the local induced electric field ionizes the surrounding neutral particles, which facilitates growth and propagation of the streamer. This process is the formation of the streamer head.

b For moderate gaps and voltages, the initial avalanche has reached the anode before the streamer head has been formed. The electrons are absorbed by the anode, leaving a cloud of positively charged ions behind, which then forms the streamer head. This induces a positive local electric field. Secondary avalanches are initiated by photo-ionization, which feed the required electrons. The transported electrons again leave behind positive ions, and the streamer propagates towards the cathode. A current has formed inside the streamer, feeding electrons collected at the streamer head towards the anode. This is called a positive streamer, corresponding to the charge of the streamer head.

c For large gaps and high voltages, the initial avalanche has not reached the anode yet, but exceeds the critical number of free electrons in the electrode gap. Similarly though, a streamer head is formed consisting of accumulated particles, this time the negatively charged electrons. The streamer head propagates towards the anode, while an electron current is induced by the idle positive ions, following the streamer head and feeding the streamer. This is called a negative streamer.

d Regardless of the direction, a significant amount of charged particles is transported resulting in a discharge current. The streamer is characterized by its slim, filament shape between the electrodes. This type of discharge is therefore also called filamentary discharge.

Now the chief breakdown and discharge processes have been discussed applicable to flow control, it is time to consider a different geometric set-up.

2.5 Dielectric-barrier discharge

In the former sections, a volume discharge set-up with a constant voltage potential was considered to explain the resulting plasma processes. Other geometries can be utilized too, where a specific kind of configuration is the dielectric-barrier discharge (DBD). This kind of discharge is fundamentally different from the test case as presented in Figure 2.6 by a dielectric layer separating the two electrodes (Kotsonis (2015)), and (in this study) the discharge not taking place in between the electrodes, but on the surface, for which it also is called a surface DBD (SDBD). A dielectric is simply a piece of polarizing, insulating material placed between two capacitors in order to prevent the generated discharge (corona or streamer) to evolve into an arc discharge. Please note that in some studies, the dielectric is just separating the two exposed electrodes, whereas in this study, the dielectric encapsulates the lower (ground) electrode entirely.

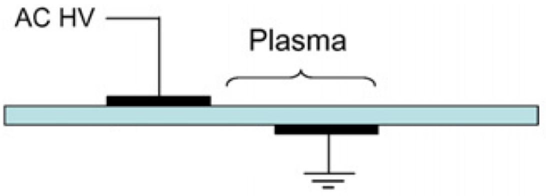

Figure 2.6: Set up of a surface DBD, with a high voltage (HV) exposed electrode (anode) and a burried ground electrode (cathode) Moreau (2007).

When placed in an electric field, the net neutral but polar molecules orientate according to the electric field. At the boundaries, i.e. the surfaces of the dielectric, a net charge occurs. This net charge at first stores the electric field: the exposed dielectric surface takes on a surface charge opposing the anode charge. Over time though, free charge carriers are attracted to the surface, accumulating on the surface and thereby reducing the effective potential. This generally leads to termination of the discharge process when a constant direct current is applied since at some point, the electric field will be reduced until discharge cannot be sustained. This configuration therefore requires usage of increasing direct current or alternating input current wave forms, such as a sinusoidal waveform or a pulsed waveform (step or saw tooth function), to re-initiate the breakdown once the accumulated surface charge has become too strong. The different operating types are discussed in section 2.6 and section 2.7.

Dielectric-barrier discharge is characterized by a number of processes, all of which according to a certain time scale (Jayaraman et al. (2007)). First of all, many different time scales exist for the discharge process alone (flow interaction not considered). The following time scaling parameters with indicated order of magnitude can be distinguished.

Table 2.1: Characteristic time scales in DBD (Jayaraman et al. (2007)).

Process	**Time scale**	**Order of magnitude**
Operating frequency	$\tau_w = \frac{1}{f}$	$= \mathcal{O}(T)$
Ion drift	$\tau_{dr,ion} = \frac{L}{V_{ion}}$	$= \mathcal{O}(T10^{-4})$
Electron drift	$\tau_{dr,e} = \frac{L}{V_e}$	$= \mathcal{O}(T10^{-6})$
Dielectric relaxation	$\tau_{diel} = \frac{\epsilon_0}{eV_e}\frac{E}{N}$	$= \mathcal{O}(T10^{-7})$
Ionization frequency	$\tau_c = \frac{1}{v_c}$	$= \mathcal{O}(T10^{-6})$

As was mentioned earlier in this section, different actuation signals can be used for operating a DBD actuator, as a constant voltage potential won't yield a sustained plasma. More specifically, for flow control, two types are favored most above all: the continuous alternating current operation (ACDBD) and the pulsed nanosecond operation (nsDBD). The AC-DBD is characterized by a continuous sinusoidal high-voltage waveform with frequencies in the kilohertz range, through which momentum is transferred from ions to neutral gas molecules Unfer and Boeuf (2010). This will be elaborated more in the next section. The nsDBD actuates high-voltage pulses with a duration in the order of nanoseconds, injecting energy into the neutral gas on a very short time scale which in turn generates shock waves. This type of actuation is treated in section 2.7.

2.6 Body forces in continuous actuator operation

It has already been explained that the charge accumulation on the dielectric surface opposes the anode voltage, thereby quenching the electric field. A constant direct current cannot sustain the plasma. By alternating the high-voltage potential, the potential difference is reversed and the electric field is restored. What then follows is a corona discharge responsible for a carrier current, with incidentally streamers occurring during the full pulse. An experimentally obtained data set is shown in Figure 2.7.

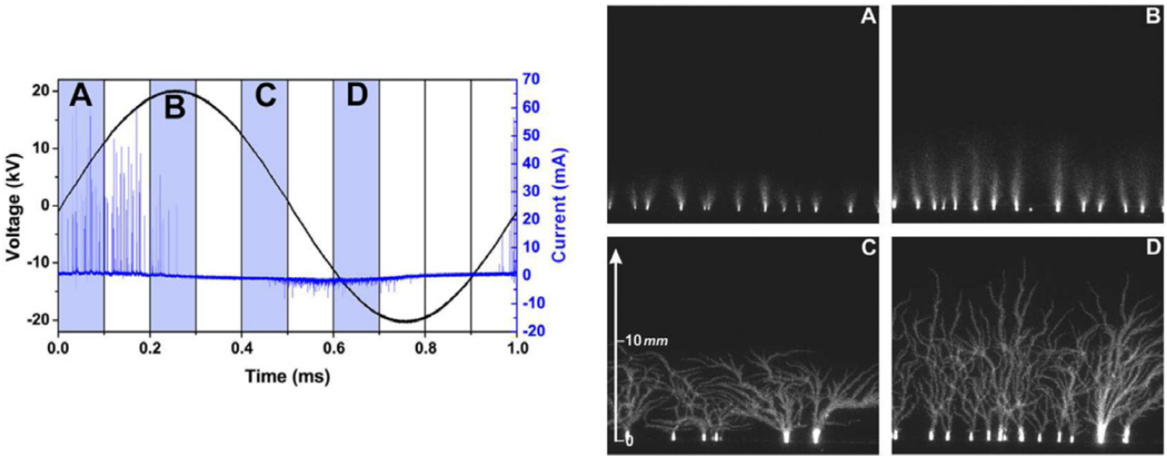

Figure 2.7: Example experimentally obtained voltage (black) and current (blue) waveforms for a DBD, with fast-imaging of the created plasma Benard and Moreau (2013).

The streamer discharges can be identified by the short current pulses in the current waveform. The voltage waveform is generally broken down into the rise phase and the decay phase, or the positive half-cycle and the negative half-cycle, as each cycle-half generates a different plasma and discharge current. During the positive half-cycle, streamer discharges were found to happen in rapid, irregular succession indicated by the high number of current spikes in the current graph. Corona discharge occurs close to the anode, visible from the bright spots in the plasma imaging. Electrons are drawn to the exposed electrode and positive streamers are formed, visible by the outskirts of those bright spots. The streamer discharges are characterised by their high current amplitude, but sparse temporal distribution. During the negative half-cycle, the plasma is characterised by corona regions which spread widely away from the exposed electrode Benard and Moreau (2013). The fundamental difference between the two cycle-halves is the infinite number of available electrons to the plasma during the negative half-cycle (exposed electrode functions as a cathode), assuming the electric field is strong enough for the cathode to emit electrons. During the positive half-cycle, the available electrons is limited to the built-up concentration on the dielectric surface and the secondarily emitted electrons Enloe et al. (2004).

The main flow interaction induced by the sinusoidal waveform actuation is momentum transfer from drifting ionized particles caught by the electric field resulting from the voltage potential to the neutral gas, which is felt by the gas as a body force. All along a voltage cycle, the EHD force is pointed away from the exposed electrode tip. This means that during the positive half of the voltage wave, the momentum transfer by positive ions is dominant, while during the negative half of the cycle, negative ion momentum transfer is dominant. Spatial and temporal force distribution differs per half, though, as can be seen clearly in Figure 2.8. Also, the local body force may not necessarily always point away from the tip, as is the case in the negative phase in close proximity to the electrode tip (red color in the figure) Boeuf et al. (2009). Furthermore, voltage amplitude and frequency influence the force density and coverage, such that for two difference input voltage waveforms, the integrated body force may be the same for two cases, but the effect on the flow may not.

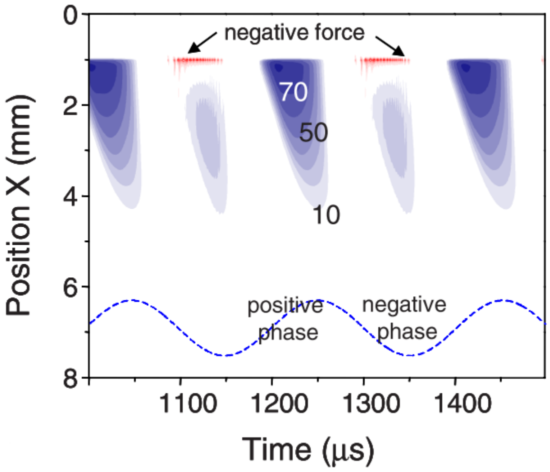

Figure 2.8: Calculated temporal distribution of the EHD body force parallel to the dielectric surface Boeuf et al. (2009). Blue indicates a positive force (away from the electrode tip) while red indicates a negative force.

The resulting body force term F_{EHD} has been formulated to different extents, but are all related to one another. The most extensive formulation is given by Unfer and Boeuf (2010); Abdollahzadeh et al. (2014); Goekce (2014); Abdollahzadeh et al. (2016):

$$\vec{F}_{EHD} = e(n_p - n_e - n_n)\vec{E} - \sum_{k=e,n,p} \nabla k_b T_k n_k \tag{2.6}$$

The first term is the momentum transfer by charged particle drift driven by the electric field. The second term is the diffusion term due to species concentration gradients. In general, the Coulomb force (drift term) accounts for the larger order which may lead to neglect of the diffusion term when only the order of magnitude of the force is of interest Goekce (2014).

A final important point stressed, which leads directly to the next section, is the fact that the corona discharge is chiefly responsible for the EHD force, whereas the streamer discharges only cause aeroacoustic noise in the form of acoustic waves, caused by the heat released by the streamers Unfer and Boeuf (2010). This is the purpose of development of nsDBD, where the EHD force effect is abandoned and this aeroacoustic effect is exploited for flow control purposes. This will be explained in the next section.

2.7 Energy deposition in pulsed nanosecond actuator operation

Where the continuous operated actuator mainly inflicts a body force on the neutral gas, a pulsed nanosecond actuator profoundly causes rapid energy deposition into the neutral gas, leading to aeroacoustic disturbances in the form of acoustic waves. As has been demonstrated in section 2.6, streamer discharges only occur during the positive voltage half-phase, during rapid rise of the voltage amplitude (Unfer and Boeuf, 2010). The streamer discharges can be concentrated in time and increased in current amplitude by applying a pulse with a rise time in the order of nanoseconds. The streamers then form at high over-voltages, leading to considerable power deposition.

The effects of this power deposition on the flow is visualized in Figure 2.9. The energy deposition happens in proximity to the electrode tip and over the covered electrode. This creates a local high pressure region, which starts to propagate through the gas. The cylindrical wave is formed by the energy deposition at the tip, also called a 'hot spot', which is strongest. The plateau is formed by propagation of the streamers in positive x-direction. Because of diversity in strength and propagation length of the streamers, the total energy deposition away from the tip is lower, yielding the characteristic tail of the shock wave.

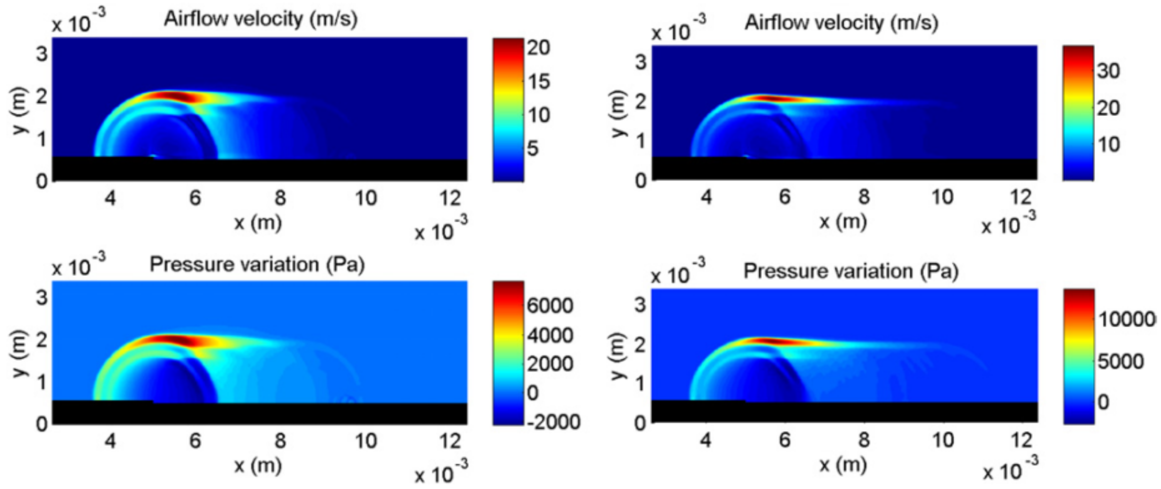

Figure 2.9: Shockwave formation after nanosecond pulsed actuation of a DBD actuator. The shock wave is characterized by the circular wave around the tip, with a tail above the covered electrode ((Unfer and Boeuf, 2010)).

Starikovskii et al. (2009) investigated the characteristics of the shock wave and concluded the following. The initial expansion wave moves away from the surface with approximately Mach 1.13. Simultaneously, a rarefaction wave travels towards the surface, is reflected and catches up with expansion wave. After interaction, the expansion wave is slowed down to Mach 1. From comparison between cathode- and anode directed discharges, i.e. positive and negative over-voltage on the exposed electrode respectively, it was concluded that cathode-directed discharge leads to greater energy deposition.

To investigate the exact order in which energy is released during a complete pulse cycle, (Unfer and Boeuf, 2009) depicts how the current behaves. A plot indicating the current development from their work is shown in Figure 2.10. As can be seen, two major pulses can be distinguished. According to the authors, the current rises at the same moment the applied voltage is increased, until the dielectric surface has been charged sufficiently and the effective electric field is reduced sufficiently to decrease the current. The current rise recovers, though, due to the continuous applied voltage increment, until the applied voltage takes on a constant value. Until now, the exposed electrode has functioned as anode, meaning the dielectric has been charged positively by accumulation of free charge carriers inside the plasma. Because of this, the effective electric field reduces, and so does the discharge current. The potential relaxes in an exponential decay, until the applied potential is decreased. During this decay, the potential between the electrode, which is still charged positively, soon becomes less than the potential on the dielectric surface, which causes a negative discharge current as the exposed electrode functions as a cathode. The current steadily increases, until the applied voltage reaches null. The dielectric surface is still positively charged, but relaxes such that the negative current increases back to zero.

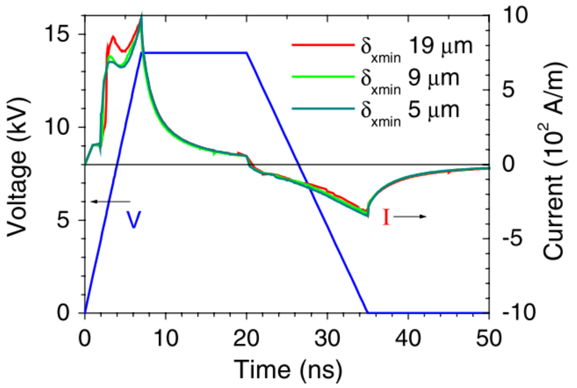

Figure 2.10: Current waveform of a nanosecond DBD (Unfer and Boeuf (2009)).

During a single streamer discharge, energy is deposited into the neutral gas. According to Unfer and Boeuf (2009), this energy transfer originates from a number of processes. First of all is the energy transfer through ion-neutral molecule collisions, also known as Joule heating. The transported charge carriers which make up the current collide with neutral particles, during which it is assumed that the energy from the charge carrier is transferred totally and instantaneously into neutral particle thermal energy. This relation is given by:

$$p_{ions} = (\vec{J}_p - \vec{J}_n) \cdot \vec{E}. \tag{2.7}$$

This relation describes the energy transferred from the electric field to the neutral gas through the induced positive and negative ion current, indicated by $\vec{J}_p$ and $\vec{J}_n$ respectively.

The second contribution is due to direct thermal energy transfer from electrons to neutral particles, driven by elastic and rotational excitation (el-R), vibrational-translational relaxation (VT) and electronic excitation (E). The transfer through elastic collisions and rotational excitation represents a fraction of the total energy gained by electrons through the electric field. This latter term is the electron power density p_{elec}:

$$p_{elec} = \sigma_e |E|^2 \tag{2.8}$$

Where σ_e is the electron conductivity and is given by $\sigma_e = e\mu_e$ (Benilov and Naidis (2005)). Unfer and Boeuf (2009) explains that energy transfer in other degrees of freedom, i.e. vibrational relaxation (VT) and electronic excitation (E), have different process time scales. A phenomenological model is then formulated based on the generally shared observation in literature (Popov (2001); Guerra et al. (2004); Flitti and Pancheshnyi (2009)) that energy spent by electrons to excite N_2 by quenching of the states by oxygen molecules (i.e. recombination) is released very rapidly compared to other processes. This then allows for the assumption that this energy release happens instantaneously. Furthermore, it is assumed that not all of this energy is released, but that only 30% is absorbed by the neutral gas. The only process which then operates on a different time scale is relaxation of vibrational and translational energy (VT), for phenomenological relation formulated:

$$\frac{\partial p_{VT}}{\partial t} + \frac{1}{\tau_{VT}} p_{VT} = \frac{1}{\tau_{VT}} \eta_V p_{elec}. \tag{2.9}$$

This relation simply states the appropriate scaling of p_{VT} from the characteristic relaxation time scale τ_{VT} to the current time scale t, determined by the fraction of the energy absorbed by the electrons from the electric field $\eta_V p_{elec}$.

The total amount of heat released is then given by the sum of the partial power terms:

$$\begin{aligned} p_{th,e} &= (p_{el-R} + p_{VT} + p_E) + p_{ions} \\ &= p_{VT} + (\eta_{el-R} + \xi \eta_E) p_{elec} + p_{ions}. \end{aligned} \tag{2.10}$$

The values of p_{VT} and p_{ions} is found through Equation 2.9 and Equation 2.7, respectively. ξ has a value of 30% and the fractions η_{el-R}, η_E and η_{VT} can be found by solving the Boltzmann equation, often by using the Bolsig+ software Hagelaar and Pitchford (2005).

2.8 DBD induced flow interaction

DBD actuators have been developed for their flow interaction capabilities. In the former chapter, it has been discussed that body forces and energy deposition applies depending on the type of actuation: AC or nanosecond DBD. Both actuation types, body force and energy deposition, will interact with the surrounding flow differently per case. Kotsonis (2015) has summed up the chief applications for which DBD actuators have been investigated so far:

- Separation control;
- Laminar-turbulent transition delay;
- Lift enhancement and drag reduction;
- Shock wave control;
- Combustion augmentation.

As can be seen, the ability of a device to produce a wall jet or a weak shock wave results in a great variety of applications. In this chapter, each topic will be discussed independently. It should be emphasized that there has been much work done on AC-DBD actuators, where the main effect is a body force, while not so much has been done on nsDBD, which mainly induces thermal effects. This is believed to be so because of the relative young popularity of the nanosecond operation mode (Likhanskii et al. (2006); Starikovskii (2005), while the continuous operation mode has been of interest for a longer time now (Roth (1998)). The actuation mode relying on the production of a wall jet seems limited in its application to low velocity flows, above which the wall jet velocity becomes insignificant. Likhanskii et al. (2008) already reported a limited range of 0-30 m/s. Since the nanosecond pulsed operation relies on thermal effects, it can also be applied for flow control higher up in the Mach regime. An example of this is shock wave control, which will be discussed in one of the sections below.

2.8.1 Separation and transition control

Separation control is a major topic for lift conservation over airfoils, but also for drag control. Post and Corke (2004) set up an experiment whereby an AC-DBD was used to reattach separated leading-edge flow over a generic airfoil, with an angle of attack 8 degrees beyond stall. Little explanation is given for the exact working principle of the stall recovery, but the actuator, which produces a 2D jet at the wall in the direction of the flow, is said to add momentum to the boundary layer, preventing a negative boundary layer velocity gradient. Similar results are found by Huang et al. (2006), who found that the momentum addition reduces the adverse pressure gradient, thereby postponing the separation point.

Little et al. (2010) not only looked at separation delay, but also at lift enhancement by manipulation of oscillating flow phenomena. As was the case in the work mentioned above, the direct effect of the AC-DBD is assumed to be a steady wall jet, which can be interpreted as a quasi-steady phenomenon. Little et al. (2010) managed to increase lift, regardless of the controlled separation, by amplifying the natural instabilities associated with vortices shedding from the flap shoulder by emulating the low shedding frequency with the plasma actuation carrier frequency. This confirms that a second effect induced by the actuator exists:

interaction between the operation frequency of the actuator and the frequency of the natural instability. As Glezer et al. (2005) puts it, lift can be manipulated by damping the large-scale trailing edge vortex shedding into the wake, which affects the overall circulation all around an air foil.

Later in continuous work, Little et al. (2012) performed similar experiments, using a nanosecond driven DBD. The resulting weak shock wave, created by the rapid energy deposition by the plasma actuator, is thought to trip the flow at pre-stall angles of attack. Transition is forced and the air remains attached over a longer distance over the air foil. During post-stall, effects are assumed to be induced similar to the ones occurring when an AC-DBD is used. Coherent span wise vortices are generated by manipulation of flow instabilities, which are known for their effective role in separation control. The effects are most apparent in the range of $F^+ = 4 - 6$, where F^+ is defined as a non-dimensional frequency $F^+ = \frac{f x_{sep}}{U_\infty}$.

The aforementioned authors have all addressed the topic of flow separation over a wing. Additionally, these devices can be used to influence the laminar-turbulent transition process. Grundmann and Tropea (2008) studied the natural transition process by introducing Tollmien-Schlichting waves over a flat surface. These waves were then cancelled by means of an AC-DBD actuator operated in pulse mode. While the boundary layer velocity profile was not affected significantly, the turbulence level was, up to 20-30% amplitude of the uncontrolled oscillation amplitudes.

2.8.2 Lift enhancement, drag reduction and noise mitigation

The applications of the work described in the former section was of a very fundamental nature. Transition and separation control are mostly means for controlling stall, lift and drag. Studying these effects in an isolated and generic test case is of great importance though, to reach better understanding of the fundamental interaction with the flow. Other authors have presented work of a more applied nature.

Thomas et al. (2008) took the problem of landing gear noise and investigated the mitigation of such noise through plasma actuated flow control. Their work involved experiments on a cylinder with mounted DBD actuators. The initial aim was to reduce noise, successfully reducing the sound pressure levels of the frequency band associated with wake vortex shedding by 13.3 dB.

Another application to aircraft aerodynamics is that of optimization of high-lift devices. He et al. (2009) mimicked the effects of a slat and flap by replacing them with two plasma actuators mounted on a NACA0015 air foil. It is reported that the trailing-edge actuator was found to produce the same effect as the flap in the sense of a uniform positive shift of the $C_{L_{\alpha_0}}$ lift coefficient, while the leading-edge actuator increased the lift-to-drag ratio up to a 340%.

In another study, Nati et al. (2013) investigated the suppression of vortex shedding from the trailing edge of a rectangular trailing edge. Using a new configuration called 'transverse actuation', successfully reducing the total kinetic energy of the fluctuating component of the velocity field with 60%, while the energy contained in the Von Kármán vortices was reduced by a factor 6 for low velocity flows ($< 7m/s$).

2.8.3 Shock wave control

The nsDBD produces a weak shock wave due to rapid energy deposition from the plasma into the neutral air during discharge. Shock wave interaction is a well known phenomena in supersonic and hypersonic aerodynamics. Nishihara et al. (2011) used a phase-locked Schlieren imaging technique to capture and analyse the interaction between a Mach 5 bow shock and a weak shock wave produced at the leading edge of a cylinder by a nsDBD. It was observed that the shock wave travels up stream, interfering with the bow shock, increasing the stand-off distance by up to 25%. It is noted that the main advantage of using a nsDBD is the low power budget compared to other methods.

2.8.4 Combustion augmentation

The highly reactive processes during a nsDBD can be exploited for other purposes than aerodynamic control. During combustion, complex chemistry plays an important role, for which nsDBD can be used to enhance processes or provide reactants, such as ozone. Starikovskaia (2014) makes the distinction between plasma-assisted ignition (PAI) and plasma-assisted combustion (PAC). Ignition is the process to initiate combustion, an irreversible chemical process during which heat is released. Since a spark is also a plasma, PAI has basically been used in the form of spark discharge since the first internal combustion engine in 1858. Starikovskaia (2014) describes the main effect of a spark discharge as local gas heating and the resulting combustion wave which then propagates through the fuel-oxidizer mixture. Using non-equilibrium plasma to increase the internal energies (excitation of internal degrees of freedom) of the present species may be much more effective than purely releasing local thermal heat. An example of PAC is the production of ozone as a catalytic species to intensify the combustion process as more oxygen atoms are present in the mixture.

Chapter 3

Description of the physical model

In this chapter, the physical model description of this work relevant to DBD physics is given. This model will form the basis of the numerical work presented in the next chapter, and its description focuses on plasma physics related to discharge dynamics only. Furthermore, an introduction is given to coupling terms governing the dynamics between the discharge and fluid flow, although a fluid model to solve for said flow dynamics is not included. The flow dynamics related to or with influence on the physics treated here are left for future work.

In section 3.1, the model problem is presented, together with relevant actuator geometries defining the solution domain. Then, in section 3.2 the governing equations applicable to this model problem are derived. Boundary and initial conditions are then discussed in section 3.3. Mathematical formulation of the interaction of the plasma with the neutral parent gas is described in section 3.3. Finally, a summary of the physical model is given in section 3.5.

3.1 Model problem and solution domain

First, the physical problem problem and its solution domain are introduced. In short, the discharge physics treated in the last chapter involves production of plasma containing electrons and charged species of the parent gas undergoing chemical reactions, such as impact- and photo-ionization, attachment and recombination. The driving force mechanism behind these processes is the electric field created between two electrodes by applying a voltage potential difference. Only dielectric-barrier discharge at atmospheric pressure is considered, yielding glow or streamer discharges, depending on the input voltage and the geometry configuration.

Two geometric configurations are considered here: a 1D volume discharge and a 2D surface discharge. Both types of configuration involve at least two electrodes, a dielectric layer and a gaseous region. The dielectric material is shielding at least one of the electrodes from the plasma, which prevents transition from any type of discharge into an arc discharge, as explained in chapter 2. The volume configuration, depicted in Figure 3.1, is symmetric and involves dielectric material on both electrodes. For convenience, the upper electrode is called the anode as its voltage is controlled, even though this voltage can be both positive and negative. The ground electrode is called the cathode and its electric potential is always zero. The gap width of such actuators varies and is generally in the order of cm, while the dielectric layers are in the order of 10^{-1}mm. The discharge of such actuators is often designed to be 1D by using a circular actuator. The domain width as therefore arbitrary.

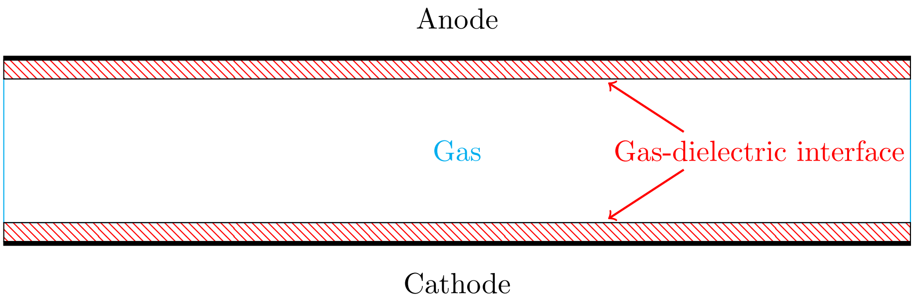

Figure 3.1: Geometry of a volume DBD actuator.

In Figure 3.2, a typical surface DBD actuator configuration is depicted. The cyan bounds indicate the far field of the fluid domain. The red bounds enclose the dielectric domain, while the black bounds enclose the electrode domains. The control volume is bounded by the left edge of the anode, the right edge of the cathode, the lower side of the cathode and the upper fluid bound at an arbitrary distance from the dielectric. This distance should be sufficient such that the far field assumption on the upper boundary is valid. Similarly to the upper boundary, in case of a relative short anode, the left boundary is extended to assure that the far field assumption is valid here as well. Similarly to the 1D geometry, the dielectric layer is often in the order of 10^{-1}mm, while the cathode length can reach up to several mm. The anode is usually of the same length, or a factor 1-5 shorter than the cathode.

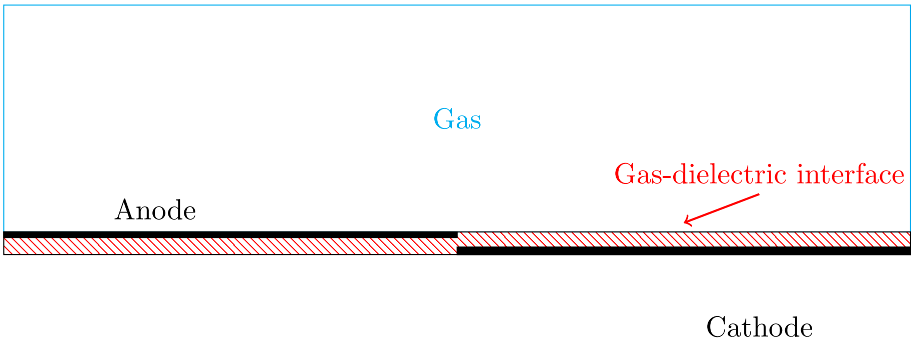

Figure 3.2: Geometry of a surface DBD actuator.

The different materials involved in this problem make it a multi-media problem, introducing additional surface processes. Also, solution of the particle dynamics is only relevant in the gas domain, but the electric field is continuous through all regions. For the electric field, this requires coupling conditions between the different regions. These conditions will be explained in section 3.3. Next, the equations governing this model problem are treated.

3.2 Governing equations

The model problem includes electrostatics and charged particle flow dynamics. The gas is considered to have an atmospheric pressure, and so the medium as well as the plasma can be assumed to behave as a continuum, to which continuity and momentum equations can be applied. The electromagnetic effects are ignored in this study. The driving mechanism behind the plasma dynamics is the electric field, resulting from a potential difference between the electrodes. For this, Gauss's law for electrostatics applies, combined with the definition of the electric field. For the particle dynamics, specie continuity and momentum equations are applicable. These relations have been derived from the Boltzmann equation, as shown in the next session. Finally, an applicable form of Gauss's law is obtained.

The fundamental Boltzmann equation

The Boltzmann equation was formulated by Ludwig Boltzmann in 1872 and describes the distribution of particles in six phase dimensions $(\mathbf{r}, \mathbf{v})$; three dimensions in both space and velocity. In primitive form, the equation is written as:

$$f(\mathbf{r}, \mathbf{v}, t)\mathrm{d}^3\mathbf{r}\mathrm{d}^3\mathbf{v} = N, \tag{3.1}$$

Where N is the total number of particles in a spatial and velocity space. The final Boltzmann differential equation in three dimensional space is written by Lieberman and A. J. (1994) as:

$$\frac{\partial f}{\partial t} + \mathbf{v} \cdot \nabla_r f + \mathbf{a} \cdot \nabla_v f = \left.\frac{\partial f}{\partial t}\right|_c . \tag{3.2}$$

Here, f is the particle distribution function, $\nabla_r = (\hat{x}\partial/\partial x + \hat{y}\partial/\partial y + \hat{z}\partial/\partial z)$ and $\nabla_v = (\hat{x}\partial/\partial v_x + \hat{y}\partial/\partial v_y + \hat{z}\partial/\partial v_z)$, v is the three dimensional velocity vector and $\mathbf{a}$ is the three dimensional acceleration vector, which can also be written as $\mathbf{a} = \mathbf{F}/m$ according to Newton's second law. The term on the right hand side accounts for production or destruction of particles inside the control volume by chemical reactions, and is also known as the collision term. When zero, the Boltzmann equation becomes the *collisionless Boltzmann equation* (Lieberman and A. J. (1994)). Note that this equation solves for the distribution function $f(\mathbf{r}, \mathbf{v}, t)$ for a certain species. From this distribution, the following *average quantities* can be computed:

$$n(\mathbf{r},t) = \int f \mathrm{d}^3 v, \text{ the particle density,} \tag{3.3}$$

$$\Gamma(r,t) = n\mathbf{u} = \int v f \mathrm{d}^3 v, \text{ the particle flux,} \tag{3.4}$$

$$w = \frac{3}{2}p + \frac{1}{2}m\mathbf{u}^2 n = \frac{1}{2}m \int v^2 f \mathrm{d}^3 v, \text{ the particle volumetric kinetic energy.} \tag{3.5}$$

Here, $\mathbf{u}$ is the mean particle velocity and $p(\mathbf{r},t)$ the isotropic pressure while m represents the particle mass. v is the particle individual velocity. Using these definitions, the Boltzmann equation can manipulated into continuity, momentum and energy conservation. These are called the drift-diffusion equations as explained in the next subsection.

Derivation of the drift-diffusion equations

The drift-diffusion equations resemble a continuity, momentum and energy conservation equation. The first is obtained by integrating the Boltzmann equation over the velocity space, which yields Lieberman and A. J. (1994):

$$\frac{\partial n}{\partial t} + \nabla \cdot (n\mathbf{u}) = G - L \tag{3.6}$$

The right hand side consists of the respective gain (G) and loss (L) terms due to e.g. ionization and recombination. An additional equation is required to describe the particle population evolution as both n and $\mathbf{u}$ are unknown. By multiplying the Boltzmann equation by $\mathbf{v}$ and again integrating over the velocity, the following momentum equation is found:

$$mn\big[\frac{\partial \mathbf{u}}{\partial t} + (\mathbf{u} \cdot \nabla)\mathbf{u}\big] = qn(E + \mathbf{u} \times \mathbf{B}) - \nabla \cdot \Pi + \mathbf{f}\Big|_c . \tag{3.7}$$

Π is the pressure tensor, which arises from integration over velocities:

$$\Pi_{ij} = mn\langle (v_i - u)(v_j - u) \rangle \tag{3.8}$$

The last term on the right hand side of Equation 3.7 can be approximated by Krook's collision operator:

$$\mathbf{f}\Big|_c = -\sum_{\beta} mn v_{m\beta}(\mathbf{u} - \mathbf{u}_\beta) - m(\mathbf{u} - \mathbf{u}_G)G + m(\mathbf{u} - \mathbf{u}_L)L. \tag{3.9}$$

The parameters q, E and $\mathbf{B}$ represent the particle charge, the electric field vector and the magnetic field vector, respectively. The collision term involves momentum created by difference between the gross mean velocity and the velocities of the considered species $\mathbf{u}_\beta$, the newly gained particles $\mathbf{u}_G$ and the newly lossed particles $\mathbf{u}_L$. This term depends on the collisional cross section of the species, which determine the reaction rates, and thus the momentum loss or gain. According to Lieberman and A. J. (1994), generally $\mathbf{u}_L \approx \mathbf{u}$ and $|\mathbf{u}_G| \ll |\mathbf{u}|$. Applying there assumptions together with negligible magnetic effects and a single neutral species, the following momentum equation is obtained:

$$mn\big[\frac{\partial \mathbf{u}}{\partial t} + (\mathbf{u} \cdot \nabla)\mathbf{u}\big] = qnE - \nabla p - mnv_m\mathbf{u}. \tag{3.10}$$

The charge of the particle is represented by q. The pressure gradient term originates from the earlier denoted Π term and can be rewritten using the equation of state:

$$p = nkT \Rightarrow \nabla p = \nabla(k_B T n). \tag{3.11}$$

According to Goekce (2014), Equation 3.10 allows for a redefinition of the flux term described above:

$$\Gamma(\mathbf{r}, t) = n\mathbf{u}. \tag{3.12}$$

When taking electron as current species, Equation 3.10 can be written as:

$$m_e n_e(\frac{\partial v_e}{\partial t} + v_e \cdot \nabla v_e) = -en_eE - \nabla(k_B T_e n_e) - m_e n_e v_m v_e. \tag{3.13}$$

Assuming that the total derivative of the electron drift velocity, and therefore the LHS term, to be zero, which according to Jayaraman and Shyy (2008) is the case when the thermal velocity is comparable to the drift velocity ($v_e \leq v_t$) and the continuum regime can be assumed ($Kn = \lambda/L \ll 1$), the term for Γ_e can be rewritten into:

$$\Gamma_e = n_e v_e = \frac{-en_eE}{m_e v_m} - \frac{1}{m_e v_m}\nabla(k_B T_e n_e). \tag{3.14}$$

Please note that for positive ions have a charge of $+e$, where negative ions and electrons have a charge of $-e$. By assuming a constant species temperature, this relation can be more generalized in terms of mobility and diffusion coefficients μ_k and D_k, respectively, through which ultimately the species momentum equation is obtained, where k is the described species:

$$\Gamma_k = n_k v_k = \pm\mu_k E n_k - D_k \nabla(n_k), \tag{3.15}$$

Where $\mu_k = q_k/m_k v_m$ and $D_k = k_B T_k/m_k v_m$, with T_k in Kelvin, m_k is the species particle mass and v_m is the particle mean velocity. The diffusion coefficient can also be written in terms of the mobility coefficient: $D_k = \mu_k k_B T_k/q_k = \mu_k T_k^*$. T^* is the species temperature in eV. A Péclet number can now be obtained:

$$\text{Pe} = \frac{\mu_k |E| n_k}{D_k \nabla n_k} = \frac{|E| L}{T_k^*} = \frac{\phi_0}{T_k^*}. \tag{3.16}$$

The input voltage ϕ_0 is in the order of $\mathcal{O}(10^3)$, while typically for the electrons, $T_e^* = 1$ and for the heavy species, $T_i^* = \mathcal{O}(10^{-2})$, which means Pe $\geq 10^3$. This problem is therefore a convection dominated problem, and often the diffusion term is neglected. In this study though, diffusion is not neglected to increase fidelity of the model. Another motivation is numerical stability: the diffusion term acts as a spatial averaging term, which should help stabilize the convective scheme. In typical electric discharges, electrons can have typical velocities in the order of several 10^6m/s, while the heavy particles reach velocities up to 10^3m/s.

Generally, these coefficients are hard to obtain and are often approximated by a Boltzmann solver, e.g. as proposed by Hagelaar and Pitchford (2005). From their software *Bolsig+*, curve fit expressions can be obtained in which the mobility and diffusion coefficients are related to the reduced electric field E/N. More on this will be explained in section 4.4.

When the continuity source terms are expressed through collision rate coefficients, the following set of equations are obtained for three species (**e**lectron, **n**egative and **p**ositive ions) as discussed by Goekce (2014). Note that the physical model is presented for three species, while the actual number of species is dependent on the gas. Monatomic plasma (which requires a noble gas parent) for example only consists of positive ions and electrons.

Continunity equations:

$$\frac{\partial n_e}{\partial t} + \nabla \cdot \vec{\Gamma}_e = (\alpha - \eta)|\vec{\Gamma}_e| - n_e n_p \beta_{ei}, \tag{3.17}$$

$$\frac{\partial n_p}{\partial t} + \nabla \cdot \vec{\Gamma}_p = \alpha|\vec{\Gamma}_e| - n_e n_p \beta_{ei} - n_n n_p \beta_{ii}, \tag{3.18}$$

$$\frac{\partial n_n}{\partial t} + \nabla \cdot \vec{\Gamma}_n = \eta|\vec{\Gamma}_e| - n_n n_p \beta_{ii}, \tag{3.19}$$

Momentum equations:

$$\Gamma_e = -\,\mu_e \vec{E} n_e - D_e \nabla(n_e), \tag{3.20}$$

$$\Gamma_p = +\,\mu_p \vec{E} n_p - D_p \nabla(n_p), \tag{3.21}$$

$$\Gamma_n = -\,\mu_n \vec{E} n_n - D_n \nabla(n_n). \tag{3.22}$$

The coefficients α and η are the ionization and attachment coefficients, respectively, while the coefficients β_{ei} and β_{ii} are the recombination coefficients and account for electron-ion and ion-ion recombination, respectively. These coefficients determine the production and destruction rates of the species. The mobility coefficient μ_k and diffusion coefficient D_k relate to the transport of the particles. How these coefficients can be obtained is explained in section 4.4.

It is very common to present the governing equations in the drift-diffusion form above. From a fluid dynamic point of view though, it may be more interesting to write these equations in a slightly different form:

Continunity equations:

$$\frac{\partial n_e}{\partial t} + \nabla \cdot \vec{U}_e n_e - \nabla \cdot D_e \nabla(n_e) = (\alpha - \eta)|\vec{\Gamma}_e| - n_e n_p \beta_{ei}, \tag{3.23}$$

$$\frac{\partial n_p}{\partial t} + \nabla \cdot \vec{U}_p n_p - \nabla \cdot D_p \nabla(n_p) = \alpha|\vec{\Gamma}_e| - n_e n_p \beta_{ei} - n_n n_p \beta_{ii}, \tag{3.24}$$

$$\frac{\partial n_n}{\partial t} + \nabla \cdot \vec{U}_n n_n - \nabla \cdot D_n \nabla(n_n) = \eta|\vec{\Gamma}_e| - n_n n_p \beta_{ii}, \tag{3.25}$$

Velocities:

$$\vec{U}_e = -\,\mu_e \vec{E}, \tag{3.26}$$

$$\vec{U}_p = +\,\mu_p \vec{E}, \tag{3.27}$$

$$\vec{U}_n = -\,\mu_n \vec{E}, \tag{3.28}$$

Ionization collision flux:

$$|\vec{\Gamma}_e| = |\vec{U}_e n_e|. \tag{3.29}$$

In the ionization collision flux, only the drift velocity is considered, i.e. diffusion is assumed to yield insufficient energy to cause any reactions. This transforms the drift-diffusion equation in a more conventional convection-diffusion relation with source terms, which is a rather well-known problem in fluid dynamics. This also improves understanding in terms of the physical meaning of boundary conditions and choice of computational schemes, as the comparison to more conventional computational problems is easier to make. Also, OpenFoam® was developed for fluid dynamic problems, so the latter form will be more straight forward to implement.

Derivation of the Poisson equation for the electric potential

The electric field is the driving principle behind the creation of species and the discharge in general. The electric field is described by Gauss's law for electrostatics:

$$\nabla \cdot \varepsilon \vec{E} = \rho_c. \tag{3.30}$$

ε is the permittivity of the medium: $\varepsilon = \varepsilon_0 \varepsilon_r$. For example, the relative permittivity of air is 1.00059, while that of helium is 1.0000684. ρ_c is the space charge, in a plasma given by the sum of the free charge carriers:

$$\rho_c = q_p n_p + q_e n_e + q_n n_n = e(n_p - n_e - n_n). \tag{3.31}$$

Also introducing the electric potential $\vec{E} = -\nabla \phi$, the following differential equation is obtained:

$$\nabla \cdot \varepsilon \nabla \phi = -e(n_p - n_e - n_n). \tag{3.32}$$

This relation is valid in the fluid region where free space charges are available. In the solid regions of the dielectric and the electrodes, no such space charges are present, leaving the RHS zero. Also, as ε is constant throughout the dielectric domain:

$$\nabla \cdot \varepsilon \nabla \phi_d = 0 \Longrightarrow \nabla^2 \phi_d = 0. \tag{3.33}$$

A note on the energy equation

The drift-diffusion equations describe species number densities over time by means of a transport equation with source terms. The set consists of a continuity equation and a momentum equation per considered species. When the temperature of the species cannot be assumed to be constant, an energy equation is included as well. In this study though, it is assumed that the gain in electron energy is directly balanced by collisional losses, and no thermal energy is obtained. This leads to the Local Field Approximation (LFA), which states that the electron energy is solely dependent on the local reduced electric field strength E/N, as energy is not transported. This requires that the electron energy relaxation time scale is smaller than the characteristic discharge time scale, which is often the case in highly collisional plasmas (Arpa and D'Ambrosio (2009)).

A similar justification is given by Abdollahzadeh et al. (2016): two distinct species temperatures can be assumed, that of ions (positive and negative) and that of electrons, based on the particle masses, which is nearly identical for the positive and negative ions. Since the ions also have nearly the same mass as the neutral particles, it may be assumed that the ion temperature is of the same order as the neutral gas temperature, i.e. the ions are in thermal equilibrium with the neutral background gas. The electrons have such low mass that their temperature can be significantly higher than that of the ions, but are unlikely to change significantly. To simplify the problem, a high but constant electron temperature is then assumed, often of 1 eV ($\approx 11,600$K) as proposed by Jayaraman and Shyy (2008). Extension of the model by addition of an energy equation is left for future work.

3.3 Analytical boundary conditions

To solve the model problem with the equations given in the former section, boundary conditions must be formulated. The specie continuity equation includes a convection term and a diffusion term. The latter has an elliptic form, and requires specification of conditions for n_k on every boundary of the fluid domain.

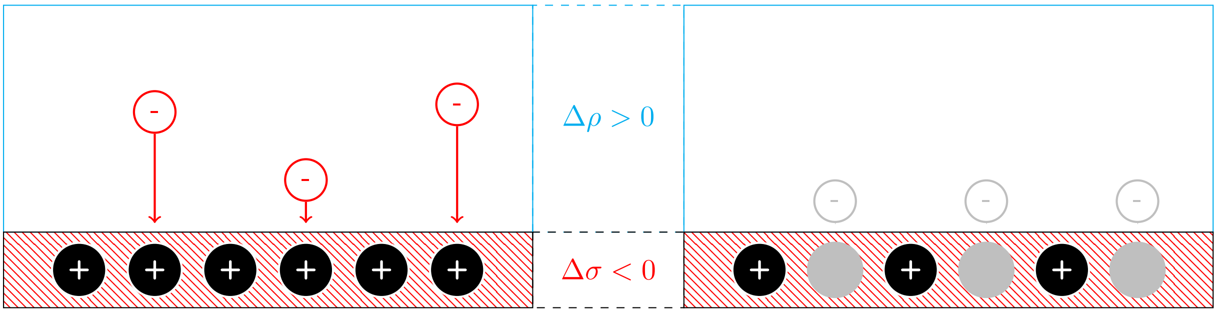

Figure 3.3: The concept of surface charging. While electrons collide on the dielectric surface, they attach to the positively polarized surface, reducing the net surface charge and increasing the net volume charge. The process is similar for ions.

The geometric problem is represented by the boundary conditions for the specie velocity $\vec{U}_k$, in literature often presented as conditions for the flux $\vec{\Gamma}_k$, and is quite typical for DBD. In general, any of the charged species colliding onto the geometric boundaries (electrode and dielectric surfaces in the fluid region) are assumed to recombine instantly. This is visualised in Figure 3.3 and can be explained as follows. Charged particles are highly reactive, as their non-zero net charge easily facilitates bonding with other particles. Charged electrodes have a net non-zero charge on their surfaces, while dielectrics have polarized surfaces. Although those charges are not free to move, they are exposed, and as the charged species in the plasma collide onto the surface, they react and form neutral molecules. This results in additional destruction of charge in the volume and charge storage on the surface: the charged species leave the plasma, and the charge on the electrode or dielectric surface is reduced. The charge surface density σ describes the net charge on the surfaces, and is dependent on the outflow of charged particles, i.e. the species fluxes.

This is discussed in the next subsection, where firstly conditions for the electrostatic potential ϕ are specified on all region boundaries.

Conditions for the electric potential

The electric potential is described by the elliptical Poisson equation, so no initial field values are required. The initial value of ρ_c is determined by the initial species densities and will be treated later. In Figure 3.4 and Figure 3.5 an overview of the electric potential boundary conditions is given.

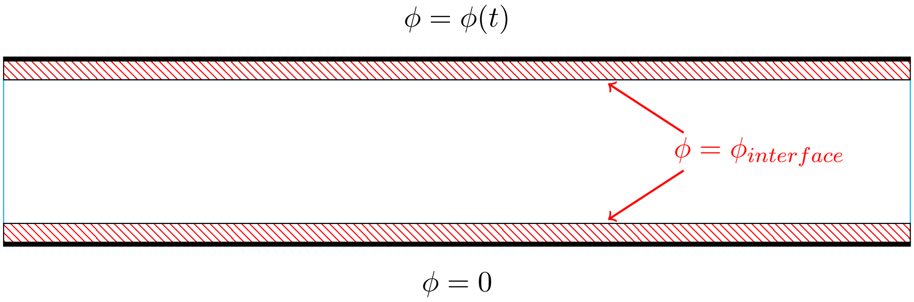

Figure 3.4: Analytical conditions for ϕ for the 1D geometry. The problem is defined in one dimension and needs no conditions on the left and right sides of the domain.

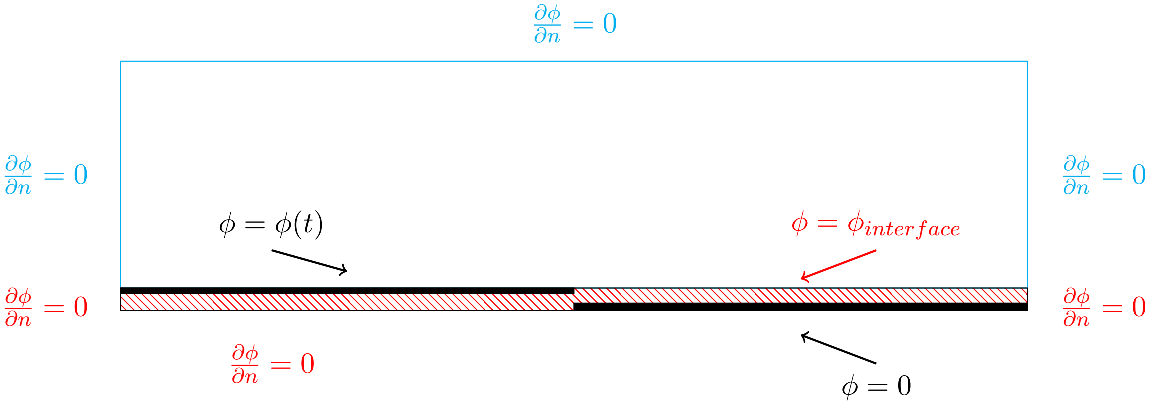

Figure 3.5: Analytical conditions for ϕ for the 2D geometry.

The values in the anode and cathode regions are prescribed as:

$$\phi_{anode} = \phi(t), \tag{3.34}$$

$$\phi_{cathode} = 0. \tag{3.35}$$

The outer domain boundary conditions of both the dielectric and the fluid regions are far field conditions, where the change of the electric potential is assumed to be zero:

$$\frac{\partial \phi}{\partial n} = 0. \tag{3.36}$$

The gas-dielectric region interface requires a special coupling condition. The Poisson equation is an elliptical equation which poses a boundary value problem. The value or the local normal derivative of ϕ should be known, which requires the solution in the other domain when solved in a segregated manner, which also is not known. This poses an initial-boundary value problem. This problem requires an iterative solution method for which a compatibility relation is required. On the boundary, the following conservation relation holds Abdollahzadeh et al. (2014):

$$\hat{n} \cdot (\varepsilon_0 \varepsilon_g E_{gas} - \varepsilon_0 \varepsilon_d E_{dielectric}) = \sigma. \tag{3.37}$$

Where σ is the accumulated charge surface density. This relation can be derived by considering Gauss's law:

$$\nabla \cdot \varepsilon \vec{E} = \rho_c, \tag{3.38}$$

which holds anywhere in the computational domain, and so also over a surface. Then, the relation can be written in a single dimension n, the distance normal to the surface. The component of the electric field in this direction is found by multiplication with the surface normal vector $\hat{n}$. Integrating with respect to n over a distance h then yields:

$$\int_h \left[\frac{\partial}{\partial n} \varepsilon \hat{n} \cdot \vec{E}\right] \mathrm{d}n = \int_h \rho \mathrm{d}n \Longrightarrow \Delta \varepsilon \hat{n} \cdot \vec{E} = \sigma. \tag{3.39}$$

This condition couples the electric fields in two domains connected by a surface on which the charge surface density is known. In literature, this relation is sometimes termed as the current continuity condition. The relation for σ is often bluntly given. For clarity, the relation between surface and volume charge is used to derive the equation for the charge surface density required in the coupling condition given above.

Derivation of the charge surface density

In the equation for the coupling value of the interface potential, a surface charge is taken into account. This surface charge causes a discontinuity in the electric field normal to the surface by accumulation of free space charge carriers in the fluid domain. To obtain this density, the relation between a volume and its area is considered first:

$$\begin{aligned}\frac{1}{\mathrm{d}V} = \frac{1}{\mathrm{d}A\mathrm{d}n} \Longrightarrow \mathrm{d}\rho_c &= \frac{q_c}{\mathrm{d}V} \\ &= \frac{q_c}{\mathrm{d}A\mathrm{d}n} = \frac{\mathrm{d}\sigma}{\mathrm{d}n} \Longrightarrow \iint_h \mathrm{d}\rho_c dn = \int \mathrm{d}\sigma.\end{aligned} \tag{3.40}$$

ρ_c is the charge (q_c) per unit volume (V), whereas σ is the charge per unit area (A) and h is the distance of the volume normal to the surface. In this case, the surface of interest is the dielectric surface, above which the charge volume density is known and can be written in terms of its fluxes:

$$\begin{aligned}\rho_c &= e(n_p - n_e - n_n) \\ &= \int_0^t e(\frac{\partial n_p}{\partial \tau} - \frac{\partial n_e}{\partial \tau} - \frac{\partial n_n}{\partial \tau})\mathrm{d}\tau \\ &= \int_0^t e(-\nabla \cdot \Gamma_p + \nabla \cdot \Gamma_e + \nabla \cdot \Gamma_n)\mathrm{d}\tau.\end{aligned} \tag{3.41}$$

This relation is obtained by noting that, when summing the different specie continuity equations, all source terms cancel out:

$$\begin{aligned}S_p - S_e - S_n &= \alpha|\vec{\Gamma}_e| - n_e n_p \beta_{ei} - n_n n_p \beta_{ii} \\ &\quad - (\alpha - \eta)|\vec{\Gamma}_e| + n_e n_p \beta_{ei} \\ &\quad - \eta|\vec{\Gamma}_e| + n_n n_p \beta_{ii} \\ &= \alpha|\vec{\Gamma}_e| - (\alpha - \eta)|\vec{\Gamma}_e| - \eta|\vec{\Gamma}_e| \\ &\quad - n_e n_p \beta_{ei} - n_n n_p \beta_{ii} + n_e n_p \beta_{ei} + n_n n_p \beta_{ii} \\ &= 0.\end{aligned} \tag{3.42}$$

Particles are always created or destroyed in combination with another specie, e.g. electrons with positive ions during ionization or positive and negative ions during recombination. What is left then are the flux terms. Since the control volume is constant over time, the differential operator is independent of time and can be taken out of the integral:

$$\rho_c = \nabla \cdot \int_0^t e(-\Gamma_p + \Gamma_e + \Gamma_n)\mathrm{d}\tau, \tag{3.43}$$

$$\sigma = \int_h \rho_c dn = \int_h \nabla dn \cdot \int_0^t e(-\Gamma_p + \Gamma_e + \Gamma_n)\mathrm{d}\tau. \tag{3.44}$$

Where it can be found that $\int_h \nabla \mathrm{d}n = -\hat{n}$, which is the surface normal vector **out of the domain** following OpenFoam® sign convention. Concluding, the relation for σ is given by:

$$\sigma = \hat{n} \cdot \int_0^t e(\Gamma_p - \Gamma_e - \Gamma_n)\mathrm{d}\tau. \tag{3.45}$$

In words, the charge surface density is the surface normal component of the species fluxes weighted by their charge integrated over time. Time t is the current time value, which increases with each iteration.

In some cases, better control on the physical processes on the surfaces can be achieved by using separate relations for the individual charge surface densities:

$$\frac{\partial \sigma_k}{\partial t} + \Gamma_k = s_k. \tag{3.46}$$

In which σ_k is the charge density on a surface of species k and s_k is a source term. The flux term is then composed out of transport and source terms, e.g. Golubovskii et al. (2002b):

$$\Gamma_k = e(u_k n_k - \gamma v_i n_i - \sigma_k \nu_k^{des}). \tag{3.47}$$

ν_k^{des} is the desorption frequency in s-1. The source term can consist of surface recombination term between species k and j:

$$s_k = \alpha_{re,kj} \sigma_k \sigma_j. \tag{3.48}$$

Finally, the net charge surface density is then given by:

$$\sigma = \sigma_p - \sigma_e - \sigma_n. \tag{3.49}$$

In this work, the **latter** formulation is **not** used, and the charge surface density is computed integrally using Equation 3.45 obeying the boundary conditions presented below.

Conditions for the species flux

The species number densities are only solved for in the fluid domain, so no boundary conditions are required in the other domains. The conditions for the flux define the geometric problem, and the prescribed conditions determine whether the boundary is e.g. a non-slip wall, an inlet or an outlet.

On the geometric surfaces, special care has to be taken. Charged particles are highly reactive, and are assumed to instantaneously recombine when colliding onto the surface. In the normal drift-diffusion formulation, conditions for the flux term Γ_k are specified. Conditions for this term used in literature will be presented first. Then, the conditions will be rewritten in terms of $\vec{U}_k$ to match Equation 3.23 to Equation 3.29.

The conventional boundary conditions applicable to the drift-diffusion equations have been discussed by Unfer and Boeuf (2010); Goekce (2014); Abdollahzadeh et al. (2016), which assume instantaneous recombination on the anode and dielectric surfaces. An overview of these conditions is given in Figure 3.6.

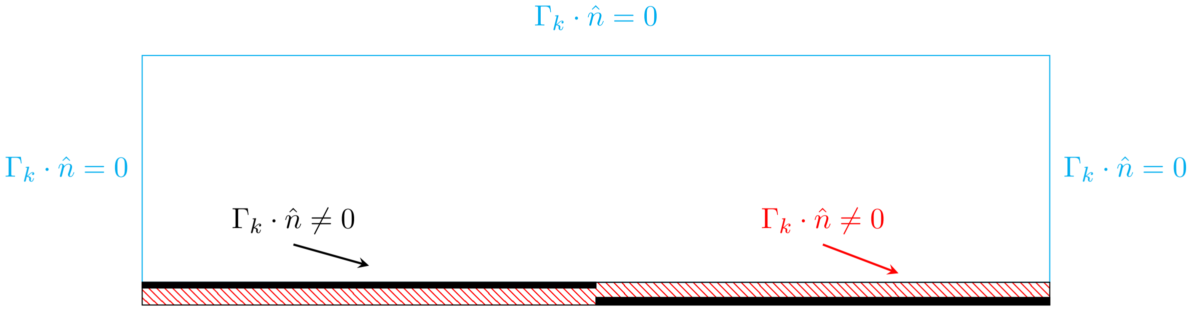

Figure 3.6: Overview of the species flux boundary conditions for the drift-diffusion formulation found in literature.

The flux values on the geometric surfaces are then given by the following relation for the ions:

$$\hat{n} \cdot \vec{\Gamma}_i = \frac{1}{4} v_{i,th} n_i + \max(\pm \mu_i \hat{n} \cdot \vec{E}, 0) n_i, \tag{3.50}$$

and for the electrons:

$$\hat{n} \cdot \vec{\Gamma}_e = \frac{1}{4} v_{e,th} n_e + \max(-\mu_e n_e \hat{n} \cdot \vec{E}, \gamma \mu_p n_p \hat{n} \cdot \vec{E}). \tag{3.51}$$

Here, the thermal velocity scalar is given by $v_{k,th} = \sqrt{8 k_B T_k / \pi m}$. Typical values of $v_{k,th}$ are in the order of $\mathcal{O}(10^5)$ for electrons (at 11,600K) and $\mathcal{O}(10^2)$ for ions (300K). The condition states that on the boundary faces of the domain, all $\pm\mu_k\hat{n}\cdot\vec{E}$ particles drifting towards the surface are permitted to leave the computational domain, which translates physically into instantaneous recombination. Additionally, the thermal velocity of each particle accounts for extra flux: i.e. when the drift velocity would be negligible, $\frac{1}{6}\frac{3}{2}v_{k,th}n_k$ particles close to the surface still collide with the surface, thereby combining, purely because of the thermal motion of said particles. Considering the electrons, an extra term is added to account for secondary electron emissions: $\Gamma_{e,sec} = -\gamma\Gamma_p$. This term is added to the relation in Equation 3.51 and is only non-zero if the positive ion flux is positive. In that case, the electron drift is always negative, and then according to Equation 3.50 set to zero. In the case of ns-DBD, the thermal velocity may be assumed negligible compared to the drift velocity.

Hagelaar et al. (2000) evaluates the condition in Equation 3.50 from a physical perspective, and concludes that the diffusion term $D\nabla n$ is often wrongly ignored. The derivations of the following equations are well explained in his work, so only a recapitulation is given. When this diffusion term is taken into account, the following relation is obtained:

$$\hat{n}\cdot\vec{\Gamma}_i = \frac{1}{2}v_{th}n_i + (2a_i - 1)\pm\mu_i\hat{n}\cdot\vec{E}n_i. \tag{3.52}$$

Where $a_i = 1$ for $\pm\mu_i\hat{n}\cdot\vec{E} > 0$, and $a_i = 0$ if $\pm\mu_i\hat{n}\cdot\vec{E} < 0$. The term $\pm\mu_i\hat{n}\cdot\vec{E}$ is the drift velocity, so this term can be rewritten into a similar form of Equation 3.50 as:

$$\hat{n}\cdot\vec{\Gamma}_i = \frac{1}{2}v_{i,th}n_i + 2\max(\pm\mu_i\hat{n}\cdot\vec{E},0)n_i - (\pm\mu_i\hat{n}\cdot\vec{E})n_i. \tag{3.53}$$

Additionally, the secondary electrons are also debated in Hagelaar et al. (2000), most notably the fact that in Equation 3.50 the plasma bulk electrons and the ones emitted from the dielectric surface are treated equally, while this mistakenly assumes that the secondary electrons also contribute to the wall-directed diffusion flux. The two types are thus separated into α bulk electrons and γ secondary electrons. For the α electrons, the expression in Equation 3.53 holds. For the γ electrons, the following relation was found:

$$\hat{n}\cdot\vec{\Gamma}_\gamma = -(1-a_e)\gamma\hat{n}\cdot\Gamma_p. \tag{3.54}$$

The last term is the original secondary electron flux term. If $a_e = 1$, the electron velocity is directed towards the surface, which means any species of opposite sign (positive ions), is not. No secondary electron emission occurs, and the term becomes zero. The γ electron number density n_γ is given by the relation:

$$n_\gamma \approx (1-a_e)\frac{\mu_p}{\mu_e}n_p\gamma\Big[(2a_p-1)+\frac{1}{2}\sqrt{\frac{8(m_p+m_g)m_g}{\pi(5m_p+3m_g)m_p}}\Big]. \tag{3.55}$$

The values of the positive ion mass m_p and neutral gas mass m_g depend on the incorporated species. When the electron flux terms are combined in rewritten in the form presented first, the following relation is obtained the electron geometric surface boundary condition:

$$\hat{n}\cdot\vec{\Gamma}_e = \frac{1}{2}v_{e,th}(n_e - n_\gamma) + 2\max(\pm\mu_e\hat{n}\cdot\vec{E},0)n_e - (\pm\mu_e\hat{n}\cdot\vec{E},0)n_e - 2\max(\gamma\hat{n}\cdot\Gamma_p,0). \quad (3.56)$$

What is obtained then is the original flux term with a correction to the thermal flux equal to the number of secondarily emitted electrons.

It is added to this discussion that the work of Hagelaar et al. (2000) was published before the other papers (e.g. (Unfer and Boeuf, 2010; Goekce, 2014; Abdollahzadeh et al., 2016)) referred to here. Even after publication, the condition in Equation 3.50 has been widely used, most likely to allow for comparison with earlier work. Therefore, it is difficult to draw conclusions on how this improved boundary condition in Equation 3.53 performs compared to the more widely applied condition in Equation 3.50, although it is shown by Hagelaar et al. (2000) that the first yields a higher effective secondary electron emission coefficient as compared to the corrected formulation. For a γ of 0.2, this can be 20% higher, potentially leading to unrealistically high emission of electrons.

The conditions for the convection-diffusion formulation are found by considering that $\vec{\Gamma}_k = \vec{U}_k n_k$. This gives the following conditions:

Boeuf et al. (2009)

$$\hat{n}\cdot\vec{U}_i = \frac{1}{4}v_{th} + \max(\pm\mu_i\hat{n}\cdot\vec{E},0), \quad (3.57)$$

$$\hat{n}\cdot\vec{U}_e = \frac{1}{4}v_{th} + \max(-\mu_e\hat{n}\cdot\vec{E},\mu_p\frac{n_p}{n_e}\hat{n}\cdot\vec{E}). \quad (3.58)$$

Hagelaar et al. (2000)

$$\hat{n}\cdot\vec{U}_i = \frac{1}{2}v_{th} + 2\max(\pm\mu_i\hat{n}\cdot\vec{E},0) - (\pm\mu_i\hat{n}\cdot\vec{E}), \quad (3.59)$$

$$\hat{n}\cdot\vec{U}_e = \frac{1}{2}v_{th}(1-\frac{n_\gamma}{n_e}) + 2\max(\pm\mu_e\hat{n}\cdot\vec{E},0)n_e - (\pm\mu_e\hat{n}\cdot\vec{E},0)n_e - 2\max(\gamma\frac{n_p}{n_e}\hat{n}\cdot\vec{U}_p,0). \quad (3.60)$$

With the definition of n_γ give in Equation 3.55 and:

$$v_{k,th} = \sqrt{\frac{8eT_k}{\pi m_k}}. \quad (3.61)$$

The conditions presented are implemented and in chapter 5 compared to one another.

Conditions for the species number densities

As the densities are described by unsteady transport equations, the problem is classified as an initial-value problem. The initial value is a manner of modelling photo-ionization, a complex process not further treated in this work but essential in streamer modelling. According to Pancheshnyi (2005), this effect can be incorporated by assuming an initial uniform neutral plasma at the start of the simulation. It is even added that other photo-ionization models only yield unrealistic results.

The values of the densities of the positive and initial species should be equal to assure a neutral plasma. The initial conditions of the three species are then:

$$\begin{aligned} n_e^0 = n_0, \qquad n_p^0 &= n_0, \\ n_n^0 &= 0. \end{aligned} \tag{3.62}$$

The value of n_0 can be varied to investigate the influence of the initially available space charges on the discharge characteristics. Typically, these values range from 10^{12} to 10^{16}, in contrast to a neutral particle density in the order of 10^{25} at atmospheric conditions.

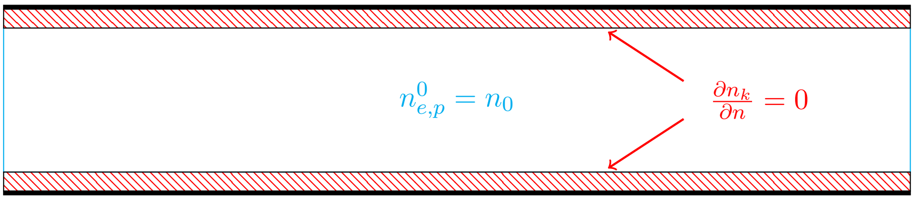

Figure 3.7: Analytical conditions for n_k for the 1D geometry. The problem is defined in one dimension and needs no conditions on the left and right sides of the domain.

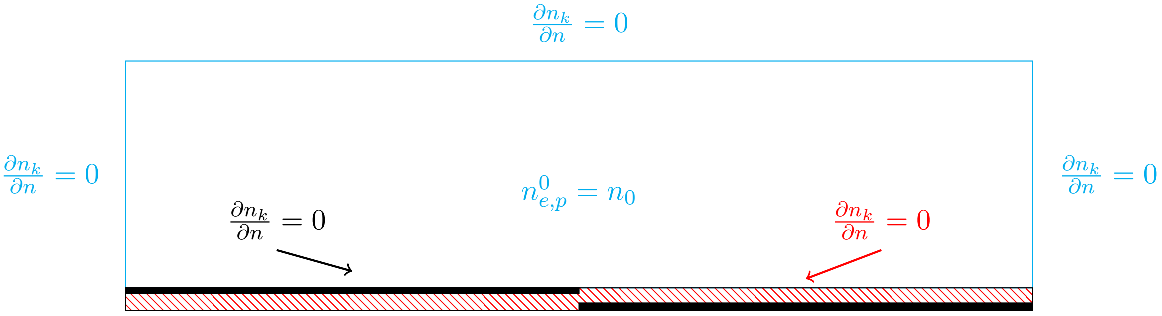

Figure 3.8: Analytical conditions for n_k for the 2D geometry.

The boundary conditions for species densities on the surfaces relate to the diffusion term. As was discussed in the former subsection, the diffusion term is included in the velocity term, and the original diffusion term is zero. The conditions on all boundaries, both far field and surface geometry, prescribe zero gradient conditions for all species, as shown in Figure 3.7 and Figure 3.8:

$$\frac{\partial n_k}{\partial n} = 0. \tag{3.63}$$

3.4 Plasma-neutral flow coupling source terms

The plasma induced flow interaction is due to ion-neutral particle momentum transfer and energy deposition as explained in section 2.6 and section 2.7. The body force consists of a Coulomb force and a pressure force:

$$\vec{F}_{EHD} = e(n_p - n_e - n_n)\vec{E} - \sum_{k=e,n,p} \nabla k_b T_k n_k \tag{3.64}$$

The first term is the momentum transfer by charged particle drift driven by the electric field. The second term stems from the partial pressure term, found by applying the equation of state:

$$p_k = k_b T_k n_k. \tag{3.65}$$

In general, the Coulomb force (drift term) accounts for the larger order (Goekce (2014)) which may lead to neglect of the diffusion term when only the order of magnitude of the force is of interest.

The heating term is built-up from two energy deposition processes. The first is ion-neutral molecule collisions, generally known as Joule or resistive heating found in any situation of an electric current through a medium with significant resistance. It's value is given by:

$$p_{ions} = (\vec{J}_p - \vec{J}_n) \cdot \vec{E}. \tag{3.66}$$

This relation describes the energy transferred from the electric field to the neutral gas through the induced ion current, indicated by $\vec{J}_p$ and $\vec{J}_n$, which are found by:

$$\vec{J}_k = q_k \vec{U}_k n_k. \tag{3.67}$$

Subscript $k = p, n$, q_k is the charge of the species, $\vec{U}_k n_k$ is the species density flux. The second contribution is due to thermal energy transfer from electrons to neutral particles, driven by elastic and rotational excitation (subscript el-R), vibrational and translation relaxation (subscript VT) and electronic excitation (subscript E):

$$\begin{aligned} p_{th,e} &= p_{el-R} + p_{VT} + p_E && (3.68) \\ &= (\eta_{el-R} + \xi \eta_E)\sigma_e |E|^2 + p_{VT}. && (3.69) \end{aligned}$$

In this equation, ξ represents the electron excitation energy instantaneously deposited into gas heating and is assumed to have a value of 30% and σ_e is the electrical conductivity of the medium, given by the equation below:

$$\sigma_e = e\mu_e n_e. \tag{3.70}$$

It denotes the ease of charged particle motion through the medium. The value of μ_e represents electron mobility inside the plasma. p_{VT} is found by solving a phenomenological differential equation:

$$\frac{\partial p_{VT}}{\partial t} + \frac{1}{\tau_{VT}} p_{VT} = \frac{1}{\tau_{VT}} \eta_V \sigma_e |E|^2. \tag{3.71}$$

Since the right hand side and the initial conditions are known, p_{VT} can be marched forward in time. The relation depends on an assumed characteristic residence time τ_{VT}, which is the time the plasma resides in the flow (and therefore the time the plasma has to deposit its energy).

3.5 Summary of the physical model

Governing equations

Gauss's law:

$$\begin{aligned} \nabla^2\phi &= 0 && \text{in solid regions,} \\ \nabla\cdot\varepsilon\nabla\phi &= -e(n_p - n_e - n_n) = -\rho_c && \text{in fluid regions.} \end{aligned} \tag{3.72}$$

Definition of the electric field vector:

$$\vec{E} = -\nabla\phi. \tag{3.73}$$

Electric field compatibility relation:

$$\hat{n}\cdot(\varepsilon_0\varepsilon_g E_{gas} - \varepsilon_0\varepsilon_d E_{dielectric}) = \sigma. \tag{3.74}$$

Charge surface density:

$$\frac{\partial\sigma}{\partial t} = \hat{n}\cdot e(\vec{U}_p - \vec{U}_e - \vec{U}_n) \qquad \text{only fluid regions.} \tag{3.75}$$

Continunity equations:

$$\begin{aligned} \frac{\partial n_e}{\partial t} + \nabla\cdot\vec{U}_e n_e - \nabla\cdot D_e\nabla(n_e) &= (\alpha-\eta)|\vec{\Gamma}_e| - n_e n_p\beta_{ei}, \\ \frac{\partial n_p}{\partial t} + \nabla\cdot\vec{U}_p n_p - \nabla\cdot D_p\nabla(n_p) &= \alpha|\vec{\Gamma}_e| - n_e n_p\beta_{ei} - n_n n_p\beta_{ii}, \\ \frac{\partial n_n}{\partial t} + \nabla\cdot\vec{U}_n n_n - \nabla\cdot D_n\nabla(n_n) &= \eta|\vec{\Gamma}_e| - n_n n_p\beta_{ii}. \end{aligned} \tag{3.76}$$

Species velocities:

$$\begin{aligned} \vec{U}_e &= -\mu_e\vec{E}, \\ \vec{U}_p &= +\mu_p\vec{E}, \\ \vec{U}_n &= -\mu_n\vec{E}. \end{aligned} \tag{3.77}$$

Ionization collision flux:

$$|\vec{\Gamma}_e| = |\vec{U}_e n_e|. \tag{3.78}$$

Conduction current:

$$\vec{J} = e(\vec{U}_p n_p - \vec{U}_e n_e - \vec{U}_n n_n). \tag{3.79}$$

Mobility and reaction rate coefficients:

$$\begin{aligned} & & \alpha = f(\vec{E}), \qquad & \eta = f(\vec{E}), \\ \mu_e = f(\vec{E}), \qquad & & \mu_p = f(\vec{E}), \qquad & \mu_n = f(\vec{E}), \\ D_e = f(\vec{E}), \qquad & & D_p = f(\vec{E}), \qquad & D_n = f(\vec{E}). \end{aligned} \tag{3.80}$$

Initial conditions (fluid regions)

Species densities:

$$\begin{aligned} n_e^0 &= n_0, \\ n_p^0 &= n_0, \\ n_n^0 &= 0. \end{aligned} \tag{3.81}$$

Charge surface density:

$$\sigma^0 = 0. \tag{3.82}$$

Boundary conditions

Far field:

$$\frac{\partial \phi}{\partial n} = 0, \tag{3.83}$$

$$\frac{\partial n_k}{\partial n} = 0. \tag{3.84}$$

$$\hat{n} \cdot U_k = 0. \tag{3.85}$$

Electrodes:

$$\phi_{anode} = \phi(t), \tag{3.86}$$

$$\phi_{cathode} = 0. \tag{3.87}$$

Fluid-dielectric interfaces (solid regions):

$$\phi = \phi_{interface}. \tag{3.88}$$

Fluid-dielectric interfaces (fluid regions):

$$\frac{\partial n_k}{\partial n} = 0, \tag{3.89}$$

$$\phi = \phi_{interface}. \tag{3.90}$$

Boeuf et al. (2009)

$$\begin{aligned} \hat{n} \cdot \vec{U}_i &= \frac{1}{4} v_{th} + \max(\pm \mu_i \hat{n} \cdot \vec{E}, 0), \\ \hat{n} \cdot \vec{U}_e &= \frac{1}{4} v_{th} + \max(-\mu_e \hat{n} \cdot \vec{E}, \mu_i \frac{n_p}{n_e} \hat{n} \cdot \vec{E}). \end{aligned} \tag{3.91}$$

Hagelaar et al. (2000)

$$\begin{aligned} \hat{n} \cdot \vec{U}_i &= \frac{1}{2} v_{th} + 2\max(\pm \mu_i \hat{n} \cdot \vec{E}, 0) - (\pm \mu_i \hat{n} \cdot \vec{E}), \\ \hat{n} \cdot \vec{U}_e &= \frac{1}{2} v_{th} (1 - \frac{n_\gamma}{n_e}) + 2\max(\pm \mu_i \hat{n} \cdot \vec{E}, 0) n_e \\ &\quad - (\pm \mu_i \hat{n} \cdot \vec{E}, 0) n_e - 2\max(\gamma \frac{n_i}{n_e} \hat{n} \cdot \vec{U}_p, 0). \end{aligned} \tag{3.92}$$

Chapter 4

Description of the numerical model

In this chapter, the physical model presented in the former chapter is converted into a numerical model. The governing equations are discretized, the boundary conditions are implemented and a numerical approach is designed, leading to a specific solver architecture.

In section 4.1, an introduction to the the open source CFD software OpenFoam® is given. The coordinate system and cell convention are explained, as well as the solution methods on which this software is based. Finally, the discretization schemes utilized in this work are presented.

This chapter continues in section 4.2 and section 4.3 with the formulations of the governing equations. Both the Poisson equation for electrostatics and the species continuity equations need special care. In order to overcome the most restrictive time scales (see Table 2.1), semi-implicit formulations are derived. Implementation, specifically in OpenFoam® , of these equations is treated briefly as well.

In section 4.4, the chemical model is introduced, which finds its way into the model through the reaction rate coefficients. A numerical model for finding the reaction rate and mobility coefficients is presented, followed by the simulation results for two gases: helium and air. These results are used in the numerical solver to model the chemical reactions of the non-equilibrium plasma.

Discretization and implementation of the boundary conditions proposed in section 3.3 are elaborated on in section 4.5. Conditions for the electric potential, number densities and fluxes are all shown how they have been implemented using short code snippets.

Finally in section 4.6, the numerical procedure and solver architecture is explained. Also, a time chart is included in which advancement of each variable is depicted.

4.1 Finite volume discretization in **OpenFoam**®

To transform the physical model into a mathematical model, consisting of a set of equations which can be solved, the solution domain must be discretized. The finite volume discretization divides the control volume into an N number of sub-control volumes, each cell having a centre point and a number of faces, corresponding to the number of neighbour cells of the cell. The sign convention used in OpenFOAM is displayed in Figure 4.1 Jasak (1996). This is a cell of arbitrary shape; in this work only equidistant hexahedral meshes are employed. In plasma modelling, cell sizes in the order of μm is typical.

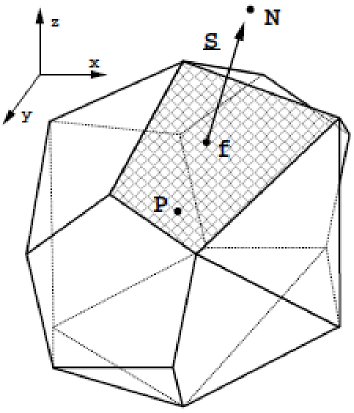

Figure 4.1: Arbitrarily shaped single cell with sign properties used in OpenFOAM finite volume discretization Jasak (1996).

Geometric field description

Two types of faces exist: the internal faces and the boundary faces. Internal faces are always shared between exactly two cells and therefore have an owner cell and a neighbour cell. The owner cell is always the cell with the lower index. Boundary faces are all other faces which together form the boundaries of the computational domain. Such domain boundaries are called patches each and consist of a set of boundary faces which make up the domain boundaries. The most important patches are:

- Wall patches for physical wall representation;
- Empty patches for reduced dimension representation of the computational domain (2D or 1D);
- Coupling patches for coupled boundaries in multi-region problems;
- Internal patches for parallel computation communication.

Volume and surface fields exist, both either as scalar fields or vector fields. Vectors interpolated to the faces can be scaled to a face normal scalar by inner-multiplication with the face normal vector. A face has a normal component which is defined positive in the cell outward direction. A positive flux on a face is then also pointing outward. This implies that at the boundaries, the positive normal is always directed out of the domain. Inside the volumes, the Cartesian coordinate system is used, i.e. a vector x-component is defined positive in the positive x direction.

Cell centre values are defined in the internalField array, while the values on the boundary surfaces are defined in the boundaryField array. The distinction between the two is visualized in Figure 4.2.

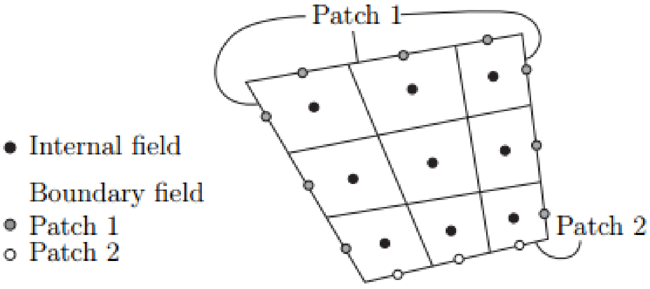

(a) A volField<Type>

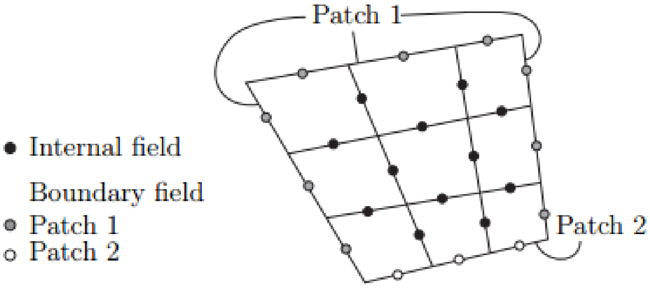

(b) A surfaceField<Type>

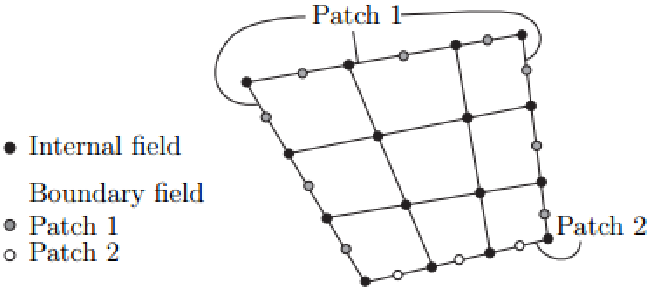

(c) A pointField<Type>

Figure 4.2: Field definitions in OpenFoam® . Volume fields are defined in the cell centres, while surface fields are defined on the cell interfaces (called faces). Boundary fields of any type are defined on the faces forming the outer boundary of the computational domain. Each boundary face belongs to a certain patch, which can be assigned a certain type with corresponding properties (documentation under reference Greenshields).

When a set of equations is solved, the internal field of the variable is accessed. The boundary values are user set and define the physical problem.

Solution methods

OpenFoam® uses iterative methods to solve PDEs. This means that always a matrix formulation of the corresponding problem is required:

$$A\bar{x} = \bar{b}$$

This approach is called implicitly solving of a PDE: the first step contains setting up the coefficient matrix A, while the second step consists of solving for $\bar{x}$ using one of the many available methods. Methods used in this work are the Preconditioned Conjugate Gradient (PCG) method and a multi-grid method, called the geometric-algebraic multi-grid (GAMG) method. Explicit relations don't need an iterative method and simply are solved using a diagonal solver. When setting up the governing equations in the source code, the user can define the level of implicitness. A typical example is the incompressible, inviscid, homogeneous momentum equation of the Navier-Stokes equations.

$$\frac{\partial \vec{u}}{\partial t} + \nabla \cdot (\phi \vec{u}) = -\nabla p$$

In this equation $\vec{u}$ is the velocity, ϕ is the mass flux $\rho\vec{u}$ and p is the pressure. The divergence term can now be included explicitly or implicitly. For the first, the divergence of the product $\phi\vec{u}$ is evaluated at the current time step and the explicit values of the term are added to the source term $\bar{b}$ on the RHS. The coefficient matrix will then consist of the matrix T only:

$$T\vec{u} + \bar{s} = \bar{b} \Longrightarrow \vec{u} = T^{-1}(\bar{b} - \bar{s})$$

The current example assumes a direct solution method for simplicity; this is not available in OpenFoam® . When treated implicitly, the divergence term is instead written into a matrix form as well:

$$T\vec{u} + U\vec{u} = \bar{b} \Longrightarrow \vec{u} = (T + U)^{-1}\bar{b} \tag{4.1}$$

It can be seen that the latter form contributes to higher accuracy of the solution, as the convection term contributes to the coefficient matrix, instead of contributing to the source term with a lagged value.

If all governing equations are assembled into one system of equations, the problem is said to be solved fully implicitly. This method does not require any iterative processes, but is often very difficult to implement. If the equations are solved separately, but the individual equations are solved implicitly, the problem is said to be solved semi-implicitly. With the set of equations governing the problem in this work, fully implicit implementation is very tricky. Furthermore, OpenFoam® is not optimized for fully implicit implementation. The equations will be implemented in a semi-implicit way: each relation is formulated implicitly, but the individual equations are solved in a sequence. This requires an iterative process to make the system of equations converge. More insight in the numerical procedure is given in section 4.6.

In sections section 4.2, the semi-implicit formulations of the governing equations of the plasma modelling are presented.

Discretization schemes in OpenFoam®

Many discretization schemes have already been implemented in OpenFoam® , ranging from first order temporal schemes to higher order Total Variation Diminishing (TVD) spatial schemes. A complete overview of schemes can be found on the OpenFoam® website [1]. Here the most relevant schemes are presented: the forward Euler scheme and the TVD MUSCL scheme.

The forward Euler temporal scheme is a first order implicit scheme, and uses the following discretization (implicit, first order):

$$\frac{\partial \phi}{\partial t} = \frac{\phi - \phi^0}{\Delta t}. \tag{4.2}$$

A first order scheme is usually not preferred in a transient solver. The problem of first order schemes is the linear decrease of the truncation error with the time step. Say, a simulation is run with N number of time steps, the cumulative discretization error is:

$$\epsilon_{disc,N} = \sum_{N} \epsilon_i. \tag{4.3}$$

Now, when the number of time steps is doubled, i.e. $M = 2N$, the truncation error per step is decreased by a factor two:

$$\epsilon_{disc,M} = \sum_{M} \epsilon_j = 2 \sum_{N} \frac{1}{2} \epsilon_i = \epsilon_{disc,N}. \tag{4.4}$$

---

[1] http://www.openfoam.com/documentation/user-guide/ (May 24, 2017)

Concluding, the total error of the simulation is not reduced. The scheme is still chosen though because sub-cycling is required at a later stage to solve the non-homogeneous continuity equations, as will be explained in section 4.6. Higher order methods, such as the backward Euler scheme, requires special asynchronous time stepping implementation (Unfer (2008)) which is not treated here, but recommended for future work. The scheme has been tested for code verification of the homogeneous continuity equations though. It's discretization (implicit, second order) is given by:

$$\frac{\partial \phi}{\partial t} = \frac{1}{\Delta t}(\frac{3}{2}\phi - 2\phi^0 + \frac{1}{2}\phi^{00}). \tag{4.5}$$

For spatial discretization, a total variation diminishing (TVD) MUSCL interpolation scheme is used. The finite volume method in OpenFoam® uses Gaussian integration for evaluation of spatial derivatives. In practice, this means the flux values on the interfaces of a cell are summed over. This flux term is defined on the cell interfaces, while the species densities are defined in the cell centres. An interpolation scheme is required to find the flux $\vec{U}_k n_k$ on the cell interfaces. The MUSCL scheme is a TVD scheme, based on Godunov's scheme, where instead of using piecewise constant values in each cell, linearly varying distributions are obtained. This is called reconstruction and according to Harten (1983), by limiting the reconstructed function, monotonicity can be assured: spurious artificial oscillations are prevented by limiting the flux on a cell interface according to the surrounding fluxes. This is done by choosing a specific limiter function, which is a min-mod limiter standard for MUSCL. Other limiters, such as de Van Leer and SuperBee limiters are available as well, but have not been used in this work. More insight in the MUSCL scheme implementation is given in Appendix B. Here, other discretization schemes proposed in literature can be found as well.

The model problem in this work is dominated by species convection, for which a flux limited higher order scheme is an appropriate choice. Such schemes are also often used in modelling of flow discontinuities and have proven their worth.

In this work, only the MUSCL scheme is utilized, combined with either a forward or backward Euler scheme. The MUSCL scheme formally is second order in smooth regions, and first order near discontinuities. The forward and backward Euler are first and second order in time, respectively. In the convection-diffusion problem with both spatial and temporal variations, the truncation error of the highest magnitude always dominates, which is not necessarily term with the lowest order as the spatial en temporal resolution are limited by one another through the Courant number.

4.2 Semi-implicit formulations of the Poisson equation

Explicit integration of differential equations lead to strict restrictions in temporal and spatial resolution if stability is still to be assured. The most severe time step restriction is the dielectric relaxation time, which relates to the evolution of the electric field, found through the Poisson equation. This equation is dependent on species densities at the current time step, which are not available yet:

$$\nabla \cdot (\varepsilon \nabla \phi^t) = -e(n_p^t - n_e^t - n_n^t). \tag{4.6}$$

By formulating a first order Taylor expansion approximation of n^t, this dielectric relaxation time constraint can be overcome (up to a factor 50 as was reported by Punset et al. (1999)):

$$n^t = n^{t-1} + \Delta t(\frac{\partial n}{\partial t})^{t-1}. \tag{4.7}$$

For the time derivative, the species continuity equations can be used:

$$\frac{\partial n}{\partial t} = S_k - \nabla \cdot \vec{\Gamma}_k. \tag{4.8}$$

S_k is the ionization/recombination source term specific for each species k. Substituting for the time derivatives yields:

$$\begin{aligned} n_p^t - n_e^t - n_n^t = n_p^{t-1} &- n_e^{t-1} - n_n^{t-1} \\ &+ \Delta t(-\nabla \cdot \vec{\Gamma}_p^{t-1} + \nabla \cdot \vec{\Gamma}_e^{t-1} + \nabla \cdot \vec{\Gamma}_n^{t-1}) \\ &+ \Delta t(S_p - S_e - S_n). \end{aligned} \tag{4.9}$$

The source terms cancel out completely, since each ionization and recombination is a process involving two of the three species, as was shown in Equation 3.42. The following approximation of the species number densities is obtained:

$$\begin{aligned} n_p^t - n_e^t - n_n^t = n_p^{t-1} &- n_e^{t-1} - n_n^{t-1} \\ &+ \Delta t(-\nabla \cdot \vec{\Gamma}_p^{t-1} + \nabla \cdot \vec{\Gamma}_e^{t-1} + \nabla \cdot \vec{\Gamma}_n^{t-1}). \end{aligned} \tag{4.10}$$

Substituting for the field values in Gauss' law:

$$\nabla \cdot (\varepsilon \nabla \phi^t) = -e(n_p^{t-1} - n_e^{t-1} - n_n^{t-1} - \Delta t\Big[\nabla \cdot \vec{\Gamma}_p^{t-1} - \nabla \cdot \vec{\Gamma}_e^{t-1} - \nabla \cdot \vec{\Gamma}_n^{t-1}\Big]). \tag{4.11}$$

Since the flux term is dependent on the electric field, another decomposition can be made. The flux terms can be written as:

$$\Gamma_k = v_k n_k = \mp \mu_k \vec{E} n_k - D_k \nabla(n_k). \tag{4.12}$$

Rewriting for the initial RHS in Equation 4.6:

$$\begin{aligned} n_p^t - n_e^t - n_n^t = n_p^{t-1} - n_e^{t-1} - n_n^{t-1} \\ - \Delta t \nabla \cdot (\mu_p \vec{E} n_p - D_p \nabla(n_p))^{t-1} \\ + \Delta t \nabla \cdot (-\mu_e \vec{E} n_e - D_e \nabla(n_e))^{t-1} \\ + \Delta t \nabla \cdot (-\mu_n \vec{E} n_n - D_n \nabla(n_n))^{t-1}. \end{aligned} \tag{4.13}$$

Reordering and implementing the relation $\vec{E} = -\nabla \phi$ yields:

$$\begin{aligned} n_p^t - n_e^t - n_n^t = n_p^{t-1} - n_e^{t-1} - n_n^{t-1} \\ + \Delta t \nabla \cdot (D_p \nabla(n_p) - D_e \nabla(n_e) - D_n \nabla(n_n))^{t-1} \\ + \Delta t \nabla \cdot (\mu_p n_p \nabla \phi + \mu_e n_e \nabla \phi + \mu_n n_n \nabla \phi)^{t-1}. \end{aligned} \tag{4.14}$$

Returning to the original Poisson equation, this now becomes:

$$\begin{aligned} \nabla \cdot (\frac{\varepsilon}{e} \nabla \phi^t) = -(n_p - n_e - n_n)^{t-1} \\ - \Delta t \nabla \cdot (D_p \nabla(n_p) - D_e \nabla(n_e) - D_n \nabla(n_n))^{t-1} \\ - \Delta t \nabla \cdot ((\mu_p n_p + \mu_e n_e + \mu_n n_n)^{t-1} \nabla \phi^t). \end{aligned} \tag{4.15}$$

The gradient term on the RHS is now taken at the new time step by multiplication of $1 = \frac{\phi}{\phi} \approx \frac{\phi^t}{\phi^{t-1}}$, such that this product becomes a correction term for the permittivity of the medium rather than a correction term for the number densities, as will become clear in the next step:

$$\begin{aligned} \nabla \cdot (\frac{\varepsilon}{e} + \Delta t(\mu_p n_p + \mu_e n_e + \mu_n n_n)^{t-1} \nabla \phi^t) = -(n_p - n_e - n_n)^{t-1} \\ - \Delta t \nabla \cdot (D_p \nabla(n_p) - D_e \nabla(n_e) - D_n \nabla(n_n))^{t-1} \end{aligned} \tag{4.16}$$

The summation of the $\mu_k n_k$ product on the LHS can be interpreted as the time rate of change of the permittivity of the fluid. The additional diffusion terms on the RHS can be calculated using the same schemes as used for the flux term for a zero drift velocity $U_k = 0$.

During the derivation of Equation 4.16, the assumption was made that $\phi^t/\phi^{t-1} \approx 1$. This puts a potential restriction on the time step:

$$\frac{\phi^t}{\phi^{t-1}} = \frac{\phi^{t-1} + \Delta t \frac{\partial \phi}{\partial t}}{\phi^{t-1}} = 1 + \frac{\Delta t}{\phi}\frac{\partial \phi}{\partial t} \approx 1.$$

For the sum of 1 and an additional term to be approximately 1, the additional term must be much smaller than 1, yielding the inequality:

$$|\frac{\Delta t}{\phi}\frac{\partial \phi}{\partial t}| \ll 1 \Longrightarrow \Delta t \ll |\frac{\phi}{\eta}|. \tag{4.17}$$

η is the time rate of change of the voltage ϕ, which is determined by the input voltage pulse. Considering the orders of magnitude:

$$\frac{\phi}{\eta} = \frac{\mathcal{O}(\phi)}{\mathcal{O}(\phi)/\mathcal{O}(T)} \Longrightarrow \Delta t \ll \mathcal{O}(T). \tag{4.18}$$

Which is in the order of magnitude of the characteristic actuation time. Since other processes require time restrictions which are much more severe (Table 2.1), it is safe to assume that this condition is always met in both nanosecond pulsed as well as continuous actuation discharge simulation and the proposed decomposition is valid.

The implementation is then done as follows:

```
// Calculate the effective permittivity of the gas.
eps = eps_g + runTime.deltaT()*Foam::constant::electromagnetic::e/epsilon0*(
    mue*Ne + mup*Np + mun*Nn);

// Predict species at current time index using information from the latest
    time index.
volScalarField Nek = Ne + runTime.deltaT()*fvc::laplacian(De,Ne);
volScalarField Npk = Np + runTime.deltaT()*fvc::laplacian(Dp,Np);
volScalarField Nnk = Nn + runTime.deltaT()*fvc::laplacian(Dn,Nn);

// Prevent negative species densities.
Nek == max(Nek, 0);
Npk == max(Npk, 0);
Nnk == max(Nnk, 0);
```

```
// Set up the equation matrix using the newly predicted species densities.
fvScalarMatrix phiEqn
(
  fvm::laplacian(eps,phi)
  ==
  - Foam::constant::electromagnetic::e/epsilon0*(Npk - Nek - Nnk)
);

// Solve the equation matrix.
phiEqn.solve();
```

4.3 Semi-implicit formulation of the continuity equations

The governing equations for the species densities have been derived in section 3.2 and are written as:

$$\frac{\partial n_e}{\partial t} + \nabla \cdot U_e n_e - \nabla \cdot D_e \nabla(n_e) = (\alpha - \eta)|\vec{\Gamma}_e| - n_e n_p \beta_{ei}, \tag{4.19}$$

$$\frac{\partial n_p}{\partial t} + \nabla \cdot U_p n_p - \nabla \cdot D_p \nabla(n_p) = \alpha|\vec{\Gamma}_e| - n_e n_p \beta_{ei} - n_n n_p \beta_{ii}, \tag{4.20}$$

$$\frac{\partial n_n}{\partial t} - \nabla \cdot U_n n_n - \nabla \cdot D_n \nabla(n_n) = \eta|\vec{\Gamma}_e| - n_n n_p \beta_{ii}. \tag{4.21}$$

Where $|\vec{\Gamma}_e| = |\vec{U}_e n_e|$ is the ionization collision flux. The continuity equations are strongly coupled, and require a special approach on solving them sequentially. Multiple techniques are available, but only the method of source splitting will be discussed here. The method relies on making the distinction between the **H**omogeneous terms and the **R**eaction terms:

$$\frac{\partial n_k}{\partial t}(\Delta t) = H(n_k) + R(n_k). \tag{4.22}$$

The RHS is split, and the split relations are integrated over time sequentially. The procedure can consist of $M = 2, 4, 6..$ sub-iterations, where a sub-iteration $1 \leq i \leq M$. The example is given for $M = 2$:

$$\frac{\partial n_k^{t+1/2}}{\partial t}(\Delta\tau) = H(n_k^t) \quad \text{with} \quad \Delta\tau = \Delta t, \tag{4.23}$$

$$\frac{\partial n_k^{t+1}}{\partial t}(\Delta\tau) = R(n_k^{t+1/2}) \quad \text{with} \quad \Delta\tau = \Delta t. \tag{4.24}$$

The relations above simply state that a number of total iterations M is chosen. The first $M-1$ sweeps are used to sequentially integrate the homogeneous terms forward in time using an implicit temporal scheme, where each sub-iteration i uses the solution of the former sub-iteration $i-1$. In a final sweep, the reaction terms are integrated explicitly over the original time step Δt. This kind of splitting is called Godunov splitting and is presented in literature as a common approach to handling the strong coupling between the different species, e.g. by Jayaraman et al. (2007); Abdollahzadeh et al. (2016). Strang splitting is an alternative to this method, in which the sweeps are performed in a symmetric order. An odd number of sweeps are required for this splitting, i.e. $M = 3, 5, 7..$, and the reaction terms are always integrated explicitly at the middle iteration $(M+1)/2$. The homogeneous terms are integrated implicitly. The example is given for $M = 3$:

$$\frac{\partial n_k^{t+1/3}}{\partial t}(\Delta\tau) = H(n_k^t) \quad \text{with} \quad \Delta\tau = \Delta t/2, \tag{4.25}$$

$$\frac{\partial n_k^{t+2/3}}{\partial t}(\Delta\tau) = R(n_k^{t+1/3}) \quad \text{with} \quad \Delta\tau = \Delta t, \tag{4.26}$$

$$\frac{\partial n_k^{t+1}}{\partial t}(\Delta\tau) = H(n_k^{t+2/3}) \quad \text{with} \quad \Delta\tau = \Delta t/2. \tag{4.27}$$

The sub-cycling is implemented using the built-in `subCycle` utility. This functionality alters the current time index of the corresponding volume field, assuring that sub-iterations are stored as t+i/N and the final iteration corresponds to the current time step t+1, instead of t+N which would be the case of the time indices are not corrected.

In the beginning of this section, it was explained that OpenFoam® uses iterative solution methods to solve differential equations. Also, in the explanation of sub-cycling given above, it was mentioned that the homogeneous terms are integrated implicitly over time. This implicit functionality is utilized by using the `fvm::` class, which tells OpenFoam® to add the coefficients of the `fvm::` operator to the matrix A it constructs when an equation matrix is build. The derived form of the governing equations easily allows for this, as the flux term Γ_k was already decomposed, and since all the terms in:

$$\frac{\partial n_k}{\partial t} + \nabla \cdot U_k n_k - \nabla \cdot D_k \nabla n_k = 0, \tag{4.28}$$

contain the variable n_k, this equation can be implicitly implemented as:

```
fvScalarMatrix exampleEqn
(
    fvm::ddt(Nk)
  + fvm::div(kFlux,Nk)
  - fvm::laplacian(Dk,Nk)
  ==
    0
);
```

The term `kFlux` requires some additional explanation. OpenFoam® is a finite volume method based package, and where the governing equation describes the Cartesian system based cell velocity $\vec{U}_k$, most spatial discretization schemes in a finite volume formulation require the surface normal flux, `kFlux`. This term is obtained by interpolation of the velocity to the interface surface, and by transformation of the surface vector to a surface scalar by inner-multiplication with the surface normal vectors:

```
surfaceScalarField kFlux = fvc::interpolate(Uk) & mesh.Sf();
```

The source R step for e.g. the electrons is implemented as:

```
fvScalarMatrix exampleEqn
(
    fvm::ddt(Ne)
  ==
    (alpha - eta)*magUe*Ne - betaep*Ne*Np
);
```

While both the Godunov and Strang splitting methods were implemented, only the Strang splitting method was used in the rest of this work.

4.4 Mobility and reaction rate coefficients

In the formulation of the drift-diffusion equations, a number of parameters are still unknown and have to be modelled. These parameters are the transportation coefficients μ and D, termed mobility and diffusion coefficient respectively, and the reaction rate coefficients β, α and η, termed the recombination, ionization and attachment coefficients, respectively. The incorporated chemical reactions together with the parent gas composition determine the values or relations for these variables, and so the model through which these values are obtained represents the chemical model of this problem description. Goekce (2014) summarizes the most important processes for non-equilibrium cold plasma:

- Two-body electron-impact ionization, collisional excitation of neutral species by electrons;
- Two- and three-body attachment, binding of electrons to electronegative species;
- Two- and three-body ion-ion recombination, binding of positive and negative ions;
- Two- and three-body electron-ion recombination, binding of positive ions and electrons.

Regarding the mobility coefficients, the influential parameters are the type of the gas (species and mixture ratio), the reduced electric field E/N and the pressure and temperature of the gas T_g and P_g, respectively.

There are multiple ways to obtain the mobility and rate coefficients required for this way of plasma modelling. Some methods simply assume constant values for these coefficients, while others use phenomenological relations (look-up tables), or a combination hereof. In this work, the Bolsig+ software developed by Hagelaar and Pitchford (2005) is used. Through this software, look-up tables can be obtained, which approximate the values of the coefficients as a function of the reduced electrical field. This follows from the LFA (section 3.2), which assumed that the electron gained energy is only a function of the local E/N. This implies that also the mobility and reaction rate coefficients are dependent of the local E/N. The curve-fitting formulas are obtained by solving the electron Boltzmann equation using a two-term approximation based on collision cross-section data, i.e. the involved reactive species. A steady-state solution is then obtained valid for a uniform electric field with uniform or exponentially growing electron densities. The solver is able to account for different spatial growth models, quasi-stationary and oscillating fields and collision reactions between electron-neutral and electron-electron species. The solver was developed specifically for application to fluid models, which, combined with the aforementioned properties, makes it suitable for application to numerical simulation of DBD actuators.

The LXCAT website [2] provides an on-line tool presented in the work of Pancheshnyi et al. (2012), with which the computations for the electron properties in a gas (mixture) can be performed. In this study, two types of gas are considered: helium and air. Using the Bolsig+ solver calculations (on the LXCAT website) were performed and the results are presented in this chapter. All calculations were done at a gas pressure of 760Torr and a temperature of 300K under the assumption of a non-Maxwellian Electron Energy Distribution Function (EEDF), as the ionization degree is low. It should be noted that Bolsig+ provides swarm parameters for electrons; parameters for the heavy species are obtained from literature. Additionally, from the Bolsig+ solver energy loss fractions can be obtained. These fractions were introduced in section 2.6 and treated in section 2.7 and section 3.4 and describe the distribution of the energy lost by the electrons during collisions and absorbed in different modes by the neutral particles.

Alternative models found in literature are given in Appendix C, but are not applied in this work. The graphs presented in this chapter are results from simulations performed with the Bolsig+ software for the reaction rates α and η, the transport coefficients μ_e and D_e and the energy loss fractions η_E, η_{VT} and η_{el-R}. Additionally, constant values or curve-fitting relations obtained from literature are given for the heavy species transport coefficients $\mu_{p,n}$ and $D_{p,n}$ and the recombination coefficients β_{ei} and β_{ii}. To implement the simulation data into the solver, spline interpolation is used to interpolate between the discrete data points:

A routine has been implemented which, for an arbitrary value of the reduced electric field `Td`, finds the two closest corresponding indices of the E/N table `ENtable` obtained from Bolsig+. Through linear interpolation, the corresponding reaction rate and electron transport

---

[2] www.lxcat.net/SIGLO

coefficients are calculated:

$$\alpha(\mathrm{E/N}) = \alpha_0 + \frac{\partial \alpha}{\partial \mathrm{E/N}} \Delta \mathrm{E/N}. \tag{4.29}$$

The simulation data is spaced equally on a logarithmic scale, i.e. at a constant $\Delta\mathrm{E/N} = 10^{\Delta x}$, which is used to find the index of the E/N table. When the input `Td` is out of bounds, the data is extrapolated. This is to prevent runtime errors, but preferably this should be avoided as validity cannot be guaranteed any more.

```
// Get the coordinates of the mesh cell centres.
const volVectorField& Cp = mesh.C();

// Get the 10log value of the first (0) and the last (end) E/N table index.
scalar logEN0 = Foam::log(ENtable[0] + SMALL)/Foam::log(10.0);
scalar logENend = Foam::log(ENtable[tableSize - 1] + SMALL)/Foam::log(10.0);

// Loop over all cells with current index p.
forAll(Cp,p)
{
  // Store the reduced electric field Td computed in the current cell p.
  scalar EN = Td[p];

  // Get its 10log value.
  scalar logEN = Foam::log(EN + SMALL)/Foam::log(10.0);

  // Find the closest corresponding table index.
  int q = min(max(round((logEN - logEN0)/dlogEN),1),tableSize) - 1;

  int qupper = -1; int qlower = -1;

  // Find the upper and lower cell indices used for inter- or extrapolation.
  if (EN > ENtable[q])
  {
   if (q != tableSize - 1) // interpolate between two closest points
   {
    qupper = q + 1;
    qlower = q;
   }
   else //Extrapolate from last two points
   {
    qupper = q;
    qlower = q - 1;
   }
  }
  else
  {
    if (q != 0) // interpolate between two closest points
   {
    qupper = q;
    qlower = q - 1;
   }
   else // extrapolate from first two points
```

```
    {
     qupper = q + 1;
     qlower = q;
    }
  }

// Compute the ionization rate alpha by multiplication of the value (.value())
     of the gas neutral particle density Ng with the value of alpha/N
    interpolated from the table "alphatable".
alpha[p] = Ng.value()*(alphatable[qlower] + (alphatable[qupper] - alphatable[
    qlower])/(ENtable[qupper] - ENtable[qlower])*(EN - ENtable[qlower]));
```

4.4.1 Properties of helium

In this section, properties of helium will be discussed. Helium is used in a number of papers and is convenient since it, as it is a rare gas, only electrons and (higher) excited states of atomic helium, He, and molecular helium, He_2, have to be taken into account.

In experimental work, obtaining a pure helium mixture is very challenging, and most often impurities are found which influence the discharge characteristics in the gas (Massines et al. (1998)). This effect is called Penning ionization, where interaction between mostly N_2 impurities and helium metastable states cause ionization of these impurities, which is due to the high energy threshold of helium metastable states compared to that of the impurities. The effect is clearly visible in Figure 4.3. A small percentage of argon (0.5%) is added to the mixture, which strongly increases the ionization rate of helium at lower reduced electric field values.

Note that this result is not simply obtained by linearly adding the ionization rate proportionally; the addition has highly non-linear effects. The strong effect Penning ionization has becomes evident when the mixture mobilities are compared to those of pure helium. The lack of difference between the He-0.5%Ar and the He **electron mobility** curves in Figure 4.4 emphasizes the negligible amount of argon added.

In the work of Ward (1962), helium **ion mobility** is given in the form of the following relation, which is a fit of experimentally obtained ion velocities (in units of cm). Generally, the ion velocity is an order of 10^2 lower than the electron velocity:

$$\mu_p p_g = \begin{cases} 8.0\times 10^3(1-8.0\times 10^{-3}|E/p|) & \text{if } |E/p| \leq 25\text{V cm-1 Torr-1}, \\ 4.1\times 10^4/\sqrt{|E/p|}(1-27.44/\sqrt{|E/p|^3}) & \text{if } |E/p| > 25\text{V cm-1 Torr-1} \end{cases} \tag{4.30}$$

The diffusion coefficient again is given by Einstein's relation, where the temperature T_k^* is in

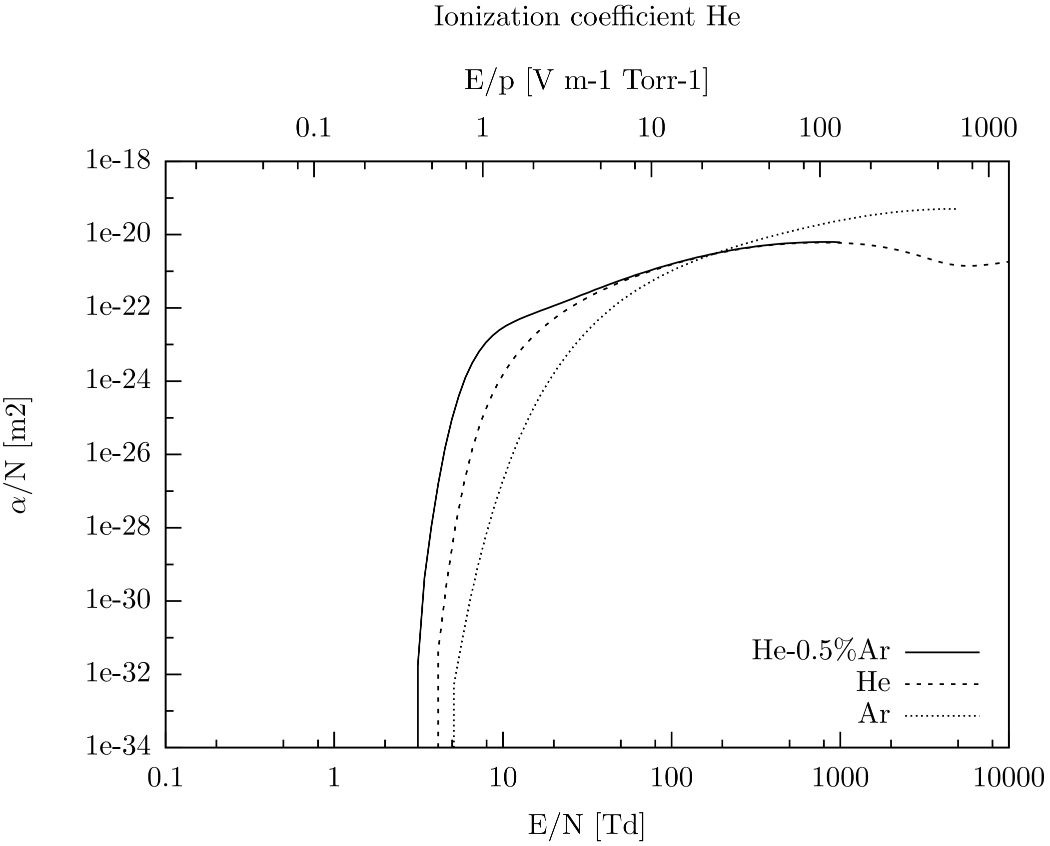

Figure 4.3: Reaction rate coefficients of the Ar-He mixture in comparison with the original distributions for pure argon and pure helium. Penning ionization strongly increases the ionization rate of the mixture at lower values of E/N.

eV and has a constant value of 0.026:

$$D_p = \mu_p T_p^*. \tag{4.31}$$

Recombination rates depend on the species taken into account, as shown in Golubovskii et al. (2002a); Mangolini et al. (2004). In this work, the recombination rate for atomic helium is used:

$$\beta_{ei} = 8 \times 10^{-20} \left(\frac{T_g}{T_e}\right)^4 \mathrm{cm}^6 \mathrm{s}^{-1}. \tag{4.32}$$

Both pure helium and argon are electro-positive gases, i.e. they have a tendency to repel electrons, and so $\beta_{ii} = 0$ as negative ions do not occur in its plasma.

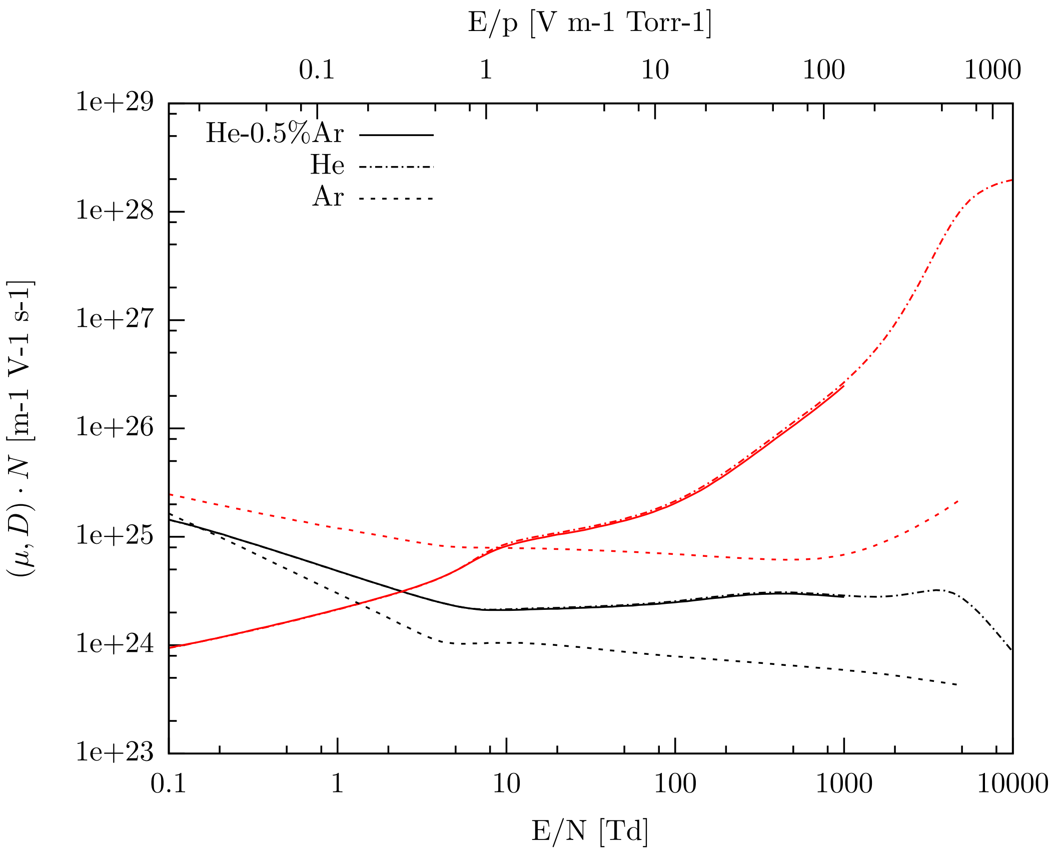

Figure 4.4: Electron **mobility** and diffusion coefficients for the Ar-He mixture, and the pure parent gases Ar and He. The transport coefficients are hardly altered by the addition of Ar.

The electric field is a source of potential energy, from which mainly electrons extract energy in different modes. The distribution of three modes with varying electric field strength is shown in Figure 4.5. The black curve corresponds to the power fraction η_{el-R} and represents elastic collisions (i.e. collisions without energy loss) and rotational excitation. The vibrational curve corresponds to η_{VT}: vibrational and translational acceleration of electrons. Lastly, the growth curve is related to η_E; the electronic excitation of atoms which results in ionization, attachment and dissociation. Following the LFA, all energy obtained by electrons is directly deposited into the neutral flow, so these fractions quantify the energy deposition during a discharge. Three different stages can be observed, where each mode is dominant over a range of reduced electric field strength. For low values hereof, vibrational and electronic excitation are negligible, and all energy absorbed by the electrons leads to elastic (i.e. energy conserving) collisions. With increasing values of the electric field, the vibrational mode is excited first for intermediate values, followed by electronic excitation, leading to ionization first and dissociation after. This is in correspondence to observations made in e.g. high temperature gas dynamics: with rising gas temperature, the thermal heat first excites vibrational modes, after which particles ionize and finally dissociate.

Also in Figure 4.5, the differences between helium and argon demonstrated in Figure 4.3 become evident. Argon can absorb much more energy in its vibrational mode than helium,

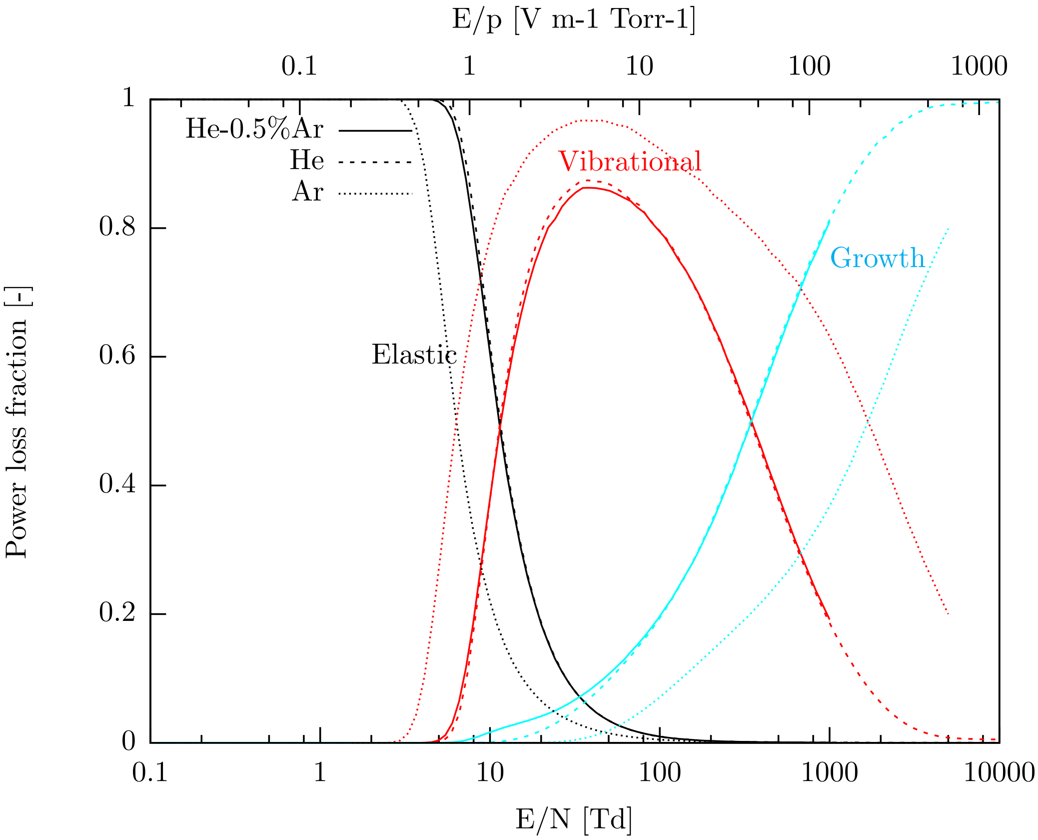

Figure 4.5: Power fractions for He-Ar mixture and pure He and pure Ar obtained with the Bolsig+ solver as a function of E/N (lower axis) and E/p (upper axis) under the assumption of a non-Maxwellian EEDF at $T_g = 300$.

and so only in stronger electric fields are electrons energized enough to get excited.

4.4.2 Properties of air

Air is a mixture consisting of 79% -21% $N_2 - O_2$, and while nitrogen is an electro-positive species, oxygen is not. This means that the attachment coefficient is non-zero and ion-ion recombination occurs.

An extensive list of reactions is given in Kossyi et al. (1992). The addition of oxygen has some strong influence on the processes in the plasma. Not only the chemical products are different, but the capability of oxygen to bind electrons to its molecules is an additional electron destruction process, one that can delay breakdown significantly. As depicted in Figure 4.6, breakdown is only possible above electric field values of 100 Td, where in helium and argon, this is already for electric fields in the order of 10 Td. Comparing the orders of magnitude of the mobility and diffusion coefficients, the values of those coefficients is much more constant for the air mixture than for the noble gases, with variation in the order of 2 and 4, respectively.

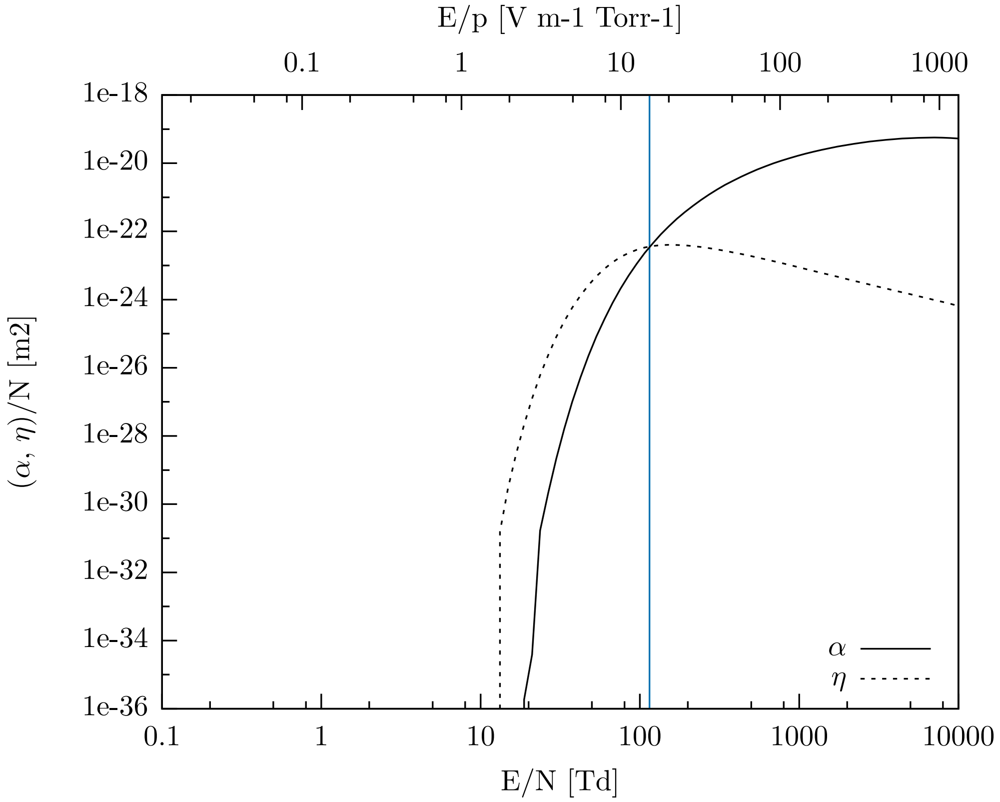

Figure 4.6: Reaction rate coefficients for air obtained with the Bolsig+ solver as a function of E/N (lower axis) and E/p (upper axis) under the assumption of a non-Maxwellian EEDF at $T_g = 300$K. Air has an ionization as well as an attachment coefficient. The blue line indicates the intersection between the two: for reduced electric field values above this line, the ionization factor becomes dominant and breakdown can occur as electrons are not dominantly attached to oxygen molecules any more.

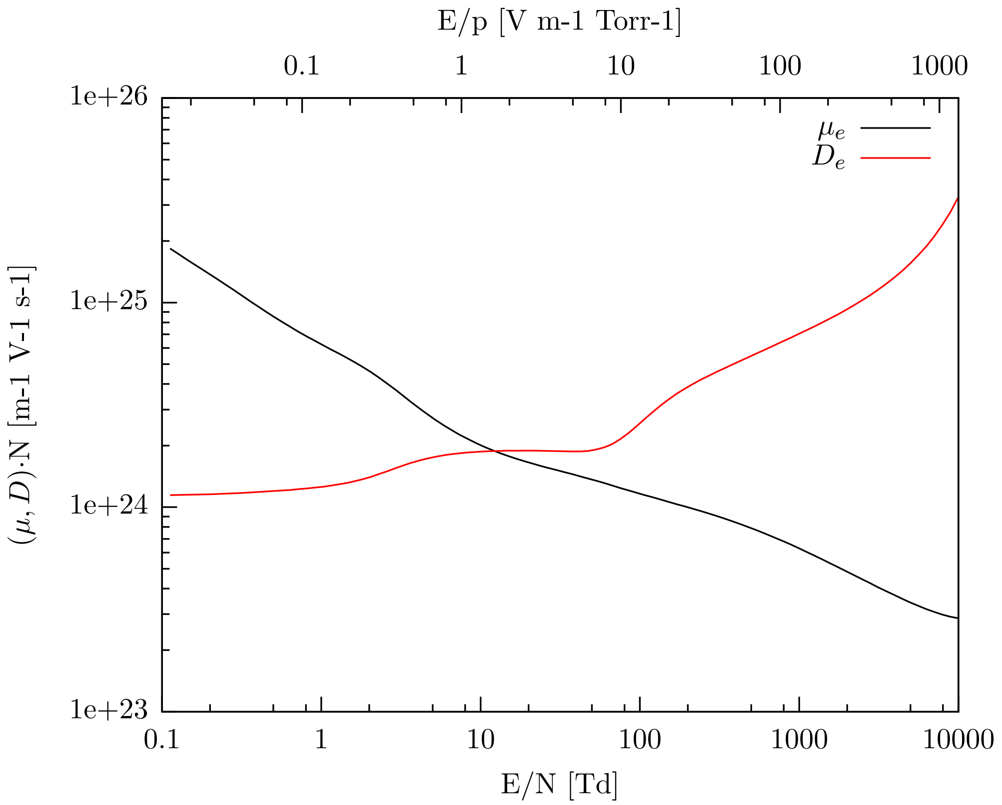

Figure 4.7: Mobility and diffusion coefficients for air obtained with the Bolsig+ solver as a function of E/N (lower axis) and E/p (upper axis) under the assumption of a non-Maxwellian EEDF at $T_g = 300$K.

The mobility coefficients of the positive and negative ions are assumed to be only dependent on the gas pressure (Goekce (2014)). Alternative relations are given by Hoskinson (2009) and can be found in Equation C.15.

$$\begin{aligned} \mu_p p_g &= 20 \quad [\mathrm{m^2 Torr (Vs)^{-1}}], \\ \mu_n p_g &= 20 \quad [\mathrm{m^2 Torr (Vs)^{-1}}]. \end{aligned} \tag{4.33}$$

To obtain the diffusion coefficient, Einstein's relation for diffusivity is used:

$$D_{p,n} = \mu_{p,n} T^*_{p,n}. \tag{4.34}$$

The temperature T^*_k is in eV and has a constant value of 0.026 for both species. The recombination coefficients describe the recombination reactions between electrons-ions and ions-ions. The coefficient β_{ei} accounts for destruction of both electrons and positive ions, whereas the coefficient β_{ii} accounts for destruction of both positive and negative ions. These coefficients are assumed to be constant and their values have been taken from Boeuf et al. (2007):

$$\begin{aligned} \beta_{ei} &= 2.0 \times 10^{-13} \quad [\mathrm{m^3 s^{-1}}], \\ \beta_{ii} &= 1.7 \times 10^{-13} \quad [\mathrm{m^3 s^{-1}}]. \end{aligned} \tag{4.35}$$

In Figure 4.8, the power fractions are presented. Compared to the distributions for helium, the vibrational excitation is dominant for a much wider range of electric field strength. Only for electric field values of higher than 100 Td, energy is spent on electronic excitation. This corresponds to the data shown in Figure 4.6, wherein only after 100 Td the electronic excitation becomes significant. This also reflects the stronger isolating properties air is characterised by in comparison to helium.

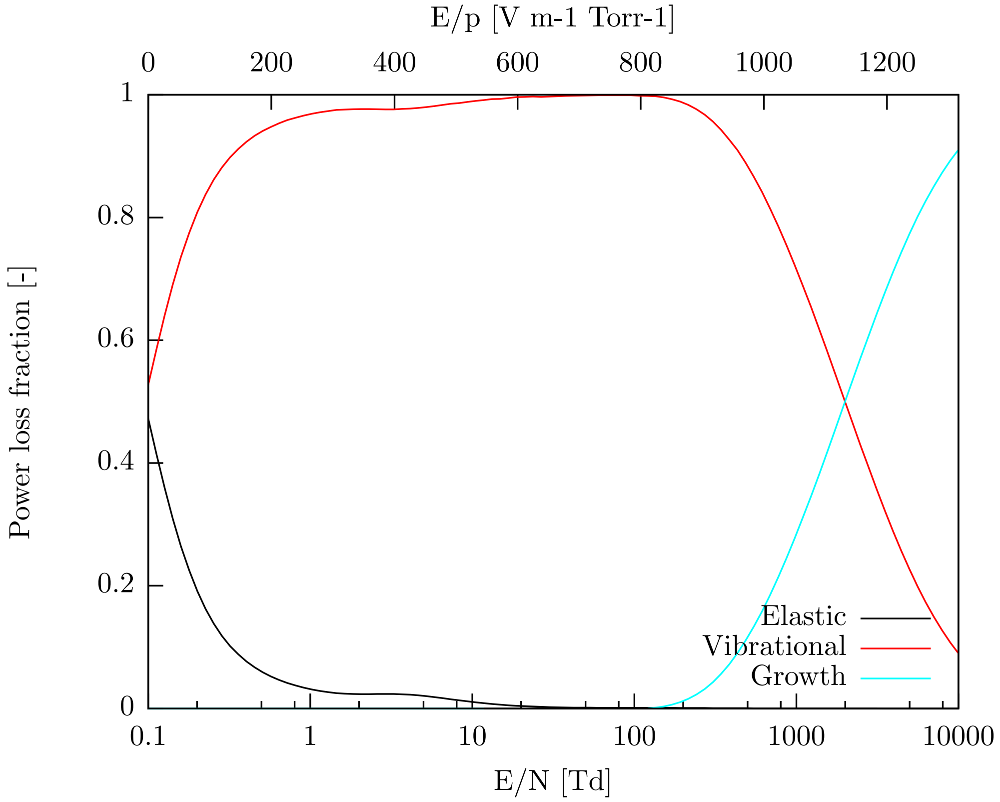

Figure 4.8: Power fractions for air obtained with the Bolsig+ solver as a function of E/N (lower axis) and E/p (upper axis) under the assumption of a non-Maxwellian EEDF at $T_g = 300$K.

4.5 Boundary and initial conditions

In section 3.3, the analytical boundary conditions which define the problem definition were elaborated on. In this chapter, discretization and implementation of these conditions is treated.

Electric potential conditions

The fluid and dielectric region share an interface which couples the electric fields in the two regions. No such boundary condition is available directly in OpenFoam® , so this coupling has to be implemented. As explained in section 3.3, the compatibility equation is given by:

$$\hat{n} \cdot (\varepsilon_0 \varepsilon_g E_{gas} - \varepsilon_0 \varepsilon_d E_{dielectric}) = \sigma. \tag{4.36}$$

This relation will be rewritten into a central difference discrete formulation such that it is implementable into the numerical solver. Using the definition of the electric field $E = -\nabla\phi$ and discretizing the terms:

$$-\varepsilon_g \varepsilon_0 \frac{\phi_{gas} - \phi_{interface}}{\Delta_{gas}} + \varepsilon_0 \varepsilon_d \frac{\phi_{interface} - \phi_{dielectric}}{\Delta_{dielectric}} = \sigma \tag{4.37}$$

Use was made of the identity $\hat{n} \cdot \partial/\partial y = \partial/\partial n$. Note that this is a first order discretization. This will make the whole Poisson scheme first order as well, as will be shown in chapter 5. The latter term is directly expressed as the absolute distance from the corresponding boundary cell centre to the cell boundary face, Δ. Then, collecting terms gives:

$$(\frac{\varepsilon_g}{\Delta_{gas}} + \frac{\varepsilon_d}{\Delta_{dielectric}})\phi_{interface} = \frac{\varepsilon_g \phi_{gas}}{\Delta_{gas}} + \frac{\varepsilon_d \phi_{dielectric}}{\Delta_{dielectric}} + \frac{\sigma}{\varepsilon_0} \tag{4.38}$$

The expression for the updated interface value becomes:

$$\phi_{interface} = \frac{\varepsilon_g \phi_g/\Delta_g + \varepsilon_d \phi_d/\Delta_d + \sigma/\varepsilon_0}{1/\Delta_g + \varepsilon_d/\Delta_d} \tag{4.39}$$

This boundary condition is applied for both the dielectric as well as the fluid region and can be interpreted as a weighted averaging of the internal field values of ϕ. The weighting term is the relative permittivity divided by the cell to face distance ε_r/Δ.

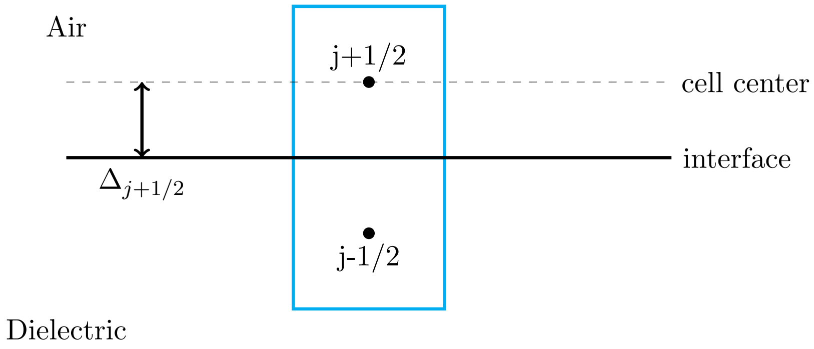

Figure 4.9: Region interface layout

To show how this single relation behaves as an iterative routine for which a converged value will be found, the recursive form is presented. Since the fluid and dielectric region are solved sequentially and the dielectric region is solved first, we consider the solving step of the dielectric $k+1/2$ while that of the fluid region $k+1$. If interface j is considered, subscript $j-1/2$ and $j+1/2$ denote the dielectric and fluid cell values, respectively:

Find interface boundary value

$$\phi_j^{k+1/2} = \frac{\phi_{j+1/2}^{k}/\Delta_{j+1/2} + \varepsilon_d \phi_{j-1/2}^{k}/\Delta_{j-1/2} + \sigma^k/\varepsilon_0}{1/\Delta_{j+1/2} + \varepsilon_d/\Delta_{j+1/2}}$$

Solve for the dielectric region

$$\nabla^2 \phi = 0 \Rightarrow \phi_{j-1/2}^{k+1}$$

Find interface boundary value with updated $\phi_{j-1/2}$

$$\phi_j^{k+1} = \frac{\phi_{j+1/2}^{k}/\Delta_{j+1/2} + \varepsilon_d \phi_{j-1/2}^{k+1}/\Delta_{j-1/2} + \sigma^k/\varepsilon_0}{1/\Delta_{j+1/2} + \varepsilon_d/\Delta_{j+1/2}}$$

Solve for the fluid region

$$\nabla^2 \phi = -\frac{\rho_c}{\varepsilon_0} \Rightarrow \phi_{j+1/2}^{k+1}$$

The segregated manner in which the different regions are solved can be regarded as one linear system $Ax = b$ describing a model problem consisting of N cells, where N is the number of coupled regions. The fluxes between the different regions are solved for using the coupling condition given in Equation 5.1. The solution inside each individual cell (which represents a whole physical region) is solved using a pre-conditioned conjugate gradient (PCG) method. The regions are solved sequentially, such that the moment one region is solved for, up-to-date information for the adjacent region becomes available. This is typical for a Gauss-Seidel iterative solution method and has improved convergence rates compared to a Jacobian method, in which all regions would be solved parallel using only the information from the former iteration. the Gauss-Seidel method allows for over-relaxation: acceleration of the convergence by applying a relaxation factor α to the following decomposition:

$$\phi^{k+1} = \phi^{k} - \alpha(\phi^{k} - \phi^{k+1/2}). \tag{4.40}$$

The value of $\phi^{k+1/2}$ is the updated flux value on the region interface. According to Carré (1961), the solution always converges for a relaxation factor of $0 \leq \alpha \leq 2$ and depends on the eigenvalues of the coefficient matrix A.

This routine is repeated until the norm of the relative residual between two iterations r_ϕ drops below a convergence criterion ϵ:

$$r_\phi = \frac{|\varepsilon_0 \varepsilon_g E_g \cdot \hat{n} - \sigma - \varepsilon_0 \varepsilon_d E_d \cdot \hat{n}|}{|\varepsilon_0 \varepsilon_g E_g \cdot \hat{n} - \sigma| + |\varepsilon_0 \varepsilon_d E_d \cdot \hat{n}|} > 0. \tag{4.41}$$

This criterion can be set manually, but by default has a value of $\epsilon = 10^{-3}$. In the relation above, the charge surface density at time step k is required.

The boundary condition is implemented into the solver by use of the groovyBC [3] functionality. An example snippet of the changeDictionaryDict of the gas region is given below. The changeDictionary functionality is further explained in Appendix A.

```
dictionaryReplacement
{
    phi
    {
        internalField   uniform 0;

        boundaryField
        {
            "air_to_dielectric.*"
            {
                type            groovyBC;
                value           $internalField;
                valueExpression "phi - rAlpha*(phi - (phiD*epsilonD/DeltaD +
                    phiA*epsilonA/DeltaA + rhoSurf/epsilon0)/(epsilonA/DeltaA
                    + epsilonD/DeltaD))";
                variables ( "phiD=mappedInternal(phi);"
                            "phiA=internalField(phi);"
                            "DeltaD{dielectric_to_air/dielectric}=dist();"
                            "DeltaA=dist();"
                            "epsilon0=8.85419e-12;"
                            "rhoSurf=sigma/mag(Sf());"
                          );
```

---

[3] https://openfoamwiki.net/index.php/Contrib/groovyBC

```
            }
        }
    }
}
```

Implementation of the particle velocity conditions

The particle velocity boundary conditions are implemented in the source code of the solver by accessing the patch fields of the vector fields, which is a property of each volume field. As only the normal components are to be altered, the conditions are imposed on the flux term `kFlux`, which is the velocity `Uk` interpolated to the cell interfaces (section 4.3). An example snippet for correcting the flux boundary values of the positive ion specie is given below. Additional explanation on coding in OpenFoam® can be found in Appendix A.

```
// Interpolate thermal velocity volume scalar to cell interfaces and scale by
    the interface surface (magSf()).
surfaceScalarField ssfUpth = fvc::interpolate(Upth)*mesh.magSf();

// Loop over all the patches available in the mesh of the current region.
forAll(mesh.boundary(), patchi)
{
  // Create read-only (const) pointer (&) p to the current patch with index
      patchi.
  const fvPatch& p = mesh.boundary()[patchi];

  // Create read-write pointer (&) ppFlux to the s(urface)PatchScalarField of
      pFlux.
  fvsPatchScalarField& ppFlux = pFlux.boundaryField()[patchi];

  // Create read-only pointer (&) pUp to the PatchVectorField of Up.
  const fvPatchVectorField& pUp = Up.boundaryField()[patchi];

  // Check that the accessed patch is not of the coupled type.
  if (!ppFlux.coupled())
  {
    // Access (==) and set the electron flux sPatchScalarField ppFlux equal to
        the inner product (&) of the patch normal vector p.Sf() and the
       internal field vector from the adjacent cell centre pUp.internalField
       ().
    ppFlux == 0.25*pssfUpth + max(p.Sf()&pUp.patchInternalField(),0.0);
  }
}
```

Implementation of the number density conditions

The number density boundary values are required for finding the appropriate flux term values on the boundaries from the momentum equation. It was explained in section 3.3 that a zero gradient condition can be imposed on all boundaries. OpenFoam® needs no particular implementation for this, and the conditions can be enforced straight forward in the case folder, e.g. using:

```
Ne
{
    internalField    uniform 1.0e16;

    boundaryField
    {
        ".*"
        {
            type             zeroGradient;
        }
    }
}
```

4.6 Numerical procedure

In the section, the solver architecture and numerical procedure will be elaborated on. The solver consists of three units:

1. the coupled-Poisson solver;
2. the convection-diffusion model for species transportation;
3. the reactive modelling of the chemical reactions.

As all units are strongly coupled, a predictor-corrector like implementation has been selected. The undertaken steps are explained below. The procedure is visualized in Figure 4.10.

Predictor step - At the start of a new time index, only information from the latest time index is available, while the solution to the Poisson equation requires the values of the space charge at the current time index. To overcome this initial value problem, a prediction of the electric field is made.

1. At a new time step, the potential on the anode has changed and is updated first;
2. The electric field in the dielectric regions is updated according to the new anode potential. This is done first as the latest information available comes from the anode region which the dielectric has direct access to;
3. The electric field in the gas region is updated according to the new anode and dielectric potentials. This requires species densities in the new time index, which are not known yet. Using the semi-implicit Poisson equation derived in section 4.2, the charge volume density is predicted using a first order approximation based on the data from the last time index. Also the surface charge is predicted in the same manner. The Poisson

equation is solved and a first prediction of the electric field is obtained. The predictor step is complete.

Corrector step - A basis for the solution of the current time step has been obtained in the predictor step. The solution will now be corrected to a convergent state at the current time index by means of iteration, sequentially updating the species number densities and the electric field.

1. Using the predicted electric field values, the reaction rate and mobility coefficients are updated, which all depend on the reduced electric field strength. The velocities and velocity boundary conditions are updated accordingly.

2. The number densities are found by solving the continuity equations using the Godunov or Strang splitting technique, and the charge volume and surface densities are updated accordingly. The currents, power deposition and body forcing resulting from the gas discharge are calculated as well. The rate of change of the EHD force is used to check convergence of the solution.

3. With the new charge volume and surface densities, the electric field can be corrected. The fully implicit Poisson equation can now be used, as the charge density does not have to be predicted any more. The fluid region is updated first to directly use the newly available information in this region. Then the dielectric regions are updated. The coupling condition between the fluid and dielectric is used as a means to check convergence. The fluid and solid regions are updated one after the other until convergence is achieved.

4. When both the electric field and the density fields have converged, the solver advances in time and restarts the prediction routine. When the density fields have not converged, the corrector step is repeated.

To visualize the process, a time advancement chart has been created which is presented in Figure 4.10. This chart indicates the order in which variables are updated. Each variable is situated on a specific row, corresponding to the equation used to find this variable. In some steps, multiple variables are updated at once, but only one has been included in the graph. These variables are depicted in Table 4.1.

The two manually set tolerances ϵ_ϕ and ϵ_n are compared to two convergence criteria r_ϕ and r_n, respectively, given by:

$$r_\phi = \frac{|\varepsilon_0 \varepsilon_g E_g \cdot \hat{n} - \sigma - \varepsilon_0 \varepsilon_d E_d \cdot \hat{n}|}{|\varepsilon_0 \varepsilon_g E_g \cdot \hat{n} - \sigma| + |\varepsilon_0 \varepsilon_d E_d \cdot \hat{n}|}, \tag{4.42}$$

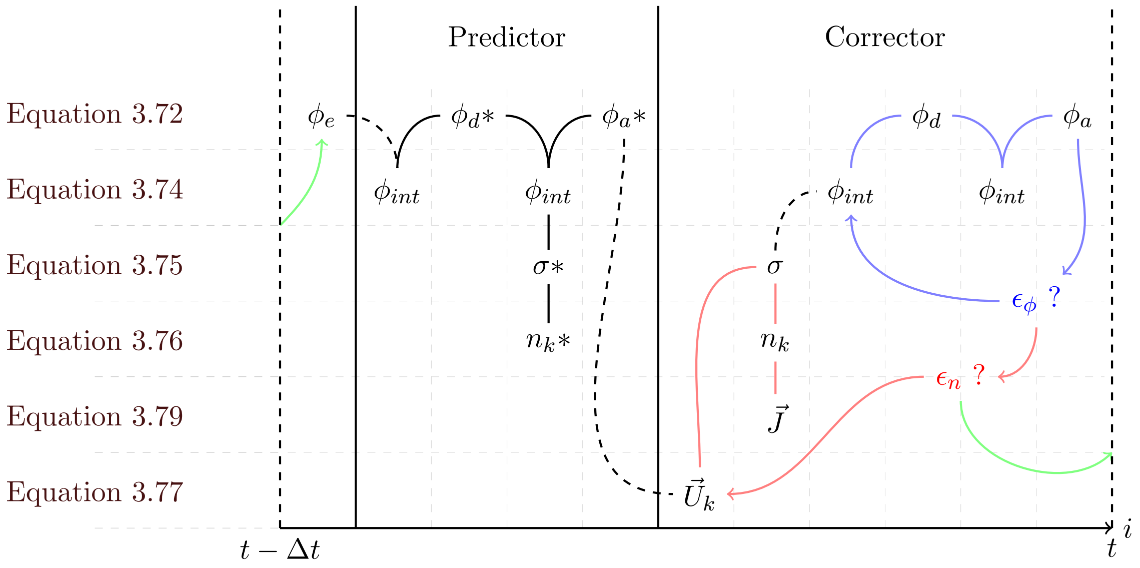

Figure 4.10: Advancement of variables in a time step. On the axis, the time increment from $t-\Delta t$ to t is indicated. The solver starts on the left and with every calculation advances to the right. The procedure starts by updating the input potential on the electrode. Then the predictor step is executed, followed by two loops in the corrector step. The predictor and corrector steps are explained above.

and

$$r_n = \frac{||\vec{F}^t - \vec{F}^{t-1}||}{||\vec{F}^{t-1}||}. \tag{4.43}$$

The first was already introduced in Equation 4.41, the latter is the relative increment of the EHD force. This force is a function of $\rho_c\vec{E}$, which means it is a good condition for checking the rate of change of the residual vectors of both the electric field and the species density numbers.

ϕ_R	$\vec{U}_k$	n_k	$\vec{J}$
$\vec{E}_R$	α,η	ρ	P,E
E/N$_R$	μ_k,D_k		$\vec{F}$,$\vec{M}$

Table 4.1: Variable updating according to Figure 4.10. The subscript R indicates the region to which the variable belongs, while subscript k indicates the species. The variables under $\vec{J}$ only exist in the fluid region.

Time stepping

The Courant-Friedrichs-Lewy (CFL) Courant et al. (1928) condition, or Courant number, is used for the time step control. The species particle velocities are used to evaluate the ratio of the distanced $v_k \Delta t$ travelled by said particles over the local length scale, determined by the local cell size Δx:

$$\mathrm{CFL} = \frac{v_k \Delta t}{\Delta x}. \tag{4.44}$$

In this work, the Courant number is limited by a maximum value of 0.7 and a maximum relative increase in value of 30% to prevent oscillations caused by changes in the time step. The maximum value of 0.7 was found to yield sufficient stability while not restricting the time step to severely. Values of the Courant number higher than 1 were found to always lead to instabilities, caused by the explicit first order approximations of the space and surface charges. Additionally, as in some cases the discharge arises to quickly and the Courant number can not guarantee stability, the time step is explicitly limited.

Error monitoring

The solution errors are monitored manually by checking two conditions: the species production and destruction and Gauss' law. It was shown in Equation 3.42 already that the charge weighted sum of the continuity source terms is zero:

$$\frac{\partial n_p}{\partial t} - \frac{\partial n_e}{\partial t} - \frac{\partial n_n}{\partial t} = -\nabla \cdot \vec{\Gamma}_p + \nabla \cdot \vec{\Gamma}_e + \nabla \cdot \vec{\Gamma}_n. \tag{4.45}$$

Of course in numerical modelling, this is never truly zero. Integrating this relation over both the computational volume V and time t:

$$\int_t \int_V \left[\frac{\partial n_p}{\partial t} - \frac{\partial n_e}{\partial t} - \frac{\partial n_n}{\partial t} + \nabla \cdot \vec{\Gamma}_p - \nabla \cdot \vec{\Gamma}_e - \nabla \cdot \vec{\Gamma}_n \right] \mathrm{d}\nu \mathrm{d}\tau = \epsilon_c \tag{4.46}$$

Where ϵ_c is the cumulative numerical error in number of particles created or destroyed, caused by discretization and round-off errors. A similar error can be formulated for Gauss' law:

$$\nabla \cdot \varepsilon \nabla \phi = -\rho, \tag{4.47}$$

For which the error is written as:

$$\int_V \Big[\nabla \cdot \varepsilon \nabla \phi + \rho\Big] \mathrm{d}\nu = \epsilon_g. \tag{4.48}$$

The error physically represents the total charge in coulomb lost by the computational procedure.

Chapter 5

Verification and validation

Verification and validation of the model has been done by using a one dimensional volume discharge set up. This set-up has been used by different authors for simulation of Townsend and glow discharges at atmospheric pressures. The configuration consists of two electrodes separated by a gap of a variable width. This gap is filled with helium at 1 atm pressure. The electrodes are both shielded from the gas by a dielectric layer.

First, code verification will be done. The electric field unit and the species transport units are verified and the order of accuracy of the schemes is tested. Then, the chemical model will be validated using reference data from a paper.

5.1 Verification of the plasma model

In the code verification process, a number of steps will be taken. First, the coupling of the electric field is studied, especially the behaviour of the solution with varying convergence tolerance, the effect of the relative permittivity and that of space charges. Then, implementation of the continuity equations is verified by analysing convergence and accuracy of the schemes. Also, the effect of space and surface charges as well as that of different boundary conditions is demonstrated.

5.1.1 Coupling of the two electric field regions

A dedicated boundary condition was formulated to couple electric fields in the fluid and dielectric regions. A convergence criterion ϵ is a numerical parameter used to set the accuracy of the coupling. The relative permittivity ε_d is a physical parameter and determines the resistivity of the dielectric material. In this subsection, the influence of both parameters is investigated. A maximum value of ϵ is proposed to assure convergence of the electric field in the whole computational domain within one time step. Thereafter, the influence of the relative permittivity on the electric field is studied. Finally, the influence of the charge volume density ρ on the solution of the Poisson equation is investigated. The solution is analysed and the observed order of accuracy of the numerical scheme is checked.

Convergence of the electric field

The normalized coupling residual r_ϕ is tested against a set coupling tolerance ϵ to determine whether the iterative routine is finished, and the solver can continue calculating the species densities. The coupling condition is written as:

$$\hat{n} \cdot (\varepsilon_0 \varepsilon_g E_g - \varepsilon_0 \varepsilon_d E_d) = \sigma. \tag{5.1}$$

The normalized error norm is then written as:

$$r_\phi = \frac{|\varepsilon_0 \varepsilon_g E_g \cdot \hat{n} - \sigma - \varepsilon_0 \varepsilon_d E_d \cdot \hat{n}|}{|\varepsilon_0 \varepsilon_g E_g \cdot \hat{n} - \sigma| + |\varepsilon_0 \varepsilon_d E_d \cdot \hat{n}|} > 0. \tag{5.2}$$

Which tests the current continuity from the gas region $\varepsilon_0 \varepsilon_g E_g \cdot \hat{n} - \sigma$ into the dielectric region $\varepsilon_0 \varepsilon_d E_d \cdot \hat{n}$ over the surface interface. The value is non-zero due to the lagged values in each region simply because the regions are solved sequentially. The iterative routine continues while $r_\phi > \epsilon$. Thus, this criterion influences the smoothness of the electric field properties (electric potential ϕ and field strength $\vec{E}$). The penalty for higher convergence accuracy is the number of required sub-iterations, which can significantly influence the total simulation real time, especially for large meshes. The exact solution of the electric field is known for a relative permittivity of $\varepsilon_d = 1.0$, where the electric field properties should be smooth continuous, as the dielectric material behaves as air and no discontinuities should arise. The test is performed at a voltage of 10kV put on the upper electrode. Thus, the voltage should rise from 0 to 10kV at a slope of 10/50=2kV/mm. The distributions of ϕ and $\vec{E}$ for a range of values of ϵ is given in Figure 5.1.

The values shown are normalised by the exact solution values and represent the solution after 1 time step. It can be concluded that a value of $\epsilon = 1e-3$ already is sufficient for the solution to converge in a single time step. It was checked that the rate of convergence of the solution is independent of the input voltage ϕ_0, which is as expected for a linear system.

Consistency of the coupling should be checked as well: does the solver behave consistently with an increasing number of cells? The consistency of the solver was tested by checking the rate of convergence of the system on two meshes of 200 and 400 cells for a non-relaxed system (i.e. $\alpha = 1$). On the finer mesh, the impact of the relaxation factor is tested by applying a factor of 2. The results are shown in Figure 5.2. Double the number of cells yields double

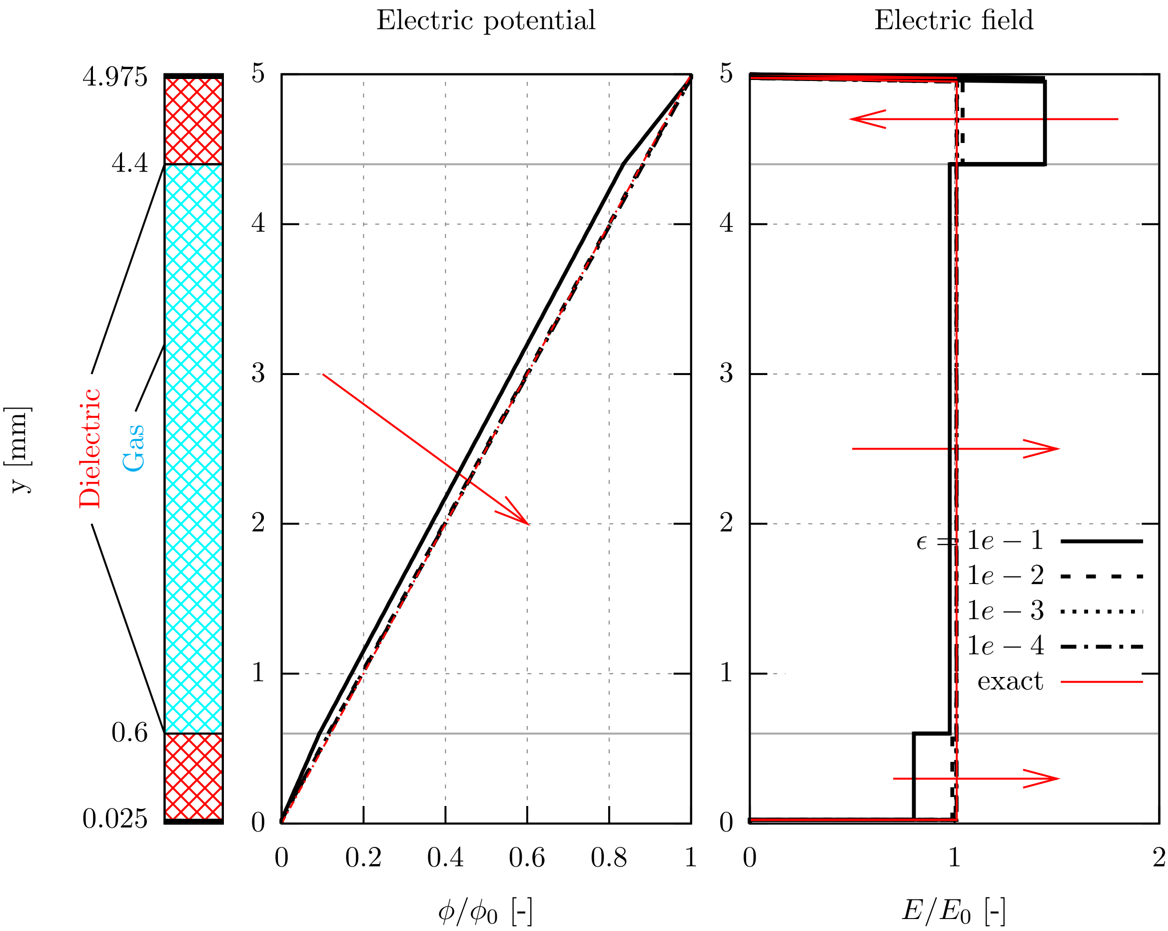

Figure 5.1: Electric potential (**left**) and electric field (**right**) distributions after 1 iteration per convergence criterion. The arrows indicate the direction of convergence with decreasing ϵ (increasing accuracy). The input $\phi_0 = 10kV$, which yields an exact solution of $E_0 = 2kV/mm$. Furthermore, the number of cells $N = 200$ and the relative permittivity $\varepsilon_d = 1.0$.

the number of iterations to achieve the same accuracy, which indicates a first order accuracy. This corresponds to the first order discretization used to formulate the recursive formula for the interface potential. For a mesh with 400 cells, a relaxation factor of 2 reduces the number of iterations by a factor 3.

When the number of cells is increased, the convergence rate decreases, which is typical for an iterative solution method. The rate of convergence varies with the spectral radius of the residual matrix B of the system, which for a Laplacian scheme with Neumann conditions is:

$$\rho(B) = 1 - \mathcal{O}(h^2). \tag{5.3}$$

The spectral radius is a quantification of the diagonal dominance of the matrix, which deter-

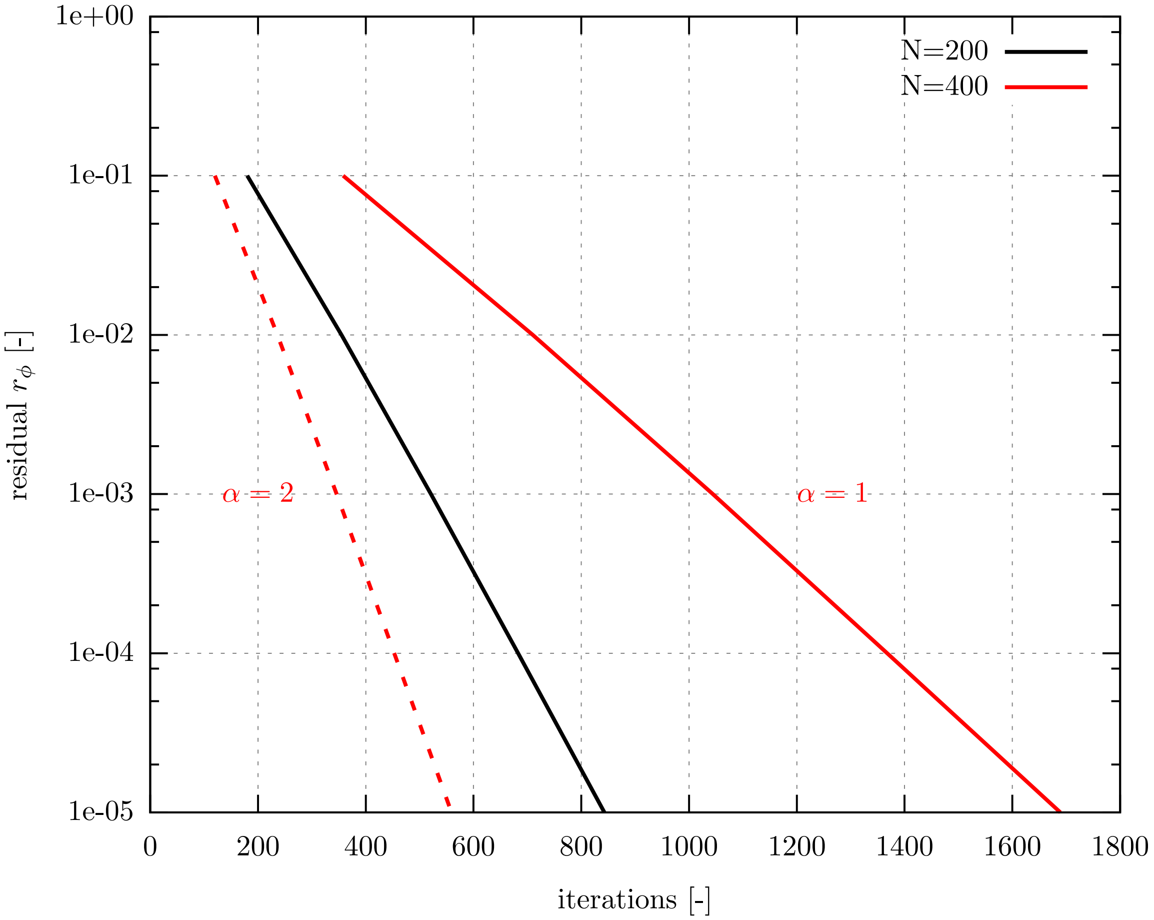

Figure 5.2: Comparison of the convergence behaviour of the region electrostatic coupling for different meshes and relaxation factors. The black line indicates the base convergence without relaxation and 200 cells.

mines the rate of convergence of the system. It can be seen that for $h \to 0$, $\rho(B) \to 1$, and the convergence rate approaches zero. This shows why an increase in cell number leads to an increase in iterations for a given accuracy.

When over-relaxed at the optimum relaxation factor (depending on the largest eigenfunction of the system), the spectral radius is in the order of:

$$\rho(B) = 1 - \mathcal{O}(h). \tag{5.4}$$

This is one order higher and shows that the radius approaches 1 linearly instead of quadratically, explaining the better convergence performance.

Relative permittivity

Next, the influence of the relative permittivity of the dielectric will be evaluated. The variable ε_d is a measure of resistivity of the material, and similarly, the set-up presented in the left column in each picture in this chapter should be seen as an resistor-capacitor (RC) electric circuit. The electrodes function as source, the dielectrics as capacitors and the gas as resistor. The definition of the relative permittivity is given by:

$$\varepsilon_d = \frac{C}{C_0}$$

Where C is the capacitance of the dielectric material relative to a reference capacitance. If ε_d increases, the effective capacitance of the material increases: the resistance, and therefore the electric field strength, drops, and in the limit of $\lim_{\varepsilon_d \to \infty}$, the dielectric behaves as an electrode. The effect on the electric field is demonstrated in Figure 5.3. The same set-up as in the convergence tests is used: an input voltage of 10kV is put on the upper electrode. The grid consists of 200 cells and the relative error criterion is set to $\epsilon = 1e-4$. The results are shown in Figure 5.3.

It can be observed that as the dielectric constant increases, the electric field strength in the dielectric material approaches zero. Consequentially, the electric potential in these regions become constant and, as the total potential energy between the two electrodes should be conserved, the electric field in the gas converges to a finite, non-zero value. Considering the effective gap width reduces from 5 mm to 3.8 mm by a value of $2 \times 0.6 = 1.2$, which means the electric field in the gas region should increase by $5/(5-1.2)$ for $\lim_{\varepsilon_d \to \infty} E(\varepsilon_d)/E(\varepsilon_d = 1) = 5/3.8 \approx 1.32$, which corresponds to the result obtained in the right graph. From this behaviour, it can be concluded that indeed, for increasing values of the dielectric permittivity, the capacitance of the dielectric material increases, its resistance drops and the dielectric starts behaving as an electrode, preserving the electric potential. As a result, a stronger electric field strength is obtained in the gaseous region.

Non-linearity through space charges

In the results presented so far, space charges were always neglected and the potential distributions were always linear. In this section, the effect of these charges will be investigated. Simultaneously, the accuracy of the solution will be tested by assuming a distribution for the space charge and by analytically deriving the solution for ϕ. This is then implemented in the solver by setting initial values of the species densities. By observing the residual norms, the accuracy of the solver can be derived.

Only the gaseous domain is considered: the relative permittivity is chosen high (100) to prevent any potential gradients in the dielectric regions, such that the value of the electric potential on the upper boundary of the fluid domain is equal to the input voltage ϕ_0. The

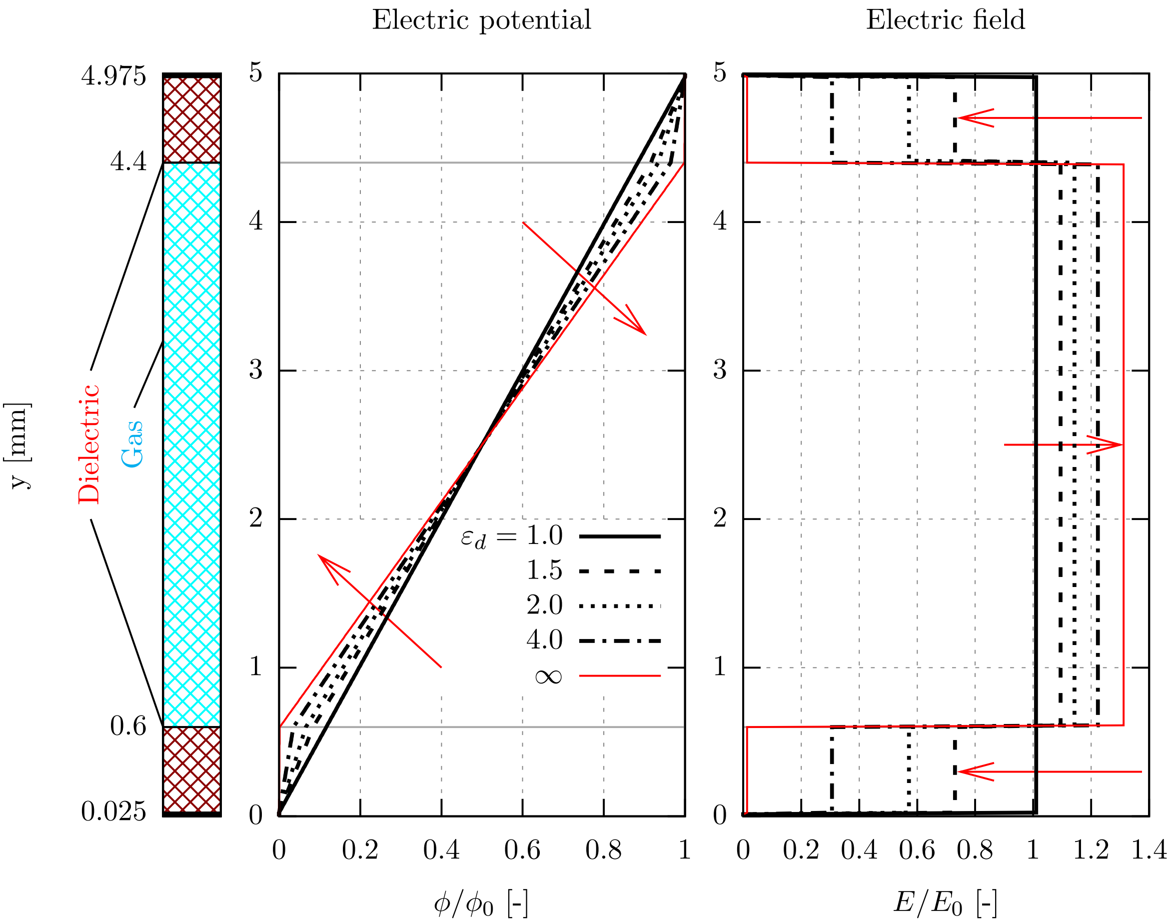

Figure 5.3: Behaviour of the electric field with varying permittivity. The arrows indicate direction of convergence for increasing values of ε_d. The reference values $\phi_0 = 10kV$ and $E_0 = 2kV/mm$. The number of cells $N = 200$.

charge volume density ρ will be varied periodically over the domain, i.e.:

$$\rho = e(n_p - n_e - n_n) = eA\sin(\frac{2\pi}{H}y). \tag{5.5}$$

Assuming the permittivity is constant throughout the domain, the one-dimensional Poisson equation becomes:

$$\varepsilon\frac{\partial^2\phi}{\partial y^2} = -eA\sin(\frac{2\pi}{H}y). \tag{5.6}$$

A is chosen according to a suitable value. The order of magnitude of the LHS is $\varepsilon\phi_0/eH^2$, where $0 \leq y \leq H$ and H is the gas region domain height. The factor with which this order varies is chosen to be 10. A then has to be $A = \frac{10\varepsilon\phi_0}{eH^2}$. Next, the equation is integrated over y:

$$\varepsilon\frac{\partial\phi}{\partial y} = -\varepsilon\vec{E} = eA\frac{H}{2\pi}\cos(\frac{2\pi}{H}y) + B. \tag{5.7}$$

Integrating this relation again over y:

$$\varepsilon\phi = eA\frac{H^2}{4\pi^2}\sin(\frac{2\pi}{H}y) + By + C. \tag{5.8}$$

With boundary conditions $\phi(y = 0) = 0$ and $\phi(y = H) = \phi_0$. This relation for ϕ is the exact solution for the potential in the gas domain. Please note that A is already known. Evaluating at $y = 0$ yields $C = 0$ and $y = H$ yields $B = \varepsilon\phi_0/H$. The exact relation for ϕ in this problem is then given by:

$$\phi = \frac{10}{4\pi^2}\phi_0\sin(2\pi\frac{y}{H}) + \frac{y}{H}\phi_0. \tag{5.9}$$

And following the corresponding relation for the electric field:

$$\vec{E} = -\frac{10}{2\pi}E_0\cos(2\pi\frac{y}{H}) - E_0. \tag{5.10}$$

Where $E_0 = \phi_0/H$. The exact solution is shown in Figure 5.4, together with the numerical solution obtained from the solver.

Now a manufactured solution is obtained, mesh consistency can be checked as well. According to Roy (2005), consistency is measured by observing the discretization error. The Laplacian scheme is second order in space, although this order is not necessarily obtained in practice. It is necessary to evaluate the obtained order of accuracy by the solver. This is done through inspection of the behaviour of the solution by varying the spatial resolution, i.e. Δx. The observed order of accuracy p can then be found by dividing the residual norms for two different mesh sizes by the ratio of their seizes:

$$p = \frac{\ln(L_k/L_{k+1})}{ln(r)}. \tag{5.11}$$

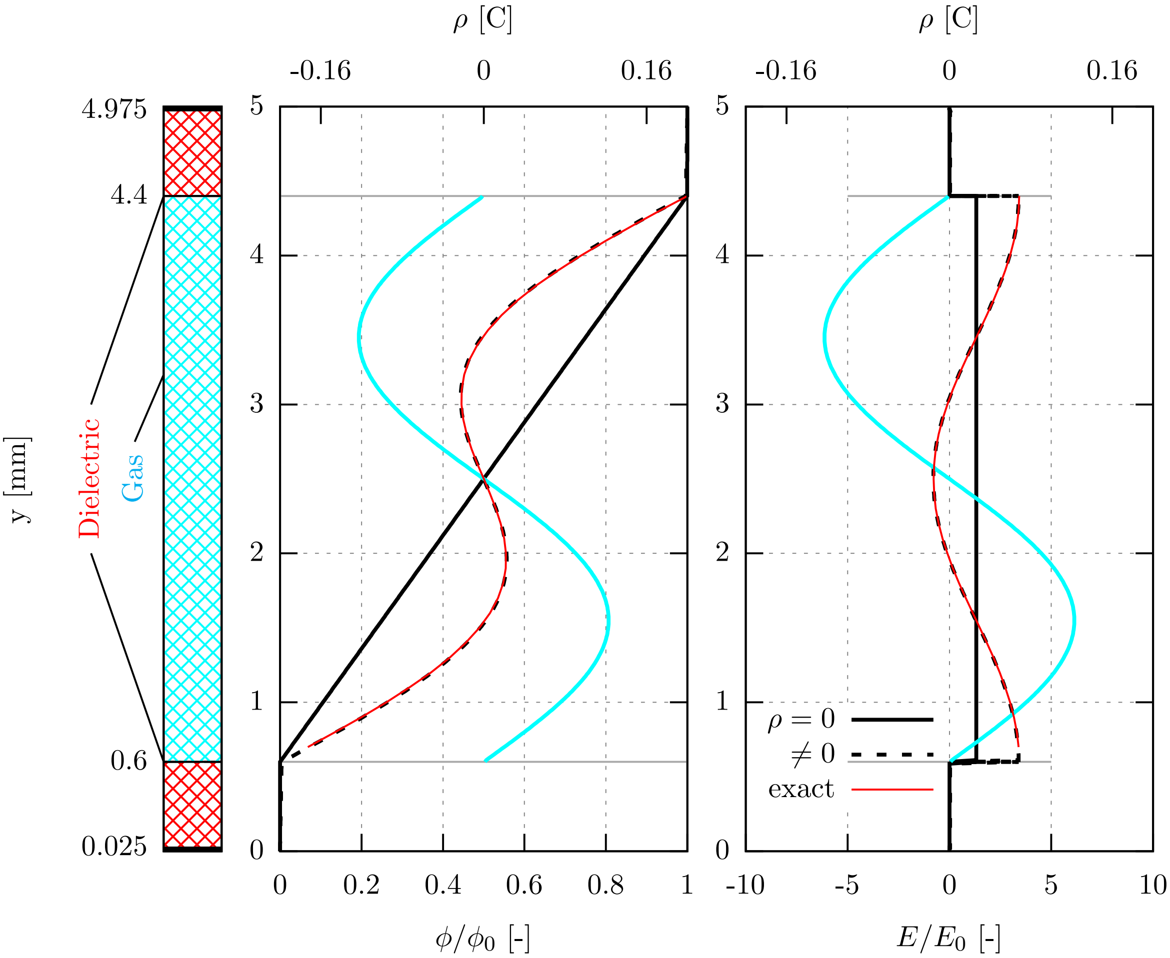

Figure 5.4: The exact and numerical solutions of ϕ **left** and $\vec{E}$ **right** to a sinusoidal charge volume density distribution ρ_c at an input voltage $\phi_0 = 10$kV and reference $E_0 = 2kV/mm$. The solution to the homogeneous Laplace for this problem is given for comparison.

The norm L_k for mesh k of size $h_k = \Delta x_k / \Delta x_0 = r h_{k+1}$ can be computed by using either of the following norms Roy (2005):

$$L_1 = \frac{\sum_j^N |f_j - f_j^*|}{N}, \tag{5.12}$$

$$L_2 = \sqrt{\frac{\sum_j^N |f_j - f_j^*|^2}{N}}, \tag{5.13}$$

$$L_\infty = \max |f_j - f_j^*|. \tag{5.14}$$

Where N is the number of cells in the mesh and f_j is the solution of the PDE in cell j. These norms are therefore residual norms and are a measure of how well the linear system approaches the exact solution. The result of the performance of the solver on different meshes for the manufactured problem with sinusoidal charge volume density is presented in Figure 5.5.

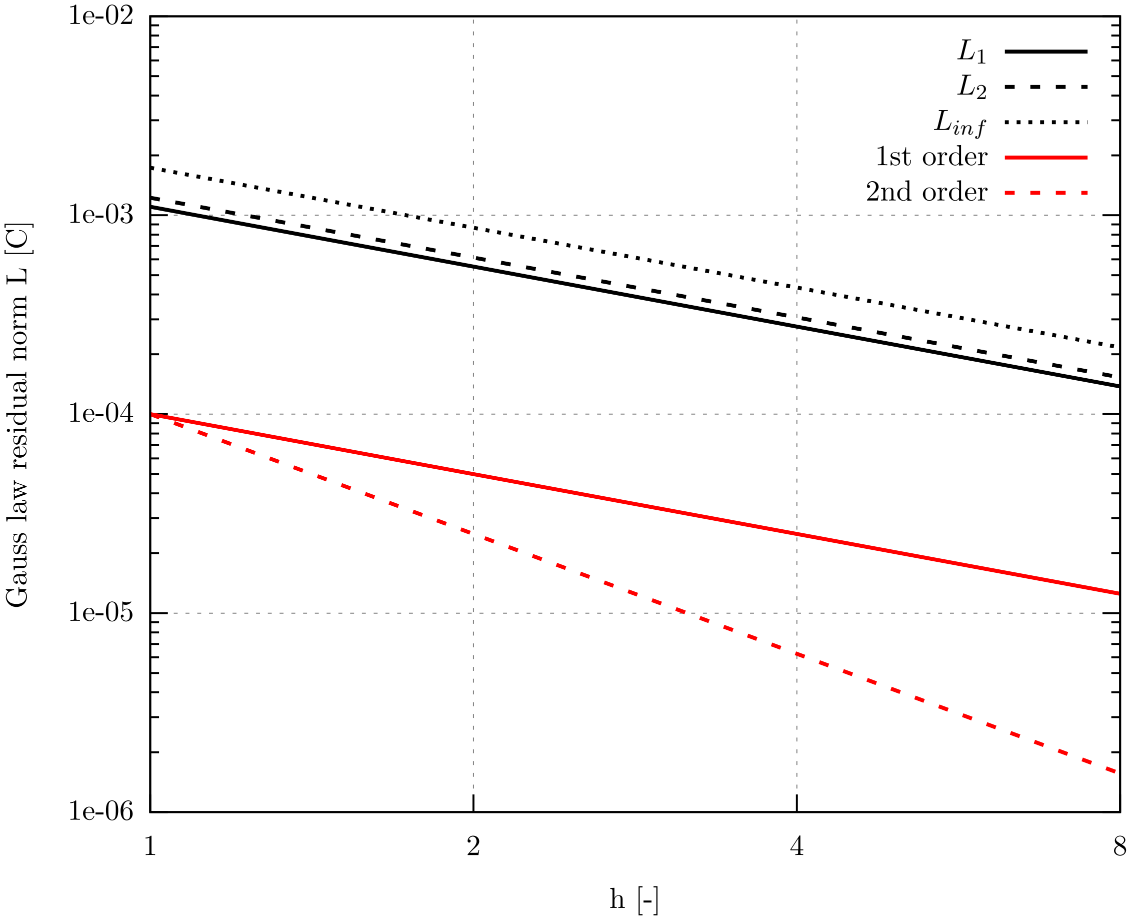

Figure 5.5: Presentation of mesh convergence of the Poisson equation for the electrostatic potential ϕ using the manufactured solution for space charge ρ. First and second order slopes are included for comparison. The Laplacian scheme was found to be only first order accurate.

The curves shown in Figure 5.5 correspond to a first order scheme. This is unexpected, as any Laplacian numerical scheme should be second order. On the other hand, a coupling condition is used which is only first order accurate, which would explain why no higher order is achieved. The first order at least proves convergence of the system.

5.1.2 Transport of species

The next unit to be tested is the transport species continuity model, which comprises drift and diffusion of the species. In this section, particles can neither be created nor destroyed, yielding the homogeneous continuity equations. The general behaviour of species over time will be visualized, as well as the influence of different boundary conditions and the effect of taking into account thermal velocity for these conditions. Finally, the influence of surface charge and space charge on the electric field, and therefore also on the transport of species, will be looked into.

First, a simple transport case is shown. An initial neutral plasma is assumed with a density of 10^{16} for both the electrons and the positive ions. Zero flux boundary conditions are imposed, so all initial species are contained within the computational domain. No space or surface charges are applied, i.e. the electric field is not distorted in any way and has a linear distribution similar to the distributions shown in Figure 5.3. Furthermore, $\epsilon = 1e - 4$ and $\varepsilon_d = 5$.

For spatial discretization a MUSCL scheme has been used. A backward Euler scheme was used for integration in time. The properties of these schemes will be evaluated later in this section. Two cases are represented, one with an input voltage of 1kV and one at 250kV. The results at three different time steps are displayed in Figure 5.6.

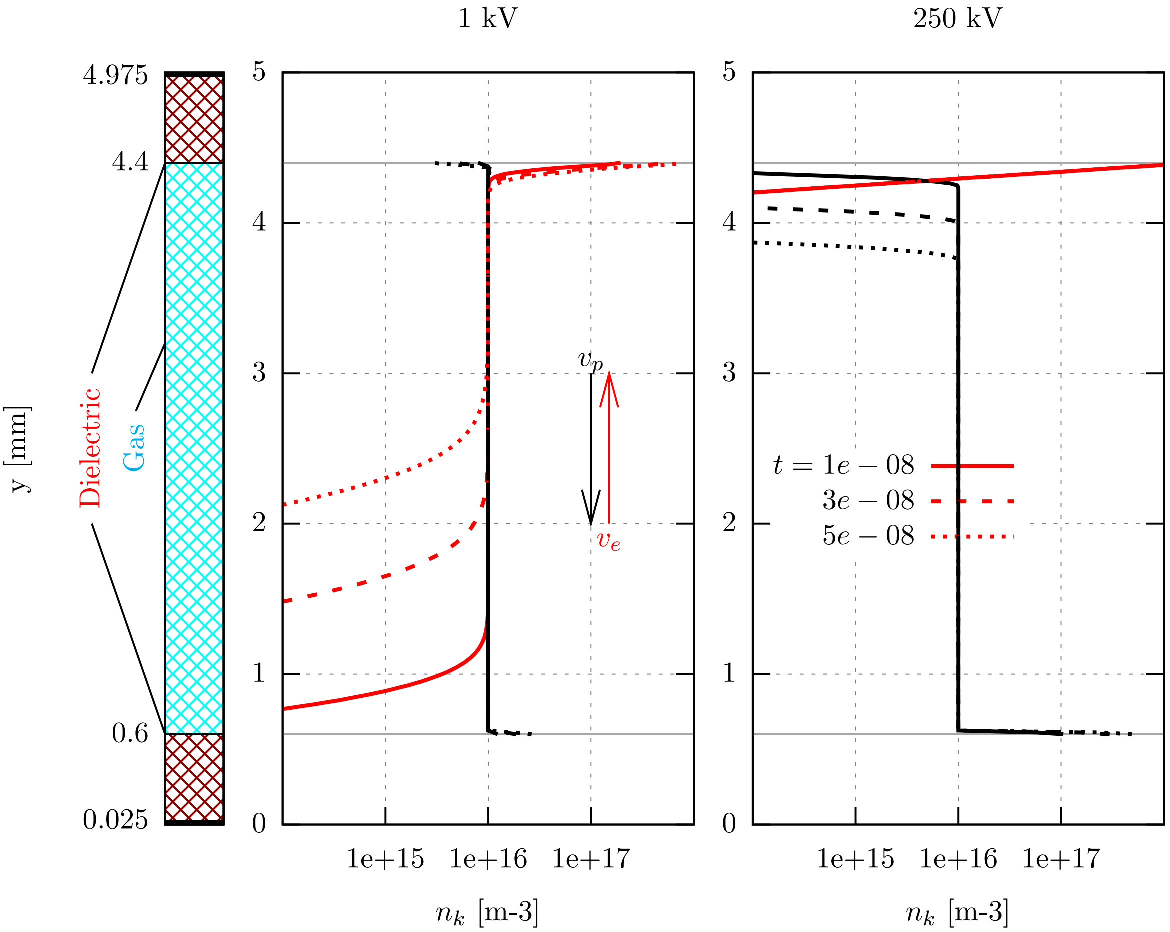

Figure 5.6: Temporal variations in species distributions for $\epsilon = 1e - 4$, $\varepsilon_d = 5$. The red line represents the **electrons**, while the black line indicates the **positive ion** distributions.

At an input voltage of 1kV at the upper electrode, the electric field has a negative value in the current reference frame (positive upward) and positive ions are forced downwards to the ground electrode. The direction of the species transport is indicated by the two arrows in the figure. As the mobility of the positive ions is not high enough though, the heavy particles hardly move and only some change can be spotted at the dielectric boundaries. The electron mobility is significantly higher, and transport of this species is clearly visible. As the electric field strength is constant throughout the whole domain, all particles have the same velocity and a wave forms at the lower dielectric. The electrons accumulate on the upper dielectric, where the concentration quickly rises. It was checked that the average density in the domain remains 10^{16}, which confirms that indeed no species are lost or created.

To demonstrate the effect of this difference in order of magnitude of the species mobilities, a voltage of 250kV is applied. The positive ion mobility is a function of the electric field and has its peak at 2.5 V/(mm Torr). The mobility reduces for higher electric field values. So in order to match the electron velocity, the voltage potential has to be exponentially increased. For now, the voltage is just set to 250kV to show that the ions are transported in a similar way.

Accuracy of the discretization schemes

The convection-diffusion problem which is dealt with in this work is a well known one, applicable to many other areas than plasma modelling. To investigate whether the solver behaves appropriately, a manufactured solution will be introduced again, for which the accuracy of the MUSCL spatial scheme and the Euler temporal scheme can be determined. The MUSCL scheme is second order accurate in smooth regions, but tends to behave as a first order scheme near discontinuities. In this case, the velocity and diffusion coefficient are assumed to be constant.

$$\frac{\partial n_k}{\partial t} + u_k \frac{\partial n_k}{\partial x} - D_k \frac{\partial^2 n_k}{\partial x^2} = 0. \tag{5.15}$$

The following solution is assumed for the number density of species k:

$$n_k(y,t) = A \sin^2(\frac{2\pi}{H} y) \sin^2(\frac{\pi}{T} t). \tag{5.16}$$

With initial conditions $n_k(y,0) = 0$ and boundary conditions $\frac{\partial n_k}{\partial t}(t,0) = \frac{\partial n_k}{\partial t}(t,H) = 0$. The constant A has a value of $A = n_0 = 10^{16}$ to simultaneously investigate the behaviour of the schemes at high gradients.

Taking the first derivative in time and the first and second derivatives in space yields:

$$\frac{\partial n_k}{\partial t} = \frac{2\pi}{T} A \sin^2(\frac{2\pi}{H} y) \sin(\frac{\pi}{T} t) \cos(\frac{\pi}{T} t), \tag{5.17}$$

$$\frac{\partial n_k}{\partial y} = \frac{4\pi}{H} A \sin(\frac{2\pi}{H} y) \cos(\frac{2\pi}{H} y) \sin^2(\frac{\pi}{T} t), \tag{5.18}$$

$$\frac{\partial^2 n_k}{\partial y^2} = \frac{8\pi^2}{H^2} A (\cos(\frac{4\pi}{H} y) \sin^2(\frac{\pi}{T} t). \tag{5.19}$$

Substituting into the convection-diffusion equation gives:

$$\begin{aligned} \frac{\partial n_k}{\partial t} + u_k \frac{\partial n_k}{\partial x} - D_k \frac{\partial^2 n_k}{\partial x^2} = n_0 \sin^2(\frac{\pi}{T} t) \Big[& \frac{2\pi}{T} \sin^2(\frac{2\pi}{H} y) \frac{\cos(\frac{\pi}{T} t)}{\sin(\frac{\pi}{T} t)} \\ & + u_k \frac{4\pi}{H} \sin(\frac{2\pi}{H} y) \cos(\frac{2\pi}{H} y) \\ & - D_k \frac{8\pi^2}{H^2} (\cos(\frac{4\pi}{H} y) \Big]. \end{aligned} \tag{5.20}$$

This equation is implemented for the electron species and solved over a simulation time T at an input voltage of 10kV. At this voltage, the electrons have velocities of $u_e = 264808$m/s. T is then computed as $H/u_e = 1.43e-8\text{s}$. To get the combined order of magnitude, both the time step and the cell size are reduced. The definition of the size factor h is then $\Delta x \Delta t / \Delta x_0 \Delta t_0$. The result is shown in Figure 5.7.

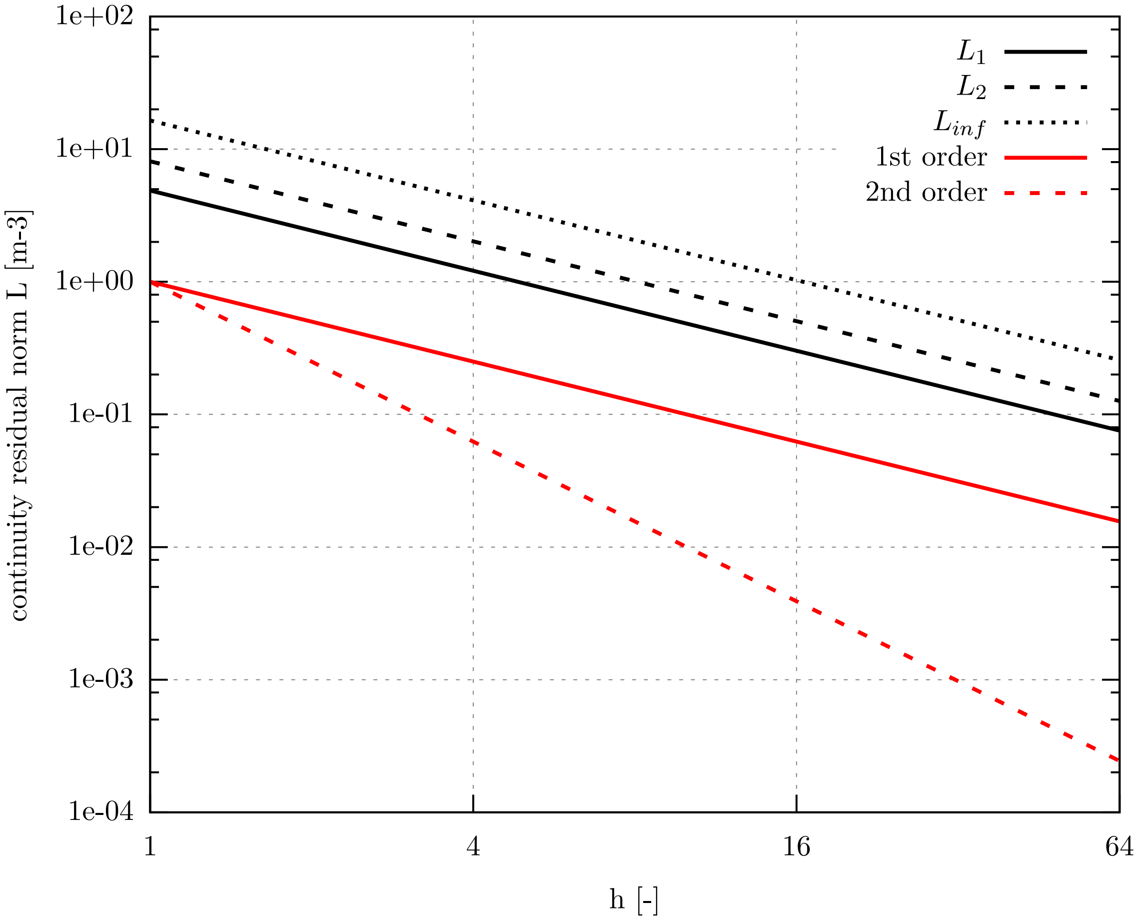

Figure 5.7: Comparison of the residual norm behaviour of the transport equations with a MUSCL spatial scheme and a forward Euler temporal scheme. The x axis indicates the temporal and spatial refinement factor. First and second order slopes are included for comparison.

It can be seen that the observed order of accuracy is 1. The backward Euler scheme (second order) was tested as well in combination with the MUSCL scheme, and also only yielded a first order accuracy. This is due to the nature of the truncation error, which is of an order equal to the sum of the truncation errors of the individual terms:

$$\text{Truncation error } = \mathcal{O}(\Delta t^p) + \mathcal{O}(\Delta x^q). \tag{5.21}$$

p and q denote the orders of the temporal and spatial schemes, respectively. Formally, the MUSCL scheme is second order. In this model problem though, the MUSCL scheme behaves as a first order scheme. As the number densities are of very high orders, so are the gradients yielding gradient ratios $r \ll 1$ (used to determine the slope limiter), indicating low scheme resolution as the first order Godunov scheme is approached. To get a second order accuracy using the presented analysis, the scheme should behave second order throughout the whole domain, which is simply never the case when computing number densities. Concluding, the net order of magnitude of the solution is then also first order.

Non-linearity through space and surface charges

As explained in subsection 5.1.1, non-linearities are imposed on the solution of the Poisson equation for the electrostatic potential. This in turn alters the plasma transport characteristics, imposing non-linear effects on the solutions of the continuity equations as well. The severity of this feedback will be investigated, and the effect for pure transport (no source terms considered) will be demonstrated. Whereas earlier on only Gauss' law was considered, the surface charge remained constant. Now, as species are also transported towards the surfaces, the net surface charge becomes a function of time, altering the potential on the fluid-dielectric interfaces.

The effect is shown in Figure 5.8. The same geometry has been taken as in the former section, with an applied voltage of 1kV and a dielectric permittivity of 9. Outflow conditions are specified, as otherwise surface charging would not occur. Also the initial species densities are taken one order higher to increase the observed effects. In the figure, four trends are depicted. The left graph shows the result when the surface charge is not considered ($\sigma = 0$), while in the right graph surface charges are considered($\sigma \neq 0$). In both graphs, the gray trends indicate the volume charge is neglected ($\rho = 0$), while the coloured trends indicate the volume charge is not neglected ($\rho \neq 0$).

Non-symmetric, non-linear effects arise as the electrons are transported towards the anode and a region of positively charged ions remains. The non-zero space charges allows for wave steepening, as the electric field upstream of the species density wave is intensified, while the electric field downstream is quenched. Furthermore, the upper surface is charged negatively, while the lower dielectric surface is positively charged, although due to the low ion mobilities, this charging is only marginal. Still, this drives the voltage difference down, quenching the electric field and reducing the movement of charged species.

When comparing the gray curves with the coloured curves, it can be concluded that the space charges alter the species velocities locally, creating discontinuities in the density fields. Comparing the left graph to the right, quenching of the electric field by surface charge built-up becomes evident.

It is added that the initial species densities are of severe influence on the observed effects. This can also be concluded when analysing Gauss' law:

$$\nabla \cdot \varepsilon \nabla \phi = -\rho, \tag{5.22}$$

by the order of magnitudes of its variables. Using the fact that $\varepsilon = \mathcal{O}(\varepsilon_0)$, $\phi = \mathcal{O}(\phi)$, $\nabla = \mathcal{O}(d)$ where d is the gap spacing, and $\rho = \mathcal{O}(en_0)$:

$$\frac{\mathcal{O}(\varepsilon_0)\mathcal{O}(\phi)}{\mathcal{O}(d^2)} = \mathcal{O}(en_0). \tag{5.23}$$

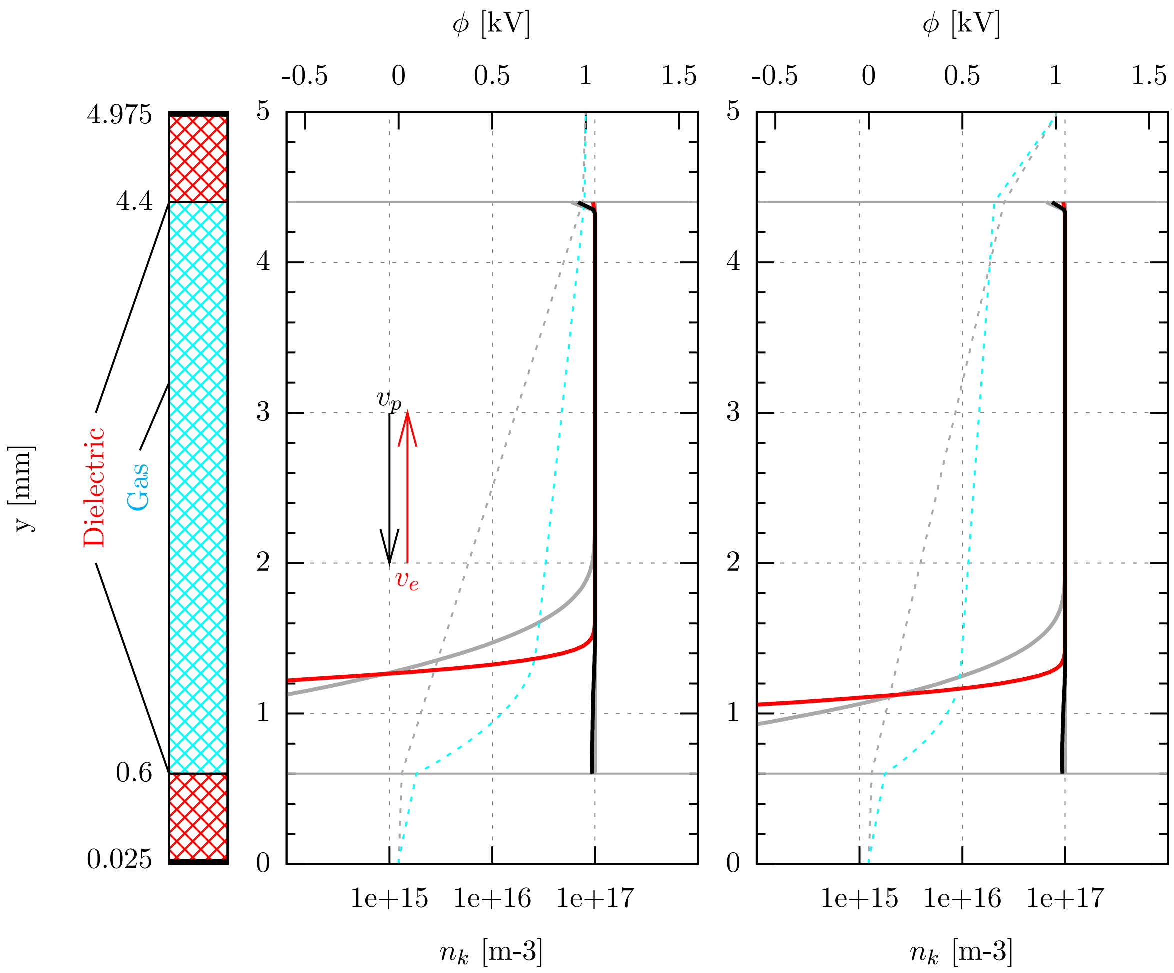

Figure 5.8: Non-linear effects of the charge densities on the electric field potential ϕ and density distributions for **electrons** and **positive ions** for $\sigma = 0$ (left) and $\sigma \neq 0$ (right), $\varepsilon_d = 9$.

The order of magnitude of the induced potential by space charges is then:

$$\phi = \mathcal{O}(\frac{en_0d^2}{\varepsilon_0}). \tag{5.24}$$

This analysis is only valid for the homogeneous transport model. When the chemical model is activated, ρ is determined by the discharge characteristics. The initial charge density is then also expected to be of less influence.

Additionally, the effect of the thermal velocity is examined. In some work, this component is ignored. When examining the order of magnitude of the component, the following can be concluded. For an electron elementary charge $e = \mathcal{O}(10^{-19})$c, temperature of $\mathcal{O}(1)$eV and mass of $\mathcal{O}(10^{-30})$kg, this velocity is in the order of $e = \mathcal{O}(1e - 5.5)$m/s. As shown in subsection 5.1.2, for voltages in the order of $V = \mathcal{O}(1)$kV, the velocity of electrons is in the order of $u_e = \mathcal{O}(10^4)$m/s. This means that in a convection dominated problem, the thermal velocity component at the boundary is dominant by 1.5 orders of magnitude. Especially considering the fact that this velocity is constant, this can have great implications on the simulation results.

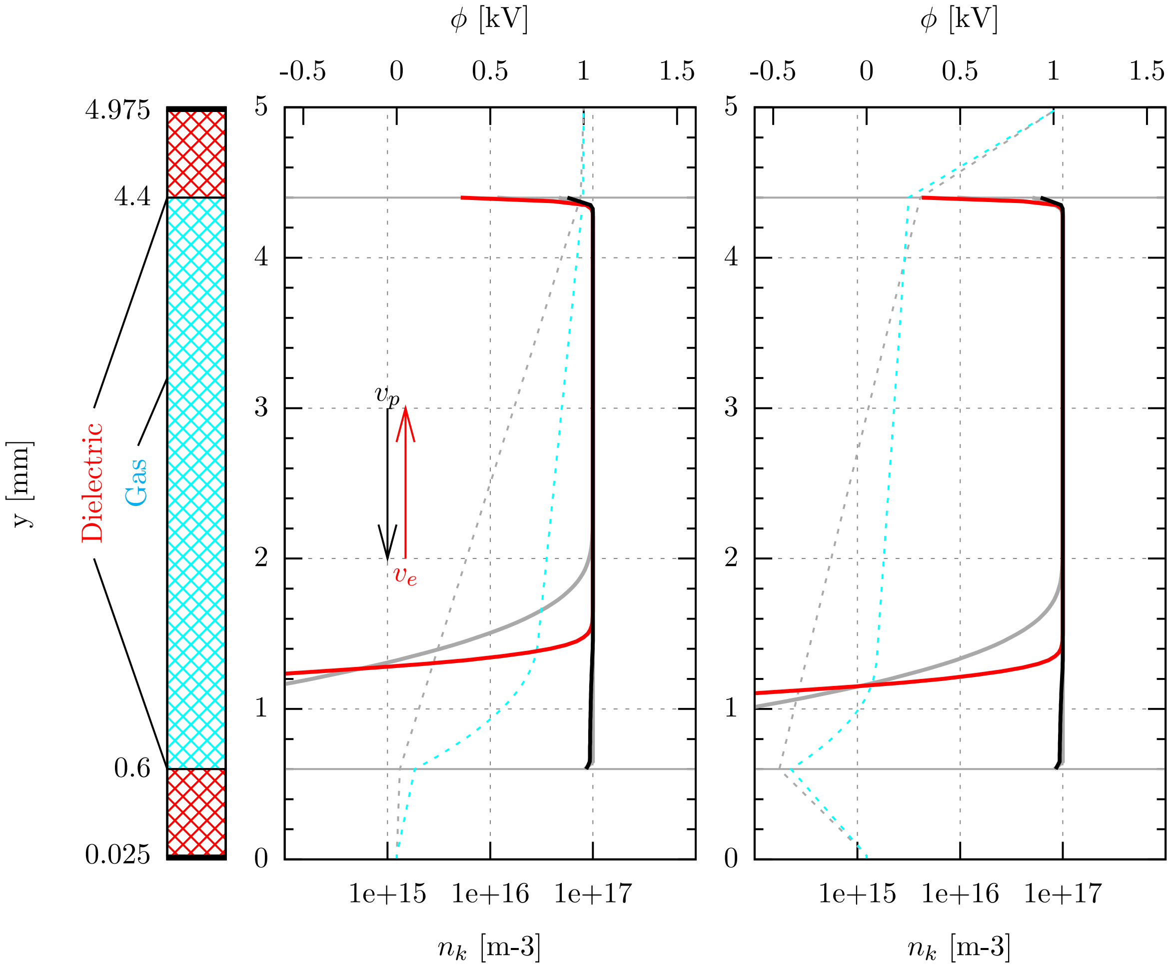

Figure 5.9: Effects of the thermal velocity on the electric field potential ϕ and density distributions for **electrons** and **positive ions** for $\sigma = 0$ (left) and $\sigma \neq 0$ (right), with $\varepsilon_d = 9$.

This can be observed in Figure 5.9. While even for a short period, the electron thermal velocity still dominates the species flux towards the cathode, which is sufficient to negatively charge the lower dielectric surface. It can be imagined that in the case of zero particle production, the influences are not so severe, and the major effect of the thermal velocity is found in a negative overall shift of the potential distribution. In actual discharge simulation, significant asymmetric peaks can arise in the particle densities, close to the dielectric surfaces. Negligence of the thermal velocity component as then ill advised, as strong asymmetric effects then may arise, which have not become clear in the given verification cases.

Concluding, neglect of the thermal velocity is not supported in this work. In ns-DBD, electrons reach velocities up to several 10^6 m/s. In this case, neglecting the thermal velocity is acceptable. For the voltages used here, ignoring the thermal velocity is not a valid assumption.

Comparison of different flux boundary conditions

Two sets of flux boundary conditions were discussed in section 3.3. The effect of the thermal velocity component was treated above. Here, the difference between the more popular conditions proposed in Boeuf et al. (2009) are compared to the physically more accurate conditions proposed by Hagelaar et al. (2000). The main difference between the two sets of conditions is disposal of the diffusion term in the first, and separate treatment of the surface emitted γ-electrons in the second.

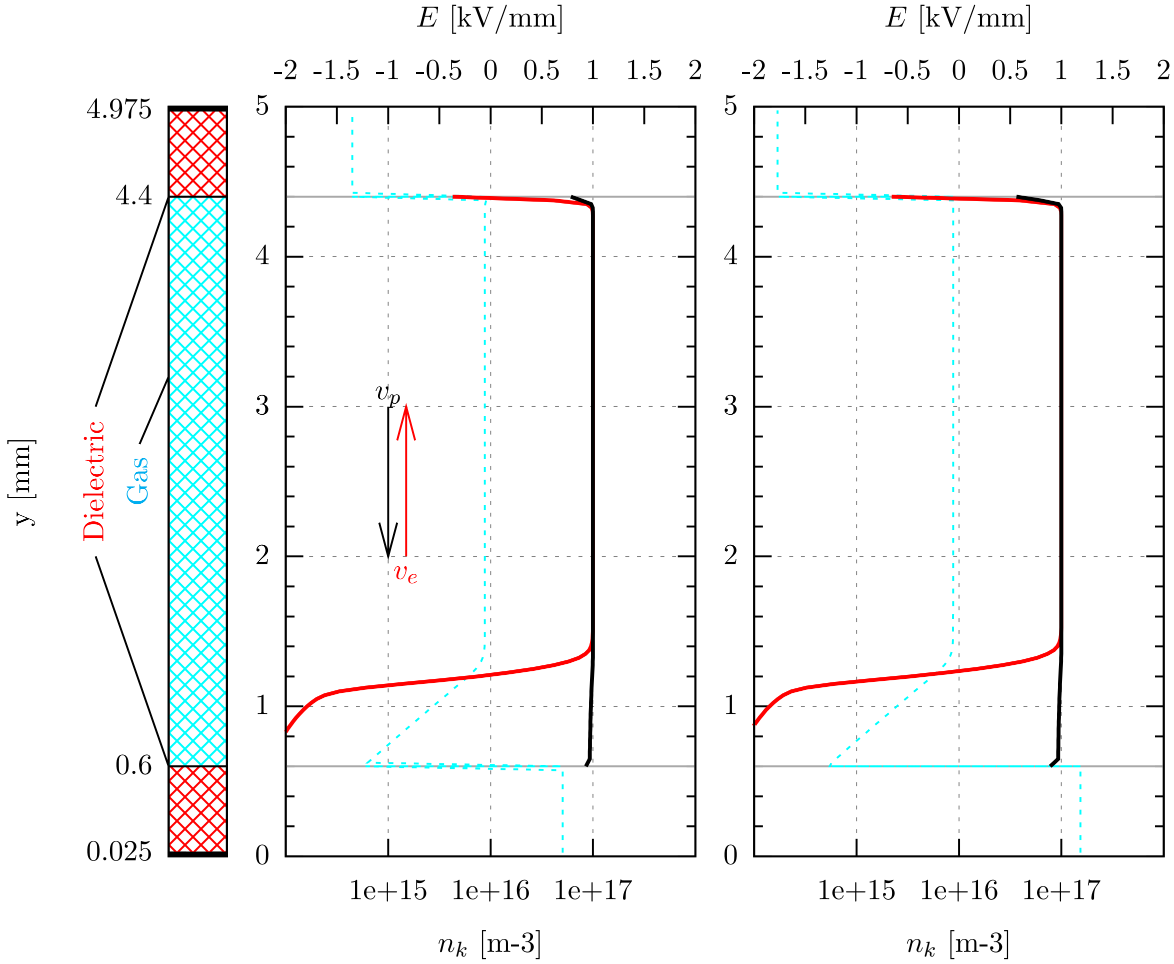

Figure 5.10: Comparison data of the boundary conditions physical effects for the electric field strength E and density distributions for **electrons** and **positive ions** at an input $\phi = 1$kV and permittivity of $\varepsilon_d = 9$. Furthermore, space and surface charges, thermal velocity and secondary electrons are all enabled, with $\gamma = 0.2$.

In Figure 5.10, the two sets of conditions are compared against each other. Thermal velocity is considered, as well as a secondary electron flux of $\gamma = 0.2$. The differences are not very clear, and so it can be assumed that the assumptions made in Boeuf et al. (2009) are valid. It is added, though, that Hagelaar et al. (2000) reported strong differences, especially in the effective γ observed when treating the γ-electrons separately. It is possible this difference only arises when the chemical model is included, and secondary electron emissions affect the breakdown voltage. This should be investigated, but is left for future work.

5.2 Validation of the plasma model

The model is validated against a case presented by Massines et al. (1998), which comprises the same geometric 1D set-up as shown before, just with slightly different parameters. The case represents a cathode-fall glow discharge.

In their paper, the model is described as follows. Two parallel electrodes were used, both covered by an alumina layer separated at $d = 5$mm, with a diameter of 40mm and a reference area of 1256mm^2, a dielectric thickness of 0.6mm and a capacitance of 70pF. According to the relation for capacitance:

$$C = \frac{\varepsilon_d \varepsilon_0 A}{d}, \tag{5.25}$$

This implies that the plates have a dielectric permittivity of 31.47. In the equation above, A is the surface area of the dielectric plates and d is the gap spacing. An uncertainty arises here, as alumina is known to have a dielectric permittivity of about 9. The explicit value used in this paper is not mentioned, so the dielectric capacitance is matched by using a value of 31.47.

The reaction rate and mobility coefficients of the He-0.5%Ar mixture presented in subsection 4.4.1 are used. Helium and argon are noble gases and their plasma consists of (positive) atomic helium and electrons only. The secondary electron emission coefficient $\gamma = 0.05$.

The validation model also has a gap spacing of 5mm, while the dielectric plates have a thickness of 0.575mm each. With each electrode having a thickness of 0.025mm, the whole computational domain has a height of 6.2mm. The plates have a reference area of 1.25mm^2, which means the results will be scaled to fit the dimensions of the reference data. The mesh is uniform and consists of 200x1x1 square cells, with a cell dimension of 12.5μm.

The presented data is the input voltage, output current, memory voltage and the gap voltage. The output current shown is the spatially averaged conduction current:

$$J_{out} = \frac{1}{h}\int_h J_{cond}\mathrm{d}y = \frac{1}{h}\int_h e(U_p n_p - U_e n_e)\mathrm{d}y \tag{5.26}$$

The memory voltage is the potential measured on the dielectric surface (at the anode side of the domain), and is a measure of the charge stored by the surface charging. This potential is directly measured by the solver. According to Massines et al. (1998), the gap voltage for a 1D geometry can then be calculated through:

$$V(t)_{gap} = V(t)_{applied} - V(t)_{memory}. \tag{5.27}$$

The results in the work of Massines et al. (1998) are shown in Figure 5.11 and Figure 5.13, where the latter is a spatial distribution of the species densities and electric field values at the time of maximum current in the first. As the discharge develops, the voltage remains constant at first, and the decrease in resistivity leads to a proportional increase in current. Then, the current is at its peak and starts to drop. This is due to quenching of the electric field as positive ions charge the dielectric surface on the anode side. The voltage and current in the gap are balanced through:

$$U = IR, \tag{5.28}$$

And as the resistance of the plasma R remains constant, the voltage drops along with the current. The dielectric continues to charge, until the discharge current is completely terminated. The process repeats every half cycle of the actuation period.

The data obtained in this work shows comparative, but different results. First of all, not one but two peaks arise per half cycle. Even though these peaks are in the order of magnitude of the reference data, they are not as strong. This results in the fact that the development of the plasma is not as strong, which is supported by the results shown in Figure 5.14. The particle densities were found to be a factor 2.5 lower than the ones presented in Figure 5.13. The dielectric surface is not charged sufficiently, which can be observed by the lower values of the memory voltage. Consequently, the gap voltage is too high. Another consequence is the remaining surface potential after the first discharge, which creates a sufficient potential difference with the still rising input voltage. This allows for a second discharge, which is slightly weaker than the first. The input voltage decays, and the current is terminated, thereby also keeping the memory voltage constant.

Polarization was observed, as a net charge builds up during a cycle. On average, a charge of 512 V was built-up until 500μs, which corresponds to 0.214 C/cm^2. The voltage curves have been corrected according to this value. This was also reported in the paper, although no explicit values were given. This charge built-up can be explained by the in general higher densities of the positive ions during the discharge peaks, which charge the dielectric surfaces.

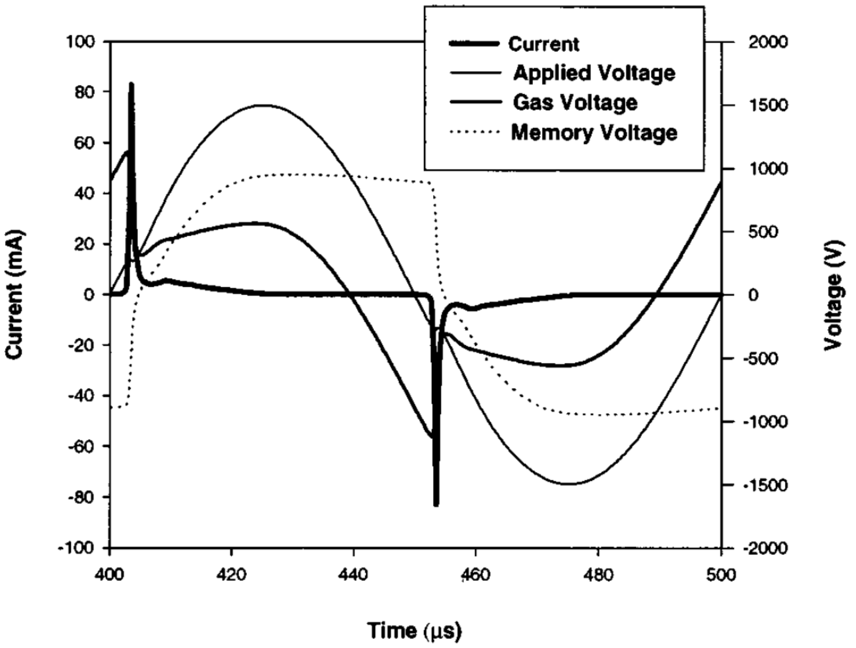

Figure 5.11: Simulation results as presented by Massines et al. (1998). Depicted is one period of oscillation at 1500V amplitude at 10kHz. During discharge, at the current peak, the dielectric surface is positively charged, increasing the potential until the electric field is quenched. The gap voltage first drops, after which it moves along with the input voltage until the next discharge.

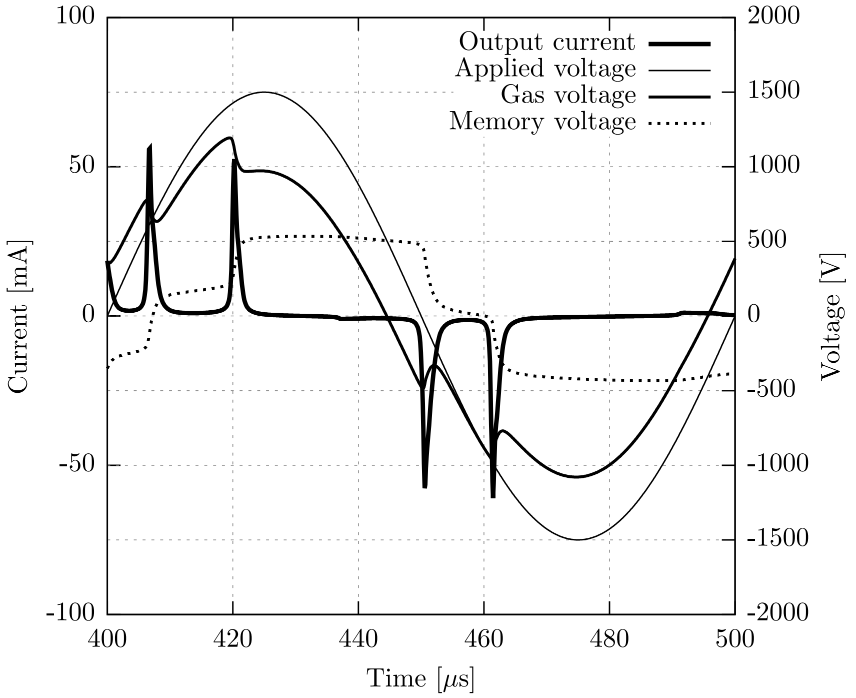

Figure 5.12: Temporal distribution results obtained with the solver.

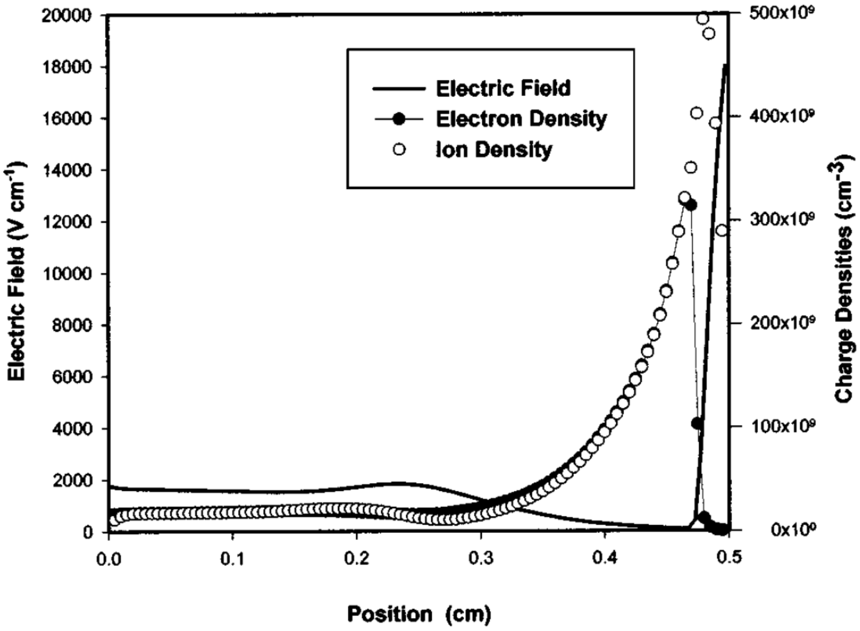

Figure 5.13: Spatial distributions of the electric field and the species densities obtained from the work of Massines et al. (1998). The anode is on the left, while the cathode is on the right.

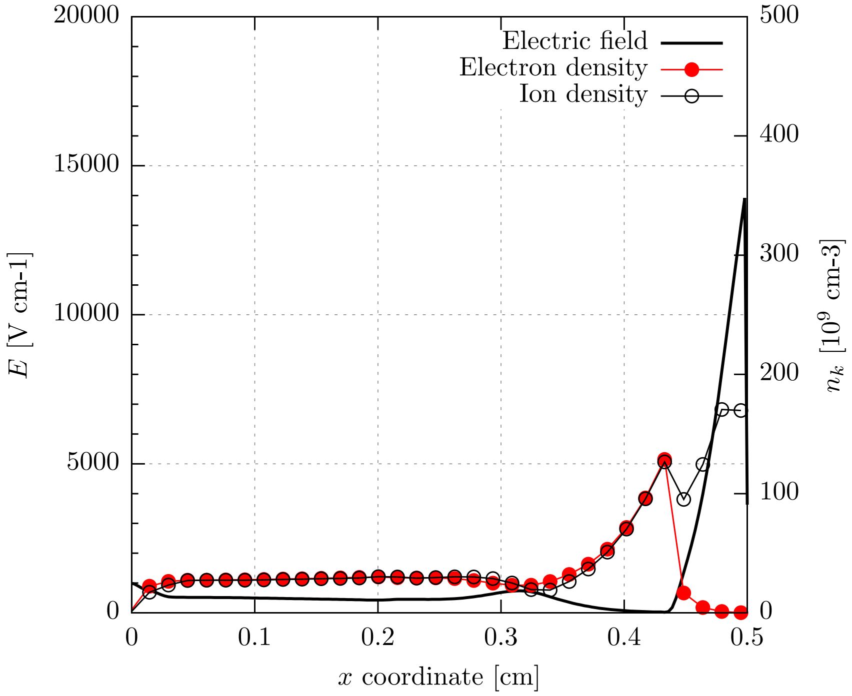

Figure 5.14: Spatial distribution results obtained with the solver.

During validation of this model, a lot of uncertainty arose in terms of the chemical model and parameters such as the secondary electron emission coefficient γ and the dielectric permittivity ε_d. This makes quantitative comparison very difficult, as can be seen from the difference in values. On the other hand, the order of magnitudes of the result align, as well as the trend of the distributions. It can be concluded that the model shows the appropriate behaviour. To give full guarantee, the model should be validated against, preferably self-conducted, experiments. This is left for future work.

5.3 Notes on the verification and validation process

In this chapter, code verification was applied to prove the correctness of the implementation of the solver. First order accuracy was observed for the Laplacian scheme as well as the temporal and convective scheme. With this, convergence of the solution has been demonstrated.

The physical effects of the space and surface charges, as well as those of the different boundary conditions, have been tested, all of which showed physical behaviour, plausible at the least. The effect of the thermal velocity, which often is neglected in reference work, was studied. The influence of the thermal velocity at medium voltages ($\mathcal{O}(10^3)$) was found to be of too much an impact, to be neglected. What hasn't been studied, though, is whether this assumption would actually yield physically preciser results. This has also been a major source of unclarity during validation, as the boundary conditions are not clarified in the paper.

The capability of the solver has been demonstrated by reproducing a cathode-fall glow discharge in a volumetric set-up. Quantitatively, full correspondence with a reference case could not be achieved. As the basis of the solver, the units responsible for the electric field and species transports, was verified, the discrepancies are sought in misinterpretation of the chemical model and the physical parameters presented by Massines et al. (1998). This does not necessarily mean the last unit has been implemented wrongly, but to give full disclosure, the model should be validated against in-house experimental data. This was aimed for in this work, as suitable experiments were performed at EPFL, but the data was not yet ready for publication.

During testing, most parts of the solver, such as the predictor-corrector scheme and its convergence criteria, were found to be successfully implemented. How successful, though, has not been studied, and some doubts even arose about the necessity of such an architecture. Implementation of a Strang splitting scheme was vital to cope with the strong species coupling, but may have made global iterating superfluous. Such questions can be answered once reliable validation data is is obtained. Accuracy studies can then be performed to investigate reduction of errors.

Additionally, the solver was experienced to behave fairly robust. Simulations could be run stably for a wide range of input voltages and actuation frequencies, but also different mesh sizes. It should be added though that the CFL number, besides being already a strict time step restriction, did not always guarantee stability. During discharge, the increase in particle velocity can be so sudden that the current time step was too large to cope with this increase, and in one time step the maximum CFL number was exceeded. As a solution, the maximum time step was limited to values of 10^{-10}, which puts a lower limit on the number of iterations in the order of 10^6 for simulation times in the order of ms. This is very strict, and leads to a high demand of computational resources (computation time and storage). The solver architecture, and specifically its convergence behaviour, should be reassessed thoroughly to find ways to overcome strict limits in the maximum CFL and time step values.

Finally, the implementation was designed for 2D, although the capabilities in multi-dimensions could not be proven. Some tests were performed, but instabilities arose quickly once breakdown was reached. This left the 2D geometry and the Bolsig+ data for air presented in this work untouched. This is an important step towards modelling of DBD utilized for active flow control, and continuation with this step is then also firmly recommended for future work. Similarly, the functionalities were only demonstrated for rectangular geometries and grids. Future work should also strive for verification and validation on non-uniform and non-rectangular meshes, which could be a step-up to investigation on cylinders and air foils.

Chapter 6

Conclusion and outlook

In this section, the conclusion to this report is given. First, the main findings of every section is recapitulated. Then, the research question and its sub-questions are evaluated and answered, and the final conclusion is formulated based on the conclusions drawn before. Finally, recommendations for future work are given.

6.1 Report recapitulation

In chapter 2, a background study was given on the processes involved in electric discharge in gaseous media. A non-equilibrium cold plasma can be generated by applying a strong electric field between two electrode plates. Plasma, the fourth state of matter, consists of free charge carriers in a neutral parent gas and has improved electric properties compared to its gas counterpart, which allows it to facilitate electric currents. Two distinct types of current used to quantify a discharge were introduced, namely the conductive and displacement current. The first is determined by transport of charged species, while the latter indicates the time rate of change of the electric field strength. Furthermore, the ionization factor α_p was introduced as a quantification of the degree of ionization, where $\alpha_p < 0.1\%$ indicates a weak plasma. Flow control methods relying on electric discharge in gas only rely on weak plasma. Another quantification of plasma is the Debye length or shielding length, $\lambda_{e,i}$, which is a characteristic length scale depending on the plasma species density and temperature.

After the short introduction on plasma, a 1D volume discharge test case was introduced, with which different discharge regimes were obtained theoretically. The Townsend breakdown or electron avalanche was marked as the primary breakdown process, from which a glow, corona, streamer or arc discharge can evolve. The arc discharge is undesired in many applications and can be prevented by inserting a dielectric-barrier between the two electrodes. The Townsend ionization coefficient α was introduced, depicting the spatial growth of electrons in a plasma. A breakdown condition was formulated, which relates the secondary electron emission γ and

α to whether a discharge is sustained, which is the case if at least one electron is released from the cathode or dielectric-barrier. This takes place at a breakdown voltage V_{br}, which is a function of the similarity parameter $P_{gas}d$, called the pressure-gap-product. From this product, the more commonly used reduced electric field similarity parameter E/N was derived, which includes the electric potential in its scaling.

The study continues with a closer look at streamer discharges, which is a type of discharge generated at high over-voltages and medium to high pressures strongly influenced by photo-ionization. Three stages were distinct in the process, starting with an electron avalanche, followed by a positive or negative streamer. Finally, when the streamer head reaches the other electrode, the circuit is closed and a filament of plasma is formed.

In the area of active flow control, streamer as well as corona discharges can be generated using a dielectric-barrier, which is an insulating but polarizing material shielding at least one of the electrodes from the plasma, preventing any discharge to evolve into an arc discharge. Characteristic time scales governing the processes of dielectric-barrier were introduced, of which the most limiting is the dielectric relaxation time. Mainly two different input wave forms are applied in active flow control: continuous AC wave forms and repetitive pulsed nanosecond wave forms. The first mainly induces a body force on the neutral flow, creating an ionic wind with some additional aeroacoustic disturbances. These disturbances are the main product of the nanosecond pulsed actuation, during which the main driving mechanism is rapid energy deposition, generating weak shock waves in the neutral flow.

Both actuator types have multiple applications, of which separation control, laminar-turbulent transition, lift enhancement and drag reduction, shock wave control and combustion augmentation are the most important examples.

In chapter 3, the physical model was presented which describes the model problem relevant in numerical simulation of DBD. Two geometries were shown, one for 1D symmetric volume discharge and one for 2D asymmetric surface discharge, consisting of a gas region, two electrodes and one or two dielectric layers. The governing equations were derived from the Boltzmann equation and resemble a continuity equation for each species, coupled to Gauss' law for electrostatics: a Poisson equation relating the electric potential to the space charges. These space charges stem from the charged particles, described by the continuity equations through which the coupling takes place. The energy equation is neglected following the LFA. The continuity equations, also called drift-diffusion equations, often used in plasma modelling. The equations have been modified though, to fit the in aerodynamics more generally known convection-diffusion equations. It was found that the Péclet number of this problem is Pe $\geq 10^3$, indicating that this is a convection dominated problem. The physical model assumes only electrons and one type of positive and negative ion species each.

As was explained, the physical boundary conditions are mainly concerned with the fact that charged particles instantly recombine when colliding on polarized geometric surfaces. This introduces a charge surface density: charge is conserved as it leaves the volume as it is stored on the surface. This surface charge influences the potential on the gas-dielectric region interfaces, which is incorporated in the electric field compatibility condition. This condition conserves charge continuity and is the boundary condition for Gauss' law.

The assumption of instant recombination leads to free flow of species out of the domain, which is controlled by setting the species velocities on these boundaries. Two sets of conditions were implemented for the flux boundary values, one ignoring diffusion towards the surface (Boeuf et al. (2009), while the other does not (Hagelaar et al. (2000)). Random motion towards the surfaces due to thermal velocity is taken into account in both sets. Also, collisions of heavy particles onto a surface trigger secondary electron emission. The latter set of conditions makes a distinction between secondary electrons just released from the surface and electrons already present in the domain. The first set treats all electrons equally, which may lead to a non-physically high effective secondary electron emission coefficient γ. The species gradients are in all cases set to zero, as diffusion towards the surface is either assumed zero or incorporated in the species flux term.

On the outer boundaries of the computational domain, far field (symmetric) conditions were imposed for all variables ϕ, $\vec{U}_k$ and n_k.

Photo-ionization was treated by assuming an initial neutral plasma, which was set through the initial conditions for the species densities.

The implementation of the physical model into the OpenFoam® package was reported in chapter 4, which started off with an introduction to finite volume discretization in OpenFoam® . The mesh topology was described, which consist only of square cells. Variable fields can be defined on either the centres or the faces of these cells. Outer faces are collected under patches, which can be assigned certain boundary types, such as a symmetric or wall type.

OpenFoam® uses iterative solution methods to solve coefficient matrices, which are constructed from the equations to solve. Different solution methods are available, but only the PCG and GAMG methods have been utilized in this study. Furthermore, the first order forward Euler and second order backward Euler temporal discretization schemes were introduced, where it was concluded that the forward Euler has a disadvantage over the second order scheme as the cumulative discretization error will remain the same with varying number of time steps. On the other hand, forward Euler can be combined with sub-cycling, while the backward Euler scheme would require special implementation. Therefore, the forward Euler is the preferred method in this work.

To overcome strict time step limits, the governing equations were rewritten in a semi-implicit form. For Gauss' law, this required a first order approximation of the space charge, as the Poisson is an elliptic PDE and requires the solution at the current time step, which should be approximated and corrected for. This led to a predictor-corrector algorithm: using the first order approximation, the electric field at the next time step is predicted. Then, a corrector loop will converge the coupled electric and density fields. The continuity equations contain heavily coupled source terms, and are solved using a Strang splitting method which required implementation of a sub-cycling routine.

To complete the system of equations of this model problem, reaction rates and mobility coefficients are required. These are obtained by the Boltzmann solver Bolsig+, which yield look-up tables for the variables, which requires a linear interpolation routine to find the values for any value of the reduced electric field. The transport coefficients are determined by the gas composition, pressure and temperature. The reaction rates are determined by the chemical model, and additionally depend on the incorporated chemical reactions. Two gases were treated, being helium and air, which is a 79%-21% nitrogen-oxygen mixture. To helium, 0.5% argon was added to account for Penning ionization. Finally, power fraction terms were obtained, also from the Bolsig+ software, which quantify the ratio of energizing of translation and rotational motion, vibrational excitation or electronic excitation of the particles. In correspondence to the LFA, the energy absorbed by the particles from the electric field is deposited into the neutral flow again in the form of elastic and inelastic collisions and appearing and disappearing of electrons through ionization and attachment.

As the system of equations was completed, the boundary conditions could be implemented. The condition coupling the electric fields in the different regions was discretized and implemented using the groovyBC package, which facilitates non-uniform boundary conditions using user-set functions. The discretization was first order, which will limit the order of the Poisson scheme to first order as well. As the regions are solved sequentially and not parallel, the iterative routine behaves as a Gauss-Seidel method and allows for over-relaxation.

The chapter concluded with an overview of the predictor-corrector numerical procedure. Three units were distinguished: the coupled-Poisson solver, the convection-diffusion model for species transportation, and the source terms accounting for the reactive model. The solution is controlled by two residuals: the electric field coupling condition residual and the relative residual of the EHD force. The first should assure convergence of the electric field, while the latter is a measure of change of the magnitude of the force, and therefore a measure of change of the electric and species density fields. The CFL number is used to control the variable time step.

The numerical mode was put to the test in chapter 5, where code verification was used to test convergence. Coupling of the electric field in the different regions was controlled by a tolerance ϵ_ϕ for the normalized residual norm r_ϕ. The coupling was proven to work, and the tolerance sets the percentile error of the electric field, i.e. a tolerance of 10% yields convergence at a 10% offset from the exact solution. Mesh convergence was checked, where a first order behaviour was observed. Convergence could be sped up by a relaxation factor, which reduced the number of iterations by a factor three at a value of $\alpha = 2$.

The effect of the relative permittivity was investigated, which is a measure of the capacitance of the dielectric material. In the limit of $\lim_{\varepsilon_d \to \infty}$, the dielectric behaves as a capacitor in which the electric field, and therefore electric losses, approach zero. The potential energy between the plates must be conserved, increasing the electric field strength in the fluid domain.

Space charges were introduced through the method of manufactured solutions, with which convergence and accuracy of the Laplacian scheme can be analysed. A sinusoidal distribution of the space charge was assumed, from which an exact solution of the electric potential and field can be derived by substitution into the Poisson equation. The space charge distribution was introduced in a test case, and the solution computed by the solver was compared to the analytical solution. From a mesh convergence study, a first order accuracy was derived. This is not expected from a Laplacian scheme, but can be explained by the first order coupling condition.

Implementation of the homogeneous convection-diffusion equations was assessed in a similar manner. Now, an exact solution for the electron density was assumed, as a quadratic sinusoidal function in both space and time. To get the combined order of accuracy, the spatial and temporal resolutions were refined simultaneously. First order accuracies were observed for combinations of the MUSCL scheme with both the first order forward Euler scheme and the second order backward Euler scheme. It was concluded that while the MUSCL scheme formally is second order, in practice this scheme is mostly first order. The highest order term is then the dominating term, explaining the first order observed for both scheme combinations.

Non-linear effects in the solution of the electric field as well as in the solution of the species densities were demonstrated with an example in which species were transported in an electric field distorted by surface and volume charges. Quenching of the electric field was observed through charging of the dielectric surfaces. The thermal velocity was shown to be of significant influence, although doubt was posed on

The two proposed sets of flux boundary conditions were compared against one another, although only minor differences were observed. Stronger distinction is expected when the chemical model is incorporated, although this was not tested.

Finally, the model was validated against a reference case which entailed a volumetric glow discharge under a sinusoidal actuation signal. A cathode-fall glow discharge is then obtained, characterised by peak densities of the species near the cathode, with two sheaths of increasing electric field near the anode and cathode. Although quantitative validation was not achieved, the model results showed good correspondence with the reference data, which were validated against experimental data. Current peaks in the same order of magnitude were observed, as well as similar species spatial distributions at those current peaks. The electric field typical for a cathode-fall was observed as well.

This concludes the body of this report. Now, the research question can be answered.

6.2 Conclusion

In this section, the main research question will be answered. Answers to the sub-questions can be distilled from the main answer, but will not be given individually. The research question posed in the introduction was:

How can a robust and flexible computational framework be established for modelling of dielectric-barrier discharge in gaseous media?

This robust and flexible computational framework could be established as follows. The physics of the underlying problem were investigated to identify the characteristic time scales and processes to be modelled. Physics of DBD is characterised by transport and production of charged particles in its parent gas, described by species continuity equations. These processes are driven by the electric field, generated by a voltage potential between two electrodes. At least one of these electrodes is covered by a dielectric material, which has insulating but polarizing electric properties. This electric field is described by Gauss' law and varies with input voltage, but also with space and surface charges in the gas. These free charged particles are not present in the dielectric, and so a partitioned approach was chosen, in which each physical region (gas, dielectrics and electrodes) is solved for in a segregated manner. This requires a condition for the electric field coupling the different regions. This condition was formulated in a first order discretization, which made the complete Laplacian scheme first order accurate.

Because of the nature of Gauss' law, which is an elliptic PDE, an initial value problem is posed when the volume and surface charges are dependent on time. Namely, these charges determine the electric field distribution at a time step at which these values are not known yet. This puts a severe restriction on the maximum allowable time step. To overcome this restriction, a predictor-corrector like method was implemented. At a new time step, the electric field was predicted using a first order approximation of the charge densities based on the values of the former time step. With this approximation, the continuity equations can be advanced. With the corrected species densities, the electric field can be corrected again, this time without the first order approximation. This iterative process is then repeated until the solution converged for this time step. This procedure allows for exceeding of the dielectric relaxation time step.

Another numerical challenge was posed by the creation and destruction of different species. Chemical reactions, such as ionization, attachment and recombination, involve multiple species. Their continuity equations are then also highly coupled, which poses another serious time step restriction. This was overcome by implementing a Strang splitting method, where each continuity equation was split in a homogeneous and a reactive part. Each part was then integrated over time in a sequence, to provide each succeeding integration with updated information.

The reliability of the framework was verified through code verification, mainly using the method of manufactured solutions. First order accuracies were found for the Laplacian scheme and the MUSCL spatial scheme, both formally second order, but this discrepancy were clarified and, more importantly, the solution converges, which means at least reliable results can be produced.

The precision of the framework could not be validated quantitatively, which should be done using experimental data. This was out of the scope of this work, and so qualitative validation was done against data from a publication. A 1D volumetric glow discharge was simulated successfully, with orders of magnitude of the discharge current, electric field strength and species densities in agreement with the values presented in the reference.

All undertaken steps have yielded a computational framework sufficiently robust for the scope of this work, although with a severe penalty on computational efficiency. To assure robustness and an acceptable level of efficiency in more advanced applications, a number of improvements have to be made in future work.

6.3 Recommendations

In this section, recommendations are made for future work to improve robustness and efficiency of the framework. These recommendations comprise essential steps to take towards a framework applicable to active flow control, and reflect doubts and uncertainties experienced during usage of the framework so far, as well as work out of scope in the current project.

Some numerical features have been implemented which have not been tested or evaluated properly. One example is the difference in the Godunov and Strang splitting methods, which should be investigated. Also, the impact of the convergence tolerance of the corrector loop has not been assessed. Doing so could give insight in the minimum required tolerance, which can then be optimized for minimum required computation time.

The motivation for creating this framework was to ultimately simulate discharges applicable to active flow control. This consists of asymmetric (i.e. 2D) actuator configuration in air, either driven by a continuous AC or nanosecond pulsed signal.

Firstly, the simulations run in this work have all been limited to one dimension. For verification and validation purposes, this is very interesting. For applications to flow control, at least 2D is required to obtain any interesting results. Advancement of the framework to facilitate 2D computations would be of high interest.

Secondly, the parent gas used in this study was helium. As flow control concerns air, it would be very interesting to extend the simulations to this medium. The transport and reaction data were already presented in this work, and have already been implemented in the framework. All is left is validation of the chemical model.

Thirdly, this study limited itself to relative low amplitude continuous sinusoidal actuation to generate glow discharges. As the plasma dynamics are essentially the same and the governing equations are valid for both types of discharge, this model can also be used to simulate streamer discharges by applying a pulsed nanosecond actuation.

Finally, also the plasma-neutral flow interaction can be studied, using the presented but so far unused coupling terms and power fractions. Ultimately, The output of this model can be used as input to a neutral flow model, with which the ionic wind or weak shock waves, generated by the discharge, can be simulated and studied. In some literature, integrated discharge-neutral flow dynamics models were presented, which solve the discharge physics and the flow interaction simultaneously. This is very interesting, but also very challenging. Hopefully, the developed framework supported by this report can serve as a first step to such a model.

Bibliography

M. Abdollahzadeh, J. C. Pascoa, and P. J. Oliveira. Two-dimensional numerical modeling of interaction of micro-shock wave generated by nanosecond plasma actuators and transonic flow. *Journal of Computational and Applied Mathematics*, 270:401–416, 2014. ISSN 03770427. doi: 10.1016/j.cam.2013.12.030. URL `http://dx.doi.org/10.1016/j.cam.2013.12.030`.

M. Abdollahzadeh, J. C. Pascoa, and P. J. Oliveira. Implementation of the classical plasmafluid model for simulation of dielectric barrier discharge (DBD) actuators in OpenFOAM. *Computers & Fluids*, 128:77–90, 2016. ISSN 00457930. doi: 10.1016/j.compfluid.2016.01.012. URL `http://linkinghub.elsevier.com/retrieve/pii/S0045793016300044`.

R. Arpa and D. D'Ambrosio. High-order accurate implicit scheme for drift-diffusion equations and application to dielectric barrier discharges. In *40th AIAA Plasmadynamics and Lasers Conference*, page 3909, 2009.

N. Benard and E. Moreau. Response of a circular cylinder wake to a symmetric actuation by non-thermal plasma discharges. *Experiments in fluids*, 54(2):1467, 2013.

M. S. Benilov and G. V. Naidis. Modelling of discharges in a flow of preheated air. *Plasma Sources Science and Technology*, 14(1):129, 2005.

J. P. Boeuf, Y. Lagmich, Th. Unfer, Th. Callegari, and L. C. Pitchford. Electrohydrodynamic force in dielectric barrier discharge plasma actuators. *Journal of Physics D: Applied Physics*, 40(3):652–662, 2007. ISSN 0022-3727. doi: 10.1088/0022-3727/40/3/S03. URL `http://stacks.iop.org/0022-3727/40/i=3/a=S03?key=crossref.602cdfe93259b6e4678cf12a749c567d`.

J. P. Boeuf, Y. Lagmich, and L. C. Pitchford. Contribution of positive and negative ions to the electrohydrodynamic force in a dielectric barrier discharge plasma actuator operating in air. *Journal of Applied Physics*, 106(2), 2009. ISSN 00218979. doi: 10.1063/1.3183960.

B. A. Carré. The determination of the optimum accelerating factor for successive over-relaxation. *The computer journal*, 4(1):73–78, 1961.

E. L. Collier and M. C. Gourdine. Resistive wall EGD channel. *AIAA Journal*, 6:2278–2281, December 1968. doi: 10.2514/3.4983.

R. Courant, K. Friedrichs, and H. Lewy. Über die partiellen differenzengleichungen der mathematischen physik. *Mathematische annalen*, 100(1):32–74, 1928.

C. L. Enloe, Th. E. McLaughlin, Robert D. Van Dyken, K. D. Kachner, E. J. Jumper, Th.C. Corke, M. Post, and O. Haddad. Mechanisms and Responses of a Dielectric Barrier Plasma Actuator: Geometric Effects. *AIAA Journal*, 42(3):595–604, 2004.

A. Flitti and S. V. Pancheshnyi. Gas heating in fast pulsed discharges in NO mixtures. *The European Physical Journal Applied Physics*, 45(2):21001, 2009. ISSN 1286-0042. doi: 10.1051/epjap/2009011. URL `http://peer.ccsd.cnrs.fr/peer-00480145/$\delimiter"026E30F$nhttp://www.epjap.org/10.1051/epjap/2009011`.

A. Glezer, M. Amitay, and A. M. Honohan. Aspects of Low- and High-Frequency Actuation for Aerodynamic Flow Control. *AIAA Journal*, 43(7):1501–1511, 2005. ISSN 0001-1452. doi: 10.2514/1.7411.

S. Goekce. PLASMA DIAGNOSTICS AND MODELLING OF NANOSECOND PULSED ACTUATORS. 6282, 2014.

Yu. B. Golubovskii, V. A. Maiorov, J. Behnke, and J. F. Behnke. Modelling of the homogeneous barrier discharge in helium at atmospheric pressure. *Journal of Physics D: Applied Physics*, 36(1):39, 2002a.

Yu. B. Golubovskii, V. A. Maiorov, J. Behnke, and J. F. Behnke. Influence of interaction between charged particles and dielectric surface over a homogeneous barrier discharge in nitrogen. *Journal of Physics D: Applied Physics*, 35(8):751, 2002b.

C. J. Greenshields. *OpenFOAM Programmers Guide*. CFD Direct Ltd.

Sv. Grundmann and C. Tropea. Active cancellation of artificially introduced Tollmien-Schlichting waves using plasma actuators. *Experiments in Fluids*, 44(5):795–806, 2008. ISSN 07234864. doi: 10.1007/s00348-007-0436-6.

V. Guerra, P. A. Sá, and J. Loureiro. Kinetic modeling of low-pressure nitrogen discharges and post-discharges, 2004.

G. J. M. Hagelaar and L. C. Pitchford. Solving the Boltzmann equation to obtain electron transport coefficients and rate coefficients for fluid models. *Plasma Sources Science and Technology*, 14(4):722–733, 2005. ISSN 0963-0252. doi: 10.1088/0963-0252/14/4/011. URL `http://stacks.iop.org/0963-0252/14/i=4/a=011?key=crossref.2a24e96f0d2a1cd028c8141d01c6b2b0`.

G. J. M. Hagelaar, F. J. De Hoog, and G. M. W. Kroesen. Boundary conditions in fluid models of gas discharges. *Physical Review E*, 62(1):1452, 2000.

A. Harten. High resolution schemes for hyperbolic conservation laws. *Journal of computational physics*, 49(3):357–393, 1983.

Ch. He, Th. C. Corke, and M. P. Patel. Plasma Flaps and Slats: An Application of Weakly Ionized Plasma Actuators. *Journal of Aircraft*, 46(3):864–873, 2009. ISSN 0021-8669. doi: 10.2514/1.38232.

A. R. Hoskinson. Measurements and Simulations of Surface Dielectric Barrier Discharges Used as Plasma Actuators. 3384093(September):104, 2009. doi: 20120014222. URL http://ezproxy.net.ucf.edu/login?url=http://search.proquest.com/docview/305034109?accountid=10003$\delimiter"026E30F$nhttp://sfx.fcla.edu/ucf?url{_}ver=Z39.88-2004{&}rft{_}val{_}fmt=info:ofi/fmt:kev:mtx:dissertation{&}genre=dissertations+{&}+theses{&}sid=ProQ:ProQuest+Dissertations+{&}+The.

J. Huang, Th. C. Corke, and F. O. Thomas. Plasma actuators for separation control of low-pressure turbine blades. *Aiaa J.*, 44(1):51–57, 2006.

J. D. Jackson and R. F. Fox. Classical electrodynamics. *American Journal of Physics*, 67(9): 841–842, 1999.

H. Jasak. Error analysis and estimation for finite volume method with applications to fluid flow. 1996.

B. Jayaraman and W. Shyy. Modeling of dielectric barrier discharge-induced fluid dynamics and heat transfer, 2008. ISSN 03760421.

B. Jayaraman, S. Thakur, and W. Shyy. Modeling of Fluid Dynamics and Heat Transfer Induced by Dielectric Barrier Plasma Actuator. *Journal of Heat Transfer*, 129(4):517, 2007. ISSN 00221481. doi: 10.1115/1.2709659.

I. A. Kossyi, A. Y. Kostinsky, A. A. Matveyev, and V. P. Silakov. Kinetic scheme of the non-equilibrium discharge in nitrogen-oxygen mixtures. *Plasma Sources Science and Technology*, 1(3):207, 1992.

M. Kotsonis. Diagnostics for Characterisation of Plasma Actuators. *Measurement Science and Technology*, 092001:92001, 2015. ISSN 0957-0233. doi: 10.1088/0957-0233/26/9/092001. URL http://dx.doi.org/10.1088/0957-0233/26/9/092001.

M. Kotsonis, R. Giepman, and L. M. Veldhuis. Numerical Study on Control of Tollmien-Schlichting Waves Using Plasma Actuators. (June), 2011.

M. Kotsonis, R. Pul, and L. M. Veldhuis. Influence of circulation on a rounded-trailing-edge airfoil using plasma actuators. *Experiments in Fluids*, 55(7), 2014. ISSN 07234864. doi: 10.1007/s00348-014-1772-y.

A. A. Kulikovsky. A more accurate scharfetter-gummel algorithm of electron transport for semiconductor and gas discharge simulation. *Journal of computational physics*, 119(1): 149–155, 1995.

G. Lee, F. K. Jiang, Th. Tsao, Y. C. Tai, and C. M. Ho. Macro aerodynamic devices controlled by micro systems. In *Aerospace Conference, 1997. Proceedings., IEEE*, volume 3, pages 255–263. IEEE, 1997.

M. A. Lieberman and Lichtenberg A. J. *Principles of plasma Discharges and Materials Processing*. 1994. ISBN 9786468600.

A. V. Likhanskii, M. N. Shneider, S. O. Macheret, and R. B. Miles. Modeling of Interaction Between Weakly Ionized Near-Surface Plasmas and Gas Flow. *44th AIAA Aerospace Sciences Meeting and Exhibit*, (January):1–26, 2006. doi: 10.2514/6.2006-1204.

A. V. Likhanskii, M. N. Shneider, S. O. MacHeret, and R. B. Miles. Modeling of dielectric barrier discharge plasma actuator in air. *Journal of Applied Physics*, 103(5), 2008. ISSN 00218979. doi: 10.1063/1.2837890.

J. Little, M. Nishihara, I. Adamovich, and M. Samimy. High-lift airfoil trailing edge separation control using a single dielectric barrier discharge plasma actuator. *Experiments in fluids*, 48(3):521–537, 2010.

J. Little, K. Takashima, M. Nishihara, I. Adamovich, and M. Samimy. Separation Control with Nanosecond Pulse Driven Dielectric Barrier Discharge Plasma Actuators. *AIAA Journal*, 50(2):350–365, 2012. ISSN 0001-1452. doi: 10.2514/1.J051114.

L. Mangolini, C. Anderson, J. Heberlein, and U. Kortshagen. Effects of current limitation through the dielectric in atmospheric pressure glows in helium. *Journal of Physics D: Applied Physics*, 37(7):1021, 2004.

Fr. Massines, A. Rabehi, Ph. Decomps, R. B. Gadri, P. Ségur, and Chr. Mayoux. Experimental and theoretical study of a glow discharge at atmospheric pressure controlled by dielectric barrier. *Journal of Applied Physics*, 83(6):2950, 1998. ISSN 00218979. doi: 10.1063/1.367051. URL `http://link.aip.org/link/JAPIAU/v83/i6/p2950/s1{&}Agg=doi`.

J. M. Meek and J. D. Craggs. Electrical breakdown of gases, 1953.

E. Moreau. Airflow control by non-thermal plasma actuators. *Journal of Physics D: Applied Physics*, 40(3):605–636, 2007. ISSN 0022-3727. doi: 10.1088/0022-3727/40/3/S01.

G. Nati, M. Kotsonis, S. Ghaemi, and F. Scarano. Control of vortex shedding from a blunt trailing edge using plasma actuators. *Experimental Thermal and Fluid Science*, 46:199–210, 2013. ISSN 08941777. doi: 10.1016/j.expthermflusci.2012.12.012. URL `http://dx.doi.org/10.1016/j.expthermflusci.2012.12.012`.

D. Nicholson. Introduction to Plasma Theory, 1983.

M. Nishihara, K. Takashima, J. W. Rich, and I. V. Adamovich. Mach 5 bow shock control by a nanosecond pulse surface dielectric barrier discharge. *Physics of Fluids*, 23(6):066101, 2011.

S. Pancheshnyi. Role of electronegative gas admixtures in streamer start, propagation and branching phenomena. *Plasma Sources Science and Technology*, 14(4):645–653, 2005. ISSN 0963-0252. doi: 10.1088/0963-0252/14/4/002.

S. Pancheshnyi, S. Biagi, M. C. Bordage, G. J. M. Hagelaar, W. L. Morgan, A. V. Phelps, and L. C. Pitchford. The lxcat project: Electron scattering cross sections and swarm parameters for low temperature plasma modeling. *Chemical Physics*, 398:148–153, 2012.

F. Paschen. Ueber die zum funkenübergang in luft, wasserstoff und kohlensäure bei verschiedenen drucken erforderliche potentialdifferenz. *Annalen der Physik*, 273(5):69–96, 1889.

S. Pavón. Interaction between a surface dielectric barrier discharge and transonic airflows. *EPFL thesis*, 4201, 2008. URL `http://infoscience.epfl.ch/record/125997/files/EPFL{_}TH4201.pdf`.

Ph. Peschke. Experimental investigation of pulsed {DBD} plasma actuators for aerodynamic flow control. 6265, 2014.

N. A. Popov. Investigation of the mechanism for rapid heating of nitrogen and air in gas discharges. *Plasma physics reports*, 27(10):886–896, 2001.

M. L. Post and T. C. Corke. Separation control on high angle of attack airfoil using plasma actuators. *AIAA Journal*, 42(11):2177–2184, 2004. ISSN 00011452. doi: 10.2514/1.2929. URL `http://www.scopus.com/inward/record.url?eid=2-s2.0-9744279704{&}partnerID=tZOtx3y1`.

C. Punset, S. Cany, and J. P. Boeuf. Addressing and sustaining in alternating current coplanar plasma display panels. *Journal of Applied Physics*, 86(1):124, 1999. ISSN 00218979. doi: 10.1063/1.370709. URL `http://scitation.aip.org/content/aip/journal/jap/86/1/10.1063/1.370709`.

Y. P. Raizer and J. E. Allen. *Gas discharge physics*, volume 2. Springer Berlin, 1997.

J. R. Roth. Electrohydrodynamically induced airflow in a one atmosphere uniform glow discharge surface plasma. *Plasma Science, 1998. 25th Anniversary. IEEE ...*, page 1998, 1998. ISSN 07309244. URL `http://ieeexplore.ieee.org/xpls/abs{_}all.jsp?arnumber=677891`.

C. J. Roy. Review of code and solution verification procedures for computational simulation. *Journal of Computational Physics*, 205(1):131–156, 2005.

D L Scharfetter and H K H. K. Gummel. Large-signal analysis of a silicon tead diode oscillator. *Electron Devices, IEEE Transactions on*, {ED}.16(1):64–77, 1969.

S. M. Starikovskaia. Plasma-assisted ignition and combustion: nanosecond discharges and development of kinetic mechanisms. *Journal of Physics D: Applied Physics*, 47(35):353001, 2014.

A. Yu. Starikovskii. Plasma supported combustion. *Proceedings of the Combustion Institute*, 30 II:2405–2417, 2005. ISSN 15407489. doi: 10.1016/j.proci.2004.08.272.

A. Yu. Starikovskii, A. A. Nikipelov, M. M. Nudnova, and D. V. Roupassov. SDBD plasma actuator with nanosecond pulse-periodic discharge. *Plasma Sources Science and Technology*, 18(3):34015, 2009. ISSN 0963-0252. doi: 10.1088/0963-0252/18/3/034015. URL `http://stacks.iop.org/0963-0252/18/i=3/a=034015`.

F. O Thomas, A. Kozlov, and Th. C. Corke. Plasma Actuators for Cylinder Flow Control and Noise Reduction. *AIAA Journal*, 46(8):1921–1931, 2008. ISSN 0001-1452. doi: 10.2514/1.27821. URL `http://arc.aiaa.org/doi/abs/10.2514/1.27821`.

T. Unfer and J. P. Boeuf. Modelling of a nanosecond surface discharge actuator. *Journal of Physics D: Applied Physics*, 42:194017, 2009. ISSN 0022-3727. doi: 10.1088/0022-3727/42/19/194017.

Th. Unfer. *Méthode asynchrone pour la modélisation d'actuateurs plasma destinés au contrôle d'écoulement*. PhD thesis, Université de Toulouse, Université Toulouse III-Paul Sabatier, 2008.

Th. Unfer and J. P. Boeuf. Modeling and comparison of sinusoidal and nanosecond pulsed surface dielectric barrier discharges for flow control. *Plasma Physics and Controlled Fusion*, 52(12):124019, 2010. ISSN 0741-3335. doi: 10.1088/0741-3335/52/12/124019. URL `http://stacks.iop.org/0741-3335/52/i=12/a=124019?key=crossref.288003bb9f620a470adf12bf832a987d`.

B. Van Leer. Muscl, a new approach to numerical gas dynamics. In *Computing in Plasma Physics and Astrophysics*, volume 1, 1976.

A. L. Ward. Calculations of cathode-fall characteristics. *Journal of Applied Physics*, 33(9):2789–2794, 1962.

Appendix A

OpenFoam® tips and tricks

This appendix is meant to summarize and, more importantly, document the discoveries made with regard to OpenFoam® during this project. Installation of the OpenFoam® software is well described on the website[1].

For the development of the presented in this document, the following software was used. The code was developed in OpenFoam® version 3.0.X on Ubuntu 14.04.5 LTS. The `swak4Foam`[2] package was used for the groovyBC and funkyFields utilities.

OpenFoam® Applications

In this section, the built-in applications used in this work are briefly commented on. These functions are sequentially executed when running the Allrun or AllSingleRun .sh files for readers in possession of the developed framework, but can also be executed manually. The order is fixed, though, and is presented below.

The `runApplication <application>` command executes the application with corresponding flags, and writes the output to a log file called "log.application".

First, the mesh is created using the `blockMesh` functionality. This requires the blockMeshDict in the system folder.

Listing A.1: Create the mesh.

```
$ runApplication blockMesh
```

Second, the region topology is set using the `topoSet` functionality. This requires the topoSet-

---

[1] https://openfoam.org/?s=3.0

[2] http://openfoamwiki.net/index.php/contrib/swak4Foam

Dict in the system folder and splits the mesh into the desired regions, indicated by bounding boxes. The mesh should be divided over the regions completely, else OpenFoam® will insert arbitrary regions, which may lead to execution errors as e.g. on the also newly created patches of these domains, the boundary conditions are undefined.

Listing A.2: Define the multi-region topology.

```
$ runApplication topoSet
```

Third, the mesh is split using the `splitMeshRegions` functionality. This only requires the set region topology in the step before.

Listing A.3: Split the mesh into sub-meshes.

```
$ runApplication splitMeshRegions -cellZones -overwrite
```

Fourth, the dictionaries are adjusted, according to the changeDictionaryDict in each region sub-folder. Here, patch types and boundary conditions can be altered. This utility is also used to implement the groovyBC functions.

Listing A.4: Change the boundary and initial field dictionaries for every region.

```
$ for i in anode cathode air dielectricAnode dielectric
$ do
$    changeDictionary -region $i > log.changeDictionary.$i 2>&1
$ done
```

When one is interested in altering the initial field values, the setFields functionality can be called. This functionality is only able to create uniform fields though, so for any non-uniform field, funkySetFields is used, which is a brother of groovyBC. The function requires specification of the time folder it should alter the field, as well as the specific region.

Listing A.5: Optionally set the initial field values using spatial functions.

```
$ runApplication funkySetFields -time 0 -region air
```

The `‘getApplication‘` gets the name of the application it should execute from the controlDict dictionary.

Listing A.6: Execute the application on a single processor.

```
# Run on single processor
$ runApplication ‘getApplication‘
```

Parallel computation has not been used in this work, but it has been explored. Alternatively to a single processor, parallel computation can be chosen. This requires the mesh to be decomposed first. This is another decomposition than the region splitting, which concerned the different physical regions. Mesh decomposition for parallel computing means all regions are again decomposed and divided over the different processors. This functionality relies on the decomposeParDict in each region sub-folder, and therefore can also be controlled per region. The application is then run using the same command as for a single processor, just with the addition of the number of processors (in this case 4). Finally, the mesh is reconstruct during which output data from each processor is collected and written to a single output folder (per output time index).

Listing A.7: Execute the application on a multiple processors.

```
# Decompose
$ runApplication decomposePar -allRegions

# Run on multiple processors
$ runParallel ‘getApplication‘ 4

# Reconstruct
$ runApplication reconstructPar -allRegions
```

In the controlDict, the data output frequency can be controlled, resulting in a number of sub-folders in the case folder, named and sorted according to the simulation time at which the output was created. This data is written in OpenFoam® format but can be sampled into other formats, such as gnuplot readable files. This is done per region. The standard output directory if the same per region, so after sampling a region, the folder has to be renamed to prevent being overwritten by the next.

Listing A.8: Sample the output data.

```
$ for i in cathode dielectric air anode  dielectricAnode
$ do
$    sample -region $i > log.sample.$i 2>&1
$    mv "postProcessing/surfaces/" "postProcessing/"$i"Surfaces/"
$ done
```

Alternatively, the data can be visualised directly in paraView. To collect the different regions, the `-builtin` flag should be added.

Listing A.9: View in paraView.

```
# Open case in paraView
$ paraFoam -builtin
```

Pointer lists

In a multi-region set-up, OpenFoam® accesses variables in different regions sequentially. This requires either a different name convention for the variables in each region, or listing of these different variables under one pointer list. The latter allows for easy looping over different regions without the need for specifying different equations for each region variable. A pointer list is created through the command:

```
PtrList<volScalarField> phiFluid(fluidRegions.size());
```

It has the size of the number of regions (for example 1 for the fluid regions and 2 for the electrode regions) and has a number of entries equal to the number of cells in the domain in case of a volume field, and equal to the number of faces in case of a surface field.

The list is then populated by looping through the regions and adding the individual volume fields:

```
forAll(fluidRegions, i)
{
        phiFluid.set
        (
            i,
            new volScalarField
            (
                IOobject
                (
                    "phi",
                    runTime.timeName(),
                    fluidRegions[i],
                    IOobject::MUST_READ,
                    IOobject::AUTO_WRITE
                ),
                fluidRegions[i]
            )
        );
}
```

During the computational routine, the region variable can be summoned by calling the operation:

```
volScalarField& phi = phiFluid[i];
```

Patch fields

In general, patch fields of volume fields are protected, e.g. in case the patch types are specified as fixed value; as the value is fixed, the solver does not have to update anything in these fields. To give control over this access, two types of equality signs are available:

- ”=”, obeys patch protection according to the type of the patch (e.g. wall, mapped, coupled), and only the internal field will be accessed by the operation;
- ”==”, overloads patch protection and gives the specified operation write access to both the internal field and (all) patch fields.

Please note that the double ”==” is also used as a boolean operator, but only in certain statements involving scalars. For field classes, the operator acts as an ”equal to” statement.

For changing flux conditions on the boundaries, this ”==” statement is also required. The following code snippets shows how this can be done. use is made of pointers by adding a ”&”

behind the class declaration to create a reference to the original variable location, instead of creating a new independent variable location. This allows for modification of the referred to variable by modifying the pointer.

```
// Loop over all the patches available in the mesh of the current region.
forAll(mesh.boundary(), patchi)
{
  // Create read-only (const) pointer (&) p to the current patch with index patchi.
  const fvPatch& p = mesh.boundary()[patchi];

  // Create read-write pointer (&) peFlux to the s(urface)PatchScalarField of eFlux.
  fvsPatchScalarField& peFlux = eFlux.boundaryField()[patchi];

  // Create read-only pointer (&) pUe to the PatchVectorField of Ue.
  const fvPatchVectorField& pUe = Ue.boundaryField()[patchi];

  // Check that the accessed patch is not of the coupled type.
  if (!peFlux.coupled())
  {
    // Access (==) and set the electron flux sPatchScalarField peFlux equal to the inner product (&) of the patch normal vector p.Sf() and the internal field vector from the adjacent cell centre pUe.internalField().
    peFlux == p.Sf()&pUe.internalField();
  }
}
```

During parallel decomposition, the mesh is broken down in a number of separate meshes, coupled through interior patches. These patches are of the ”coupled” type, and as they are numerical boundaries, they should not be treated as physical boundaries. Thus, they are skipped during this operation. The operator $A\&B = A \cdot B$ denotes the inner product between A and B and should not be confused with the & denoting a pointer.

Writing to files

OpenFoam® , or rather C, contains a number of information stream functions which can be used in the source code to in- or output data. The following line for example calls an OpenFoam® function which writes some given input to the terminal:

```
Info<< "some scalar: " << scalar << endl;
```

The string is put between parenthesis, while the variable `scalar` is evaluated and printed. The terminal written output can also be redirected to a log file, by calling the OpenFoam® solver as follows:

```
$ corrDriftDiffusionFoam > log.corrDriftDiffusionFoam
```

The output printed by the `Info` function is then written to the log file. To gain more control over writing, functions similar to `Info` can be created by the user:

```
#include <iostream>
using namespace std;

{
  fileName myDir;
  if (Pstream::parRun())
  {
  myDir = mesh.time().path()/"..";
  }
  else
  {
  myDir = mesh.time().path();
  }

  if (Pstream::master())
  {
    word tracingFileName="file.dat";
    fileName myFile = myDir/tracingFileName;
    std::ofstream strIV(myFile.c_str(),ios_base::app);

    strIV<< DATA1 <<" "
         << DATA2 <<" "
         << DATA.. <<" "
         <<endl;
  }
}
```

Compiling the source code

To compile the source code, the following line can be executed from the `corrDriftDiffusionFoam` application folder:

```
  $ wclean
  $ wmake > log 2>&1
```

The compilation failed if the following line is returned:

```
  $ tailf -1 log
    make: *** [Make/linux64GccDPInt32Opt/corrDriftDiffusionFoam.o] Fout 1
```

Otherwise,

```
  $ tailf -1 log
    -lm -o /home/floris/OpenFOAM/floris-3.0.1/platforms/linux64GccDPInt32Opt/
       bin/corrDriftDiffusionFoam
```

Appendix B

Discretization methods proposed in literature

Below, two spatial discretization schemes are explained. Alternative temporal schemes are not included, but a highly interesting first and second order Runge-Kutta Legendre polynomial method, which can be combined with sub-cycling, can be found in Abdollahzadeh et al. (2016).

The momentum equation in the drift-diffusion equations poses a specifically challenging problem. The expression for the flux term consists of both a convection and a diffusion term. The physical relation is given by:

$$\Gamma_k = \pm\mu_k \vec{E} n_k - D_k \nabla n_k \tag{B.1}$$

Extreme high density gradients cause severe instability problems when describing the transport of species, a problem well known in numerical modelling of supersonic flows. Shocks create similar high density gradient regions, commonly even regarded as discontinuities, which require special attention to the discretization of the gradient term. Direction of propagation of information becomes a very important aspect by which central differencing will not suffice. Different discretization schemes have been proposed to cope with this problem, of which two interpolation schemes are elaborated on: the Scharfetter-Gummel Scharfetter and H. K. Gummel (1969) and the MUSCL scheme Van Leer (1976).

Scharfetter-Gummel discretization scheme

In plasma modelling, a large range of numerical values has to be dealt with. The number densities of a species can already range from orders of $\mathcal{O}(0)$ to $\mathcal{O}(1e24)$, in a computational domain with size in the order of $\mathcal{O}(cm)$. This yields enormous gradients, giving rise to instability in the approximation of the flux term $\vec{\Gamma}_k$ using standard discretization methods. This term is given by the relation:

$$\vec{\Gamma}_k = \pm\mu_k n_k \vec{E} - D_k \nabla n_k \tag{B.2}$$

According to Scharfetter and H. K. Gummel (1969), these instabilities arise when the difference in voltage potential between two cells exceeds two times the electron temperature T_{eV}, i.e. the voltage difference is limited by ($k = e, p, n$):

$$\Delta\phi < 2\frac{D_k}{mu_k} = 2T_k, \tag{B.3}$$

where the temperature T_k is in eV and Einstein's relation has been used for the diffusion coefficient D_k. Scharfetter and H. K. Gummel (1969) proposed to rewrite Equation B.2 into a differential equation, solve them analytically for the number density n_k and substitute the solution into a local approximated form of the original expression for the flux. For this approach to work, it must be assumed that the values of Γ_k, mu_k, D_k and E is constant between the two cells, which is done by interpolating these values to the face shared by the two cells.

$$\frac{\partial n(s)}{\partial s} = \frac{\mu_{face} E_{face}}{D_{face}} \frac{1}{n(s)} - \frac{1}{D_{face}} \Gamma_{face} \tag{B.4}$$

Solving this equation on the interval (s_p,s_{p+1}), where p denotes the current cell indices and s the cell center coordinates, an expression for n is obtained (Kulikovsky (1995)):

$$n(s) = (n_p - \frac{\Gamma_{face} h_p}{D_{face}} \int_0^{\xi} e^{\alpha\xi'} d\xi')e^{-\alpha\xi}, \tag{B.5}$$

where $h_p = s_{p+1} - s_p$, $\xi = \frac{s - s_p}{h_p}$ and

$$\alpha = \frac{\mu_{face} h_p E_{face}}{D_{face}}.$$

When taking $s = s_{p+1}$, i.e. the neighbour cell enclosing the considered face, Equation B.5

can be solved for analytically. Then, rewriting for the flux at a certain face yields:

$$\Gamma_{face} = \frac{D_{face}}{h_p I_0}(n_p - e^{\alpha} n_{p+1}), \tag{B.6}$$

with $I_0 = \frac{e^{\alpha}-1}{\alpha}$. As can be seen, the flux term has been rewritten into a form where the gradient term is replaced by formulating a local approximation of the number density at the next cell, and using this approximation to find the corresponding flux which should yield this approximated number density. This has resulted in a formulation with monotonic properties. This relation is the original formulation of the Scharfetter-Gummel (SG) scheme.

According to Kulikovsky (1995), the SG scheme is accurate as long as the potential difference is much less than the electron temperature (Equation B.3), which can be a very restrictive condition. Therefore, he has provided a scheme which dramatically improved the accuracy of the original SG scheme, even when this condition is not met. The method can be seen as temporary grid refinement, where two virtual points are introduced symmetrically around the corresponding face, between the two cell centres. The spacing between the two virtual points, h_v, is the original cell spacing h_p multiplied by a scaling factor. Doing so, a virtual cell stencil is produced which will always satisfy the aforementioned condition.

Now to obtain the relation for the flux term using the virtual point scheme, Equation B.5 is taken as starting point and written in a more general form:

$$n(s) = (n_p - \frac{\Gamma_{face} h_p}{D_{face}} \int_0^{\xi} e^{f(\xi')} d\xi') e^{-f(\xi)}, \tag{B.7}$$

where function f is defined as $f(y) = \alpha(y + \beta y^2)$, $\xi = \frac{s-s_v}{h_v}$, $\alpha = \frac{\mu_{face} h_v E_{face}}{D_{face}}$ and $\beta = \frac{\Delta E_v}{2E_v}$. Since $y < 1$, the exponential can be written as a power series, with the requirement that the product $|\alpha\beta| \ll 1$. For this requirement, a condition can be formulated by expanding $|\alpha\beta|$:

$$|\alpha\beta| = \frac{\mu_{face} h_v |E_v|}{2D_{face}} \ll 1 \Longrightarrow h_v \ll \frac{2D_{face}}{\mu_{face}|\Delta E_v|} \tag{B.8}$$

Given that E can be interpolated to the new cell nodes through $\Delta E_v = \frac{h_v}{h_p}\Delta E_p$, and introducing a scaling factor $\varepsilon \ll 1$ to ensure satisfaction of the condition in Equation B.8:

$$h_v = \sqrt{\frac{\varepsilon 2D_{face}}{|\Delta U_v|} h_p}, \tag{B.9}$$

where ΔU_v is the virtual point velocity difference, given by $\Delta U_v = \mu_{face}\Delta E_v$. ε is a user defined parameter to control the accuracy of the routine, ranging from 0 to 1, toggling the scheme from a highly accurate but dispersive one, to a less accurate and diffusive, but monotonic SG routine Kulikovsky (1995). In general, the value of ε is chosen between $0.01 - 0.04$.

Continuing with the derivation of the flux term, the exponent of the function $f(y)$ is power expanded in terms of $\alpha\beta$:

$$e^{f(y)} = e^{\alpha y}(1 + \alpha\beta y). \tag{B.10}$$

Which is always valid following the definition of h_v. The flux term can now be written as:

$$\Gamma_{face} = \frac{D_{face}}{h_p I}(n_L - e^{\alpha}(1 + \alpha\beta)n_R). \tag{B.11}$$

The integral $I = \int_0^1 e^{\alpha y}(1 + \alpha\beta y^2)dy$ can be analytically evaluated to:

$$I = -\frac{\alpha^2 + 2\alpha\beta}{\alpha^3} + \frac{e^{\alpha}}{\alpha^3}(\alpha^3\beta + \alpha^2 + 2\alpha\beta - 2\alpha^2\beta). \tag{B.12}$$

The variables n_L and n_R hold the values of the number densities on the left and right virtual nodes, respectively. These have to be interpolated, for which the following interpolation scheme is used:

$$n_L = (n_p + 1)\frac{n_{p+1} + 1}{n_p + 1}^{\frac{h_p - h_v}{2h_p}} - 1 \tag{B.13}$$

$$n_R = (n_p + 1)\frac{n_{p+1} + 1}{n_p + 1}^{\frac{h_p + h_v}{2h_p}} - 1 \tag{B.14}$$

The integral expression for I is evaluated from 0 to 1, which implies that the upwind is done from the left cell to the right, which is only valid if $|U_L| > |U_R|$. In case of $|U_L| < |U_R|$, the interpolation is done in the opposite direction, and the relation of Γ_{face} becomes:

$$\Gamma_{face} = \frac{D_{face}}{h_p I}(\frac{1}{e^{\alpha}(1 + \alpha\beta)}n_L - n_R). \tag{B.15}$$

I then becomes:

$$I = \frac{\alpha^2 - 2\alpha\beta}{\alpha^3} - \frac{e^\alpha}{\alpha^3}(\alpha^3\beta + \alpha^2 + 2\alpha\beta + 2\alpha^2\beta). \tag{B.16}$$

If h_v is found to be $h_v \geq h_p$, the utilization of the virtual points is obsolete and the original Scharfetter-Gummel method can be used as given in Equation B.6.

MUSCL discretization scheme

A Monotonic Upstream-centered Scheme for Conservation Laws (MUSCL) discretization was formulated by Van Leer (1976) as an alternative to the available methods to describe discontinuities in physical problems. One of such methods was the polynomial approximation, which is famous for the Gibbs phenomenon: spurious numerical oscillations in proximity of the discontinuity whose amplitude diverge when an actual jump in the solution value is approached. The monotonic MUSCL scheme was intended to prevent such oscillations by considering not just the flux of the respective face, but also the fluxes on the surrounding faces. The numerical procedure is explained here.

First the cell stencil is considered, which has been visualized in Figure B.1.

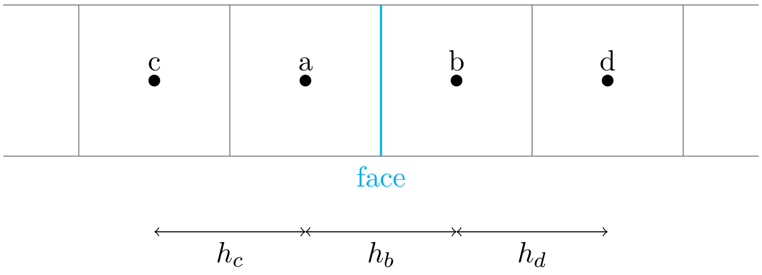

Figure B.1: MUSCL scheme cell layout.

The method relies on correction of the density values in cells a and b, between which the flux is calculated, and cells c and d, whose fluxes influence the values in a and b. By taking this into account, monotonicity can be assured.

Again, the original flux term consists of a drift and a diffusion part:

$$\vec{\Gamma}_k = \vec{U}_k n_k - D_k \nabla n_k. \tag{B.17}$$

$U_k = \pm\mu_k\vec{E}$ is the drift velocity. First, a drift velocity term a is defined which determines from which cell the value of n is interpolated, according to the direction of U. If U is positive, the density is interpolated from cell a to cell b using a^+. If U is negative, the interpolation is done vice versa with a^-.

$$a^+ = \begin{cases} U \text{ if } U > 0, \\ 0 \text{ otherwise.} \end{cases}$$
$$a^- = \begin{cases} U \text{ if } U < 0, \\ 0 \text{ otherwise.} \end{cases}$$

The limiter coefficient r is based on the density gradients of the surrounding cells:

$$r_\mathrm{R} = \begin{cases} \frac{n_b - n_a}{n_a - n_c} \text{ if } n_a - n_c > 0, \\ 0 \text{ otherwise.} \end{cases}$$
$$r_\mathrm{L} = \begin{cases} \frac{n_b - n_a}{n_d - n_b} \text{ if } n_d - n_b > 0, \\ 0 \text{ otherwise.} \end{cases}$$

Now the actual limiter ϕ is determined according to the coefficients r_L and r_R. A *MinMod* limiter function is used, but other functions can be implemented to control the solution in different ways. The *MinMod* limiter function states that:

$$\phi_\mathrm{R} = \begin{cases} \min(\frac{1}{h_c}, \frac{r_\mathrm{R}}{h_d}) \text{ if } r_\mathrm{R} > 0, \\ 0 \text{ otherwise.} \end{cases}$$
$$\phi_\mathrm{L} = \begin{cases} \min(\frac{1}{h_b}, \frac{r_\mathrm{L}}{h_c}) \text{ if } r_\mathrm{L} > 0, \\ 0 \text{ otherwise.} \end{cases}$$

Now the density values in cells a and b are corrected according to the fluxes to their other neighbour cells, i.e. a to c and b to d.

$$n_\mathrm{R} = n_b + \frac{1}{2}\frac{h_d + h_c}{2}\phi_\mathrm{R}(n_d - n_b).$$
$$n_\mathrm{L} = n_a + \frac{1}{2}\frac{h_c + h_b}{2}\phi_\mathrm{L}(n_a - n_c),$$

Now the flux on the face can be calculated from the corrected values n_L and n_R in its original form as presented in Equation B.17:

$$\Gamma_\mathrm{face} = a^+ n_\mathrm{L} + a^- n_\mathrm{R} - D_\mathrm{face} \frac{n_b - n_a}{\frac{h_a + h_b}{2}}. \tag{B.18}$$

Different limiter functions have been presented since the first formulation of this scheme, and the limiter function determines the diffusivity of the solution, as is depicted in Figure B.2.

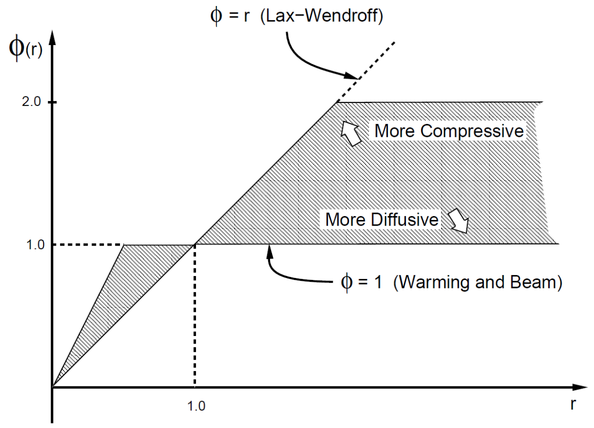

(a) Second-order limiter regions defined by Sweby

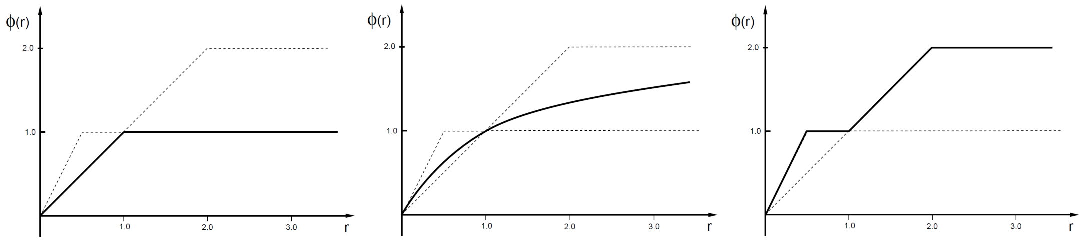

(b) MinMod flux-limiter (c) Van Leer flux-limiter (d) Superbee flux-limiter

Figure B.2: Limiter functions for the second order TVD scheme

Appendix C

Reaction models proposed in literature

C.1 Models for air

The following lookup tables were reported by Hoskinson (2009):

Recombination coefficients

$$\beta_{ei} = 2 \times 10^{-13} \tag{C.1}$$
$$\beta_{ii} = 1.7 \times 10^{-13} \tag{C.2}$$

Ionization coefficients

$$\frac{\alpha}{p}(N2) = \begin{cases} 4.71 \times 10^{-11} \left|E/p\right|^3, & \text{if } \left|E/p\right| < 1.4 \times 10^4 \\ 3.32\sqrt{\left|E/p\right| - 12500}, & \text{if } \left|E/p\right| > 1.4 \times 10^4 \end{cases} \tag{C.3}$$

$$\frac{\alpha}{p}(O2) = \begin{cases} 1.17 \times 10^{-10} \left|E/p\right|^3, & \text{if } \left|E/p\right| < 1.1 \times 10^4 \\ 0.0319\left|E/p\right| - 211, & \text{if } 1.1 \times 10^4 < \left|E/p\right| < 2.1 \times 10^4 \\ 6.32\sqrt{\left|E/p\right| - 16300}, & \text{if } \left|E/p\right| > 2.1 \times 10^4 \end{cases} \tag{C.4}$$

Attachment coefficients

$$\eta \approx p_{O2}\Big[1.307 + \frac{33200}{\left|E/p\right|} \exp\Big(\frac{-(\ln\left|E/p\right| - 9.04)^2}{2.53}\Big)\Big] \tag{C.5}$$

Electron mobility coefficients

$$\mu_e p(N2) = 24.32\exp(\frac{-E/p}{1057}) + 19.38\exp(\frac{-E/p}{23430}) + 14.45 \tag{C.6}$$

$$\mu_e p(O2) = 173.1\exp(\frac{-E/p}{195.1}) + 36.19\exp(\frac{-E/p}{3134.4}) + 31.73\exp(\frac{-E/p}{18205}) + 12.49 \tag{C.7}$$

Positive ion mobility coefficients

$$\mu_p p(N2) = 0.05492\exp(\frac{-E/p}{6858} + 0.07509\exp(\frac{-E/p}{38175} + 0.0308 \tag{C.8}$$

$$\mu_p p(O2) = 0.06841\exp(\frac{-E/p}{59678} + 0.09194\exp(\frac{-E/p}{12763} + 0.0320 \tag{C.9}$$

Negative ion mobility coefficient

$$\mu_p p(N2) = 0 \tag{C.10}$$

$$\mu_p p(O2) = 0.181125 \tag{C.11}$$

Plasma effective coefficients

$$\mu_{eff} = \frac{1}{p}\left[p_{N2}\cdot\mu_{N2} + p_{O2}\cdot\mu_{O2}\right] \tag{C.12}$$

$$\alpha_{eff} = p_{N2}\cdot\frac{\alpha}{p}(N2) + p_{O2}\cdot\frac{\alpha}{p}(O2) \tag{C.13}$$

Diffusion coefficients (k=e,n,p)

$$D_k = k_B T_k/m_k v_m = \mu_k k_B T_k \tag{C.14}$$

C.2 Models for helium

For helium, several models are available Golubovskii et al. (2002a); Mangolini et al. (2004); Jayaraman et al. (2007). These models differ most importantly in the number of species taken into account, and their respective chemical reactions. In this work, only electrons and atomic helium are considered. The coefficients are given by the following relations. Note that the units of the pressure normalized electric field $|E/p|$ is in [V cm-1 Torr-1]in these tables.

$$\alpha_{He}/p_g = 4.4\exp(-14.0/\sqrt{|E/p|}) \tag{C.15}$$

$$\alpha_{N_2}/p_g = 8.8\exp(-275.0/|E/p|) \tag{C.16}$$

$$\mu_p p_g = \begin{cases} 8.0\times 10^3(1-8.0\times 10^{-3}|E/p|) \text{ if} & |E/p| \leq 25\text{V cm-1 Torr-1}, \\ 4.1\times 10^3/\sqrt{|E/p|}(1-27.44/\sqrt{|E/p|^3}) \text{ if} & |E/p| > 25\text{V cm-1 Torr-1} \end{cases} \tag{C.17}$$

The following differences can be distinguished:

Reference	α [cm-1]	β_{ep} [cm3 s-1]
Golubovskii et al. (2002a)	$99.5\%\alpha_{He} + 0.5\%\alpha_{N_2}$	$8.9 \times 10^{-9}(T_e/T_p)^{-3/2}$
Mangolini et al. (2004)	$99.5\%\alpha_{He} + 0.5\%\alpha_{N_2}$	$8.0 \times 10^{-20}(T_p/T_e)^4 n_e$
Jayaraman et al. (2007)	α_{He}	$1.09 \times 10^{-20}(T_p)^{9/2} n_e$

Table C.1: Reaction rate coefficients for helium from different references, where $v_{en} = 10^{12}[s{-}1]$. All units in this table are given in units of cm. The variables given in this table refer to the curve fittings in Equation C.15 to Equation C.17.

Reference	μ_e [cm2 V-1 s-1]	μ_p	D_e [cm2 s-1]	D_p
Golubovskii et al. (2002a)	$0.86/p \times 10^6$	μ_p	0	0
Mangolini et al. (2004)	$0.86/p \times 10^6$	10	$\mu_e T_e$	$420/p$
Jayaraman et al. (2007)	$e/(m_e v_{en})$	10	$\mu_e T_e$	$500/p$

Table C.2: Mobility coefficients for helium from different references, where $v_{en} = 10^{12}[s - 1]$. All units in this table are given in units of cm. The variables given in this table refer to the curve fittings in Equation C.15 to Equation C.17.

- The models of Golubovskii and Mangolini both take Penning ionization into consideration due to nitrogen impurities, whereas the model of Jayaraman & Shyy does not. The latter model is expected to have an increased breakdown voltage, and a delayed moment of breakdown;

- The model of Golubovskii has a recombination coefficient linearly dependent on n_e and n_p, which is a quadratic dependency on n_e for the other two models;

- The model by Jayaraman & Shyy has a higher electron mobility (0.178 versus 0.113 for the first two models). Higher electron mobility results in higher electron velocities and higher ionization frequencies. This is expected to yield stronger breakdown phenomenon, such as higher production of species and higher current amplitudes;

- Finally, the model of Golubovskii assumes an ion mobility variable with the electric field $|E/p|$ through an inverse dependency, i.e. μ_p decreases as $|E/p|$ increases.